Improved Seismic Design Recommendations for Wide-Flange Columns in Ductile Steel Moment-Resisting Frames considering Three-dimensional Response

by

Abrar Islam

A thesis submitted in partial fulfillment of the requirements for the degree of

Master of Science

in Structural Engineering

Department of Civil and Environmental Engineering
University of Alberta

Abstract

Deep wide-flange columns are commonly used in the construction of steel moment-resisting frames (MRFs) to resist lateral seismic loads in high seismic regions in North America. Past studies on deep columns with base plastic hinges located at the first storey of MRFs have indicated that such sections can be prone to significant axial shortening and out-of-plane instability under design-level seismic excitation. Despite significant advancement in the seismic performance of steel wide-flange columns, the effect of limit states observed in the past studies on the member seismic stability response has not been quantified in the framework of the Canadian design practice. Moreover, the influence of three-dimensional response of steel MRFs on the stability of the first-storey columns with base plastic hinging using more representative loading protocols expected under seismic loads, e.g., earthquake accelerations, has not been well comprehended yet. Finally, new supporting data is needed 1) to evaluate the current stability design requirements; and 2) to propose enhanced seismic stability recommendations to improve the design of steel MRFs in Canada. Therefore, this study aims to evaluate the stability response of wide-flange columns of Ductile steel MRFs under seismic loading and propose enhanced stability design recommendations in the framework of the Canadian steel design standard (CSA S16).

A prototype five-storey Ductile MRF was selected and designed following the CSA S16 seismic design provisions. Various column design scenarios were considered. The concentrated plasticity-based numerical model of the MRF was then developed, which was used to perform nonlinear response history analyses under the ground motion records representing three predominant seismic actions in western Canada. The global and local responses of the alternative designs were evaluated using nonlinear response history analysis (NLRHA) results. A continuum-based finite element

model of the interior and exterior columns isolated from the prototype MRF designs was developed and subjected to the displacements and axial load histories obtained from the NLRHA. The results of the NLRHA of the frame and those from the CFEM of the isolated columns were used to evaluate the CSA S16 stability design requirements.

A continuum-based finite element model (CFEM) of an MRF subassembly consisting of the exterior bay plus half of the adjacent interior bay was also created to study the three-dimensional response of steel MRFs. A weak-axis bending moment loading protocol was created using the results of the NLRHA of the MRF subassembly, which in combination with in-plane cyclic displacement history and a constant gravity-induced axial compression load were used to perform a parameter study on column stability response using a refined CFEM representing isolated interior first-storey MRF columns. A total of 52 columns were analyzed by varying the section size, unbraced length, and axial load ratios.

The results of this study showed that the equivalent moment factor $\kappa = 0.45$ can be used for first-storey columns, which results in a lateral bracing limit of $L_b/r_y = 70$. The CFEM of the MRF subassembly is a good tool to understand the three-dimensional demands of first-storey columns under seismic loading. Moreover, four strength and deformation response parameters, including base moment, axial shortening, out-of-plane displacement, and cross-section twist angle, can be used to determine column instability modes, including out-of-plane buckling at the base and member buckling. Column stability was detrimentally affected by the level of the constant gravity-induced axial load. Finally, a simple, coupled empirical equation as a function of the global slenderness ratio (L_b/r_y), cross-section aspect ratio (d/b_f), and axial load ratio (C_f/AF_y) was proposed to predict the stability response of wide-flange columns with base plastic hinging in the framework of the Canadian steel design standard.

Acknowledgements

This research project was funded by the Natural Sciences and Engineering Research Council (NSERC) and Canadian Institute of Steel Construction (CISC). Financial support in the form of scholarships was provided by the Faculty of Graduate Studies and Research at the University of Alberta.

Thank you to my fellow Steel Centre colleagues and coworkers for the valuable discussions, meetings, and support throughout my research project.

Table of Contents

List of Tables

List of Figures

List of Symbols

A : Gross cross-section area

A_f : Cross-section flange area

A_w : Cross-section web area

b_f : Width of flange

C_f : Total factored axial compression load

C_{fg} : Factored axial compression load from gravity

$C_{P\Delta}$: Factored axial compression load on P-Delta leaning columns

C_y : Yield capacity under compression

C_r : Resistance under compression

C_w : Warping torsional constant

d : Section depth

d_b : Beam section depth

d_c : Column section depth

E : Modulus of elasticity

F_y : Specified nominal yield stress

G : Shear modulus

h : Web clear depth

I_x : Moment of inertia about the strong axis

I_y : Moment of inertia about the weak axis

J : St. Venant torsional constant

κ : Ratio of smaller moment to larger moment demand from opposite ends of the member unbraced length

L : Length of member

L_b : Unbraced length of member

$M_{c,prob}$: Expected yield moment about strong axis from Modified Ibarra-Medina Krawinkler backbone curve

M_{pb} : Nominal plastic moment capacity of beam about strong axis

M_{pc} : Nominal plastic moment capacity of column about strong axis

M_x, M_{fx}: Moment demand about strong axis

M_y, M_{fy}: Moment demand about weak axis

M_{px} : Nominal plastic moment capacity about strong axis

M_{py} : Nominal plastic moment capacity about weak axis

M_{small} : Smaller moment demand at member end

M_{large} : Larger moment demand at member end

M_{rx} : Moment resistance about strong axis

M_w : Moment magnitude of ground motion

R : Hypocentral distance of ground motion

R_d : Ductility reduction factor

R_o : Over-strength reduction factor

R_{sh} : Strain hardening factor

r_x : Radius of gyration about strong axis

R_yF_y : Specified expected yield stress

r_y : Radius of gyration about weak axis

$S_a(g)$: Pseudo spectral acceleration

t_f : Section flange thickness

t_w : Section web thickness

W : Seismic weight

Z_x : Plastic section modulus about the strong axis

Z_{RBS} : Plastic section modulus about the strong axis for reduced beam section (RBS)

Z_y : Plastic section modulus about the weak axis

Δ : Lateral displacement of storey

Δ_{axial} : Axial displacement along member cross-section

$\Delta_{out-of-plane}$: Out-of-plane displacement of member cross-section

$\gamma_{cross-section}$: Twist of member cross-section in radians

θ : Chord rotation of member account for drift with axial shortening of member

θ_{PH} : Rotation demand at Modified Ibarra-Medina Krawinkler non-linear plastic hinge spring

θ_y : Yield rotation from Modified Ibarra-Medina Krawinkler backbone curve

List of Abbreviations

2D : Two dimensional

3D : Three dimensional

AISC : American Institute of Steel Construction

BRBF : Buckling-restrained braced Frame

CFEM : Continuum-based finite element model

CISC : Canadian Institute of Steel Construction

CSA : Canadian Standards Association

DOF : Degree-of-freedom

IMK : Ibarra-Medina-Krawinkler

kN : Kilonewton

LTB : Lateral-torsional buckling

MPa : Megapascal

MRF : Moment-resisting frame

NBCC : National Building Code of Canada

NLRHA : Nonlinear response history analysis

OpenSees : Open System for Earthquake Engineering Simulation

RBS : Reduced beam section

RP : Reference point in ABAQUS

SAP2000 : Structural Analysis Program 2000

SMRF : Special Moment-Resisting Frame

Chapter 1. Introduction

1.1 Background

Steel moment-resisting frames (MRFs) are widely used as the seismic force-resisting system of building structures, particularly in high seismic regions. Fig.1-1a shows an example of a five-storey steel MRF with the beam-to-column moment connection and the column base detail typical of North American construction practice. Ductile MRFs are designed to dissipate seismic input energy through flexural yielding at beam ends and column bases, as shown in Fig. 1-1b, plus limited shear yielding in the beam-to-column panel zone. MRF members are designed to resist gravity plus seismic load effects and satisfy code-specified storey drift limits, which often dictates the selection of beams and columns. Columns of steel MRFs are commonly made of wide-flange members and are designed to resist the combined effect of gravity and seismic loads.

According to the modern design standards such as the Canadian steel design standard CSA S16 (CSA 2019), columns, except those located in the first storey with base plastic hinging and those part of a continuous column stack located at the roof level (the latter is not the intent of this study), should be designed to remain essentially elastic to ensure the achievement of desirable yielding hierarchy and maintain the gravity load-carrying capacity under seismic loading. The first-storey columns with anticipated base plastic hinging are expected to possess sufficient strength and remain stable under code-specified seismic plus gravity loads, and when the beams reach their probable flexural resistance. Additionally, their flexural stiffness along with other MRF columns and the beams should be sufficient to limit the lateral displacement of each storey to the displacement corresponding to the drift limit prescribed by the respective building code, e.g., 2.5% as per the National Building Code of Canada (NBCC 2015). Similar provisions can be found in other design standards such as U.S. Seismic Provisions for Steel Buildings AISC

341 (AISC 2016), Eurocode 8 (EN1998-1 2003), and New Zealand steel design standard NZS 3404 (NZS 1997).

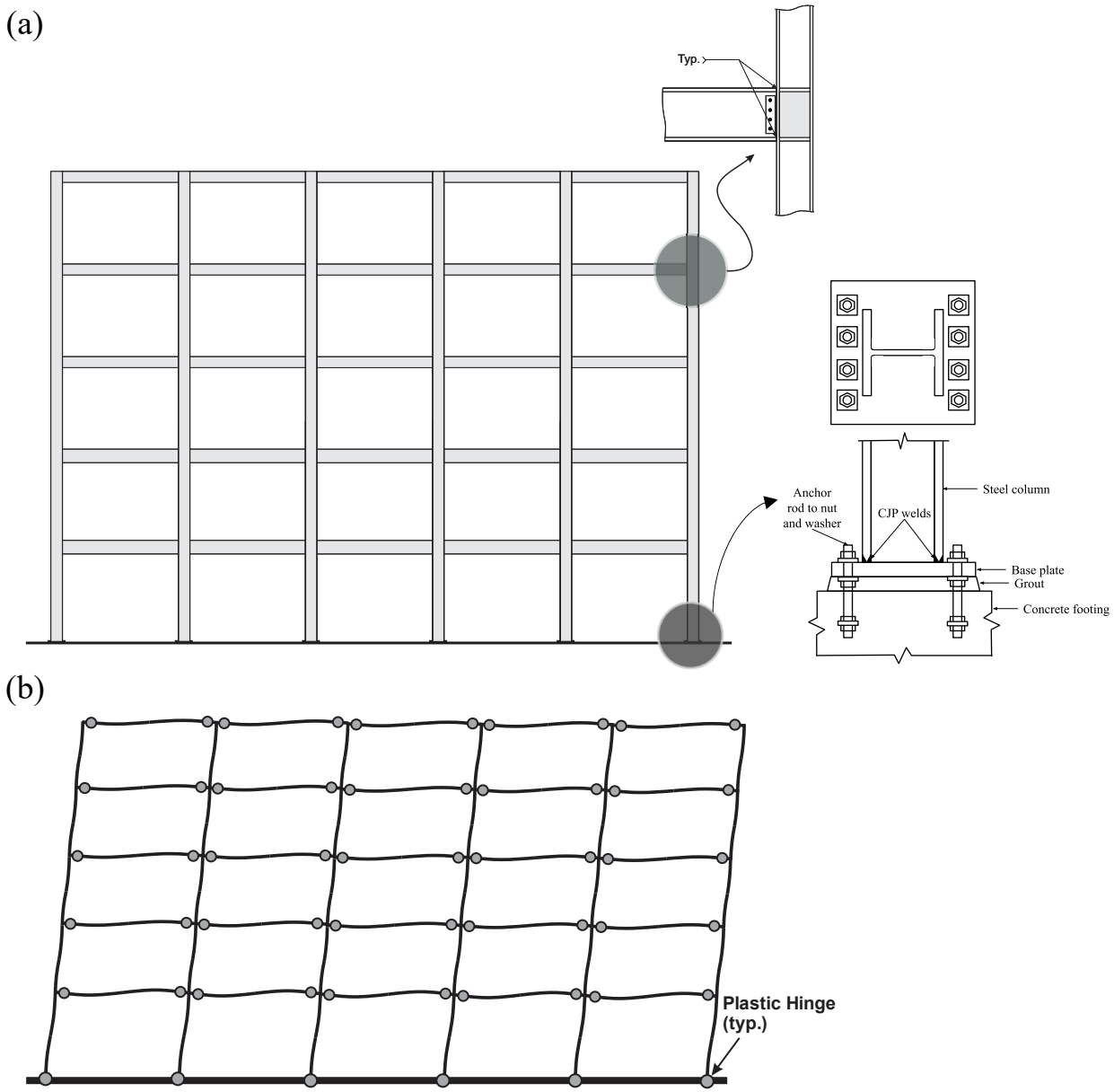

Figure 1-1. (a) Steel moment-resisting frame (MRF); (b) Desired plastic collapse mechanism of steel MRFs

Extensive research studies have been performed in the past to evaluate the inelastic cyclic response of steel MRF columns and beam-to-column moment connections (Popov et al. 1975; MacRae 1990; Nakashima et al. 1990; Popov et al. 1998; FEMA 355D; Yu et al. 2000; Shen et al. 2002; Ricles et

al. 2004), which led to the development and improvement of the seismic design provisions for steel MRFs. In particular, Newell and Uang (2008) examined the cyclic inelastic response of wide-flange columns isolated from steel buckling-restrained braced (BRB) frames with low width-to-thickness ratio, i.e., Class 1 flange and web, and nearly square shape ($d/b_f \approx 1.0$) where d is the overall depth of the cross-section and b_f is the flange width) under varying axial loads and large lateral displacements. It was confirmed that square columns under high axial compression load exhibit a stable response and significant rotational capacity with minor flexural strength degradation and twisting. Over the past decade, the focus has shifted to the cyclic behaviour of steel wide-flange columns with deep cross-sections ($d/b_f \geq 1.7$). The cyclic stability of deep wide-flange columns was evaluated using large-scale laboratory testing (Ozkula et al. 2017a, 2021; Uang et al. 2019; Elkady and Lignos 2017a, 2018a, Cravero et al. 2020) and detailed finite element simulations (Elkady and Lignos 2018b, Ozkula 2017b). The specimens representing the first-storey column of a multi-storey steel MRF were tested under unidirectional and bidirectional loading protocols with various end conditions. The results showed that the flexural capacity of wide-flange columns, particularly at large storey drifts, is often controlled by local buckling at the end plastic hinge locations. Member stability, including weak-axis flexural buckling or lateral-torsional buckling, was observed after local buckling in columns with high member slenderness ratios, e.g., $L_b/r_y = 161$ where L_b is the unbraced length and r_y is the radius of gyration about the section weak-axis. Moreover, it was confirmed that column instability highly depends on its end conditions and is less severe when a fixed-flexible end condition is employed. The numerical simulation of wide-flange columns focused on generating a larger database of column cyclic responses to develop design recommendations and nonlinear modelling parameters.

To safely achieve the MRF plastic mechanism (Fig. 1-1b), particularly the anticipated flexural plastic hinging at the base of columns, the Canadian steel design standard specifies a set of seismic design requirements for columns in Ductile (Type D) and Moderately Ductile (Type MD) steel MRFs. These provisions consist of the column strength verification using the strong column-weak beam concept at every joint, column stability checks, including in-plane and lateral-torsional buckling modes, for all the columns except the first–storey column, and special provisions for the first-storey columns with base plastic hinging. In lieu of the stability verification for the first-storey columns with base plastic hinging, the Canadian steel design standard sets out special requirements by imposing uncoupled limits on section width-to-thickness ratios, global slenderness ratio, and axial load ratio to ensure stable and ductile response under major seismic events. However, these requirements lack sufficient background research and may, in some cases, lead to highly conservative designs.

1.2 Problem Statement

Deep wide-flange columns are preferred in the construction of MRFs because they provide greater stiffness and moment capacity in the plane of the MRF compared to square-shaped wide-flange sections at the same weight. This helps minimize the structural weight while efficiently meeting the stringent code-specified storey drift limit, which often governs the selection of members in steel MRFs due to their high inherent flexibility under lateral loads.

Recent studies on deep wide-flange columns under cyclic loading have shown that they can be prone to significant strength and stiffness degradation once a plastic hinge is formed at their base or both ends under large storey drifts, mainly due to the severe flange and web local buckling near the plastic hinge location (Ozkula et al. 2017a; Elkady and Lingos 2018a). Furthermore, the columns with large global slenderness ratios ($L_b/r_y \geq 80$) may be prone to out-of-plane instability

at large storey drifts (Elkady and Lignos 2018b). Despite significant advancement of the body of knowledge on seismic performance of steel wide-flange columns, the effect of limit states observed in the past studies on the member seismic stability response has not yet been quantified, in particular, in the framework of the Canadian design practice. Moreover, the influence of three-dimensional response of steel MRFs, e.g., the weak-axis moment and displacement caused by beam out-of-plane response and local buckling near the column plastic hinge, on the stability of the first-storey columns with base plastic hinging has not been well comprehended yet. Finally, new studies are needed to quantify column seismic-induced demands under more representative loading protocols expected under seismic loads, e.g., earthquake accelerations.

The special stability design requirements, i.e., uncoupled stability design limits, prescribed by CSA S16-19 for Ductile and Moderately Ductile steel MRF columns that develop plastic hinges may not appropriately represent their behavior under seismic loads, in particular, when deep wide-flange columns are used. Thus, new supporting data is needed 1) to evaluate the current stability design requirements; and 2) to propose enhanced seismic stability recommendations to improve the design of steel MRFs in Canada.

1.3 Research Objectives

The general objective of this M.Sc. thesis is to evaluate the stability response of wide-flange columns of Ductile steel MRFs under seismic loading and propose enhanced stability design recommendations in the framework of the Canadian steel design standard. The specific objectives of this research are as follows:

- To determine the seismic-induced demands for steel MRFs under design-level earthquake ground motion accelerations.

- To examine the three-dimensional response of wide-flange steel columns under the demands expected when the MRF is subjected to earthquake base excitation.
- To develop a continuum-based finite element model of an MRF subassembly, including beams, columns, and beam-to-column connections.
- To quantify the three-dimensional force and deformation demands, i.e., in-plane strong-axis bending, twist, out-of-plane deformation, and weak-axis bending, of wide-flange columns using the subassembly model under seismic ground motions.
- To assess the 2019 CSA S16 stability design requirements for wide-flange steel columns located in the first storey of Ductile MRFs, namely the global slenderness ratio limit, axial load ratio limit, and width-to-thickness ratio limits
- To propose and validate enhanced seismic design recommendations, e.g., coupled stability design limits, more liberal limits, requirements representative of the anticipated seismic response, for steel MRF columns with base plastic hinging.

1.4 Research Methodology

The following eight steps were completed to achieve the objectives of this research project:

1) Literature Review: a survey of past experimental and numerical investigation on the seismic performance of steel MRFs and wide-flange steel columns. A review of past numerical modelling techniques was also conducted to develop low- and high-fidelity models for steel MRFs.
2) MRF Design: Several prototype Ductile (Type D) steel MRFs were designed in accordance with the requirements of CSA S16-19. The frames were part of a five-storey office building located in Vancouver, British Columbia, representing a high seismic region on the west coast of Canada.

3) Earthquake ground motions: a suite of 33 historical ground motions were selected and scaled following the recommendation of the 2015 National Building Code (NBCC) of Canada.
4) Frame Numerical Model and Nonlinear Response History Analysis: a concentrated plasticity-based numerical model of prototype MRFs designed in Step 2 was developed and used to perform nonlinear response history analyses (NLRHA) under the records selected and scaled in Step 3. Seismic-induced demands were then extracted from the analysis results.
5) Column Numerical Model and Analysis: a continuum-based finite element model (CFEM) of the wide-flange column isolated from the first storey of MRF was developed. The model was used to perform static analyses under the axial load and in-plane displacement history obtained from the NLRHA in Step 4. The analyses were used to understand the columns' seismic stability response and evaluate the CSA S16 (uncoupled) stability design provisions.
6) MRF Subassembly Numerical Model and Analysis: A continuum-based finite element model of one of the prototype MRFs designed in Step 2 was developed. The model includes the exterior bay plus half of the adjacent interior bay of the frame. The MRF subassembly was analyzed under three ground motion accelerations producing the largest displacement demands on the structure. The analyses results were leveraged to understand the three-dimensional response of the MRF with the focus on the first-storey column, including the strong-axis and weak-axis moments, out-of-plane deformations, and twists. Moreover, the MRF subassembly was used to refine the CFEM of the isolated column of Step 5 by including the weak-axis moments.

7) Column Stability Parameter Study: a total of 52 wide-flange steel columns encompassing a wide range of global and local slenderness ratios as well as two axial load ratios that represent potential MRF columns in the Canadian design practice was selected and analyzed under a combination of axial compression load, weak-axis bending moment, and in-plane displacement demand using the refined CFEM of Step 5. The results were then used to further examine the Canadian seismic design provisions for steel MRF columns and improve design recommendations.
8) Design Recommendation Development: An improved, coupled, yet simple interaction equation consisting of section and member geometric properties, global slenderness ratio, and cross-section aspect ratio), and axial load ratio, which were found in Step 7 to influence the column seismic performance, was developed in the context of the Canadian steel design standard using the results of the parameter study.

1.5 Organization of Report

This M.Sc. thesis is organized into five chapters. Chapter 1 presents the background information, the research objectives, and the methodology used to carry out the research. Chapter 2 provides an overview of the 2019 Canadian seismic provisions for wide-flange columns and a review of the past research on the response of wide-flange columns under seismic loading. In Chapter 3, the stability design requirements of CSA S16 are evaluated using the concentrated plasticity-based model of the frame and the CFEM of the isolated column, and design recommendations, including new the equivalent moment factor, global slenderness limit, are proposed for both interior and exterior columns. With some minor modifications, this chapter has been accepted for publication in the *Bulletin of Earthquake Engineering*, with the title “Stability of Wide-Flange Columns in Steel Moment-Resisting Frames: Evaluation of the Canadian Seismic Design Requirements”.

Chapter 4 presents the development and dynamic analysis of the CFEM of the MRF subassembly used to study the three-dimensional response of the MRF with emphasis on the first-storey column demands, a parameter study on the column stability response used the refined CFEM of the isolated column, and the development of new stability design recommendations in the context of the Canadian steel design standard that couple the section aspect ratio, member slenderness ratio, and axial force level. With some minor modifications, this chapter will be submitted to the *Journal of Constructional Steel Research* with the title, "Seismic Performance of Wide-Flange Columns in Ductile Moment-Resisting Frames: Three-Dimensional Response and Stability Design Recommendations". Finally, a summary of the thesis, the key findings, limitations, and recommendations for future work are presented in Chapter 5. The author also contributed, based on his M.Sc. project, to a collaborative work submitted to the *Journal of Constructional Steel Research* with the title, "Development, Seismic Performance and Collapse Evaluation of an Innovative Steel Moment-Resisting Knee Braced Frame Considering the Seismic Sources Expected in the West Coast of North America".

Chapter 2. Literature Review

2.1 Introduction

The chapter summarizes the key design requirements for wide-flange columns in steel Type D MRFs. An overview of past experimental and numerical research studies on wide-flange steel columns under seismic loading is provided.

2.2 Canadian Seismic Design Provisions

As per the Canadian seismic design provisions for Ductile steel MRFs, beams shall meet the most stringent width-to-thickness limits specified for Class 1 (i.e., highly ductile sections) that are 7.3 and 58.8 for the flange and web, respectively. The columns are selected from Class 1 or Class 2 sections, and their strength is verified when beams reach their probable flexural resistance (i.e., plastic hinging forms at the beam ends) by ensuring the combined flexural capacity of the column sections above and below the joint exceeds the summation of the flexural demands imposed by adjoining beams:

$$\sum 1.18\Phi M_{pc}\left(1-\frac{C_f}{\Phi C_y}\right) \geq \sum(R_{sh}R_y M_{pb}+V_h s_h) \tag{2-1}$$

where $\Phi = 0.9$ is the resistance factor, M_{pc} and M_{pb} are nominal plastic moment resistances of the columns and beams, respectively, and $C_y = AF_y$ is the axial compressive load at yield strength. A is the cross-sectional area and F_y is the specified nominal yield strength of the material. The term $R_{sh}R_yM_{pb}$ in Eq. 2-1 represents the probable flexural resistance of the adjacent beams, including the effects of strain hardening $R_{sh} = 1.1$ and ratio of the probable-to-nominal yield stresses R_y. The total flexural demand on the columns also includes the moments induced by beam shear forces V_h located at the anticipated beam plastic hinge, a distance s_h away from the column centreline. The column axial force C_f is calculated considering gravity loads plus the summation of beam shears

when they reach their probable flexural resistance, acting at and above the storey under consideration.

The columns that are expected to remain elastic under seismic loads (e.g., columns other than those in Storey 1 and the roof level of the continuous columns) should be verified for in-plane and out-of-plane stability using the axial force – bending interaction equation as follows:

$$\frac{C_f}{C_r}+\frac{0.85U_{1x}M_{fx}}{M_{rx}} \leq 1.0 \qquad \text{where } U_{1x}=\frac{\omega_1}{1-C_f/C_{ex}} \tag{2-2}$$

where M_{fx} is the factored strong-axis bending demand when the beams reach their probable flexural resistance. C_r is the factored axial resistance based on strong-axis buckling mode when verifying in-plane buckling limit state. In contrast, weak-axis buckling resistance is used when the lateral-torsional buckling limit state is examined. M_{rx} is the strong-axis factored moment resistance computed considering full yielding of the cross-section when in-plane stability is verified and the lateral-torsional buckling resistance when out-of-plane stability limit state is evaluated. The factor U_{1x} accounts for moment gradient and member level second-order effects. ω_{1x} is the bending coefficient and is the larger of 0.4 and $0.6 - 0.4\kappa$, and C_{ex} is the Euler buckling load of a column. The factor κ (i.e., the moment distribution factor) is the ratio of the smaller to the larger factored column moment demand at opposite ends of the members unbraced length, which is positive when the member is in contraflexure (positive for double curvature and negative for single curvature). For elastic sway frames, U_{1x} is set equal to 1.0 for in-plane and out-of-plane stability limit states (Imanpour et al. 2016).

Although stability limit states need not be verified for the first-storey column, since the same column profile is often used for the first and second stories, member stability in the second-storey columns may control the selection of the column section in the first storey.

CSA S16 specifies special requirements for the first-storey columns with anticipated base plastic hinging to ensure stable and ductile response under major seismic events. These columns shall comply with the width-to-thickness limits of Class 1 sections. In lieu of the out-of-plane stability check using Eq. 2-2, which is designed to verify the stability of elastic members, the following lateral bracing requirement shall be met:

$$\frac{L_b}{r_y} \leq \frac{17250+15500\kappa}{F_y} \tag{2-3}$$

in which L_b/r_y is the global slenderness ratio of the member about its weak-axis, L_b represents the unsupported length (e.g., storey height), and r_y is the radius of gyration about the weak-axis. When verifying Eq. 2-3, $\kappa = 0$ is recommended unless a rational analysis can justify another value. CSA S16 also requires that the factored axial load of the column be limited to $0.30AF_y$ for MRFs located in high seismic regions (Seismic Category 4). This limit is intended to avoid the rapid degradation of the flexural strength of the member under high axial load, which can limit column ductility under seismic loading. For the first-storey columns subjected to a factored axial load greater than or equal to $0.15AF_y$, a more stringent limit for the web width-to-thickness ratio h/t_w compared to that of Class 1 sections must be met:

$$\frac{h}{t_w} \leq \frac{700}{\sqrt{F_y}} \qquad \text{when } C_f \geq 0.15AF_y \tag{2-4}$$

where h and t_w are the web clear depth and thickness. When imposing Eqs. 2-3 and 2-4 to a wide-flange column with F_y = 350 MPa, the global slenderness ratio would be limited to 50, assuming $\kappa = 0$, and the h/t_w limit would be 37, eliminating the majority of deep wide-flange sections in design, which would be otherwise ideal to meet the stringent code storey drift limits. It is important to note that Eqs. 2-2 and 2-4 have been specified for the first time in the 2019 edition of the standard. When flexural yielding is expected at the base of the first-storey column, the verification of member stability using the axial force – bending interaction equation (e.g., Eq. 2-2) is not required, which

may be attributed to the fact that heavy and square wide-flange members were typically used as MRF columns in the past where the potential for lateral instability is unlikely as confirmed by the results of past experimental and numerical studies performed on square members (FEMA 2000a, FEMA 2000b, Newell and Uang 2008). The U.S. seismic provisions for structural steel buildings AISC 341 (2016) currently do not specify any special stability design requirements for Special Moment-Resisting Frames (SMRFs), comparable to Type D MRFs in Canada.

2.3 Cyclic Response on Square Wide-flange Columns

Newell and Uang (2008) tested 9 full-scale square column specimens (W360×196, W360×262, W360×347 and W360×551) that were designed as part of multi-storey buckling-restrained braced frames (BRBF), which have roughly equal cross-section depth and flange width ($d/b_f \approx 1$), under cyclic loading at different levels of constant axial loads at 35, 55, and 75% of the specimen axial yield strength measured in the laboratory. The specimens had a clear length of 4570 mm, and the lateral displacement history was set to the symmetric cyclic loading protocol proposed in Section K of AISC 341-16 with gradually increasing storey drifts from 0 to 10%. Rotational DOFs and translational DOF in the weak-axis were fixed at both ends of each specimen, while the axial load was imposed in the longitudinal direction of the specimen, and the lateral displacement was applied at one end along the plane of the column web. Although the columns were designed as part of multi-storey buckling-restrained braced frames (BRBF), the results still represent the cyclic performance such square wide-flange sections would have as columns in an MRF. The text matrix was comprised of three W360×196 and three W360×262 specimens at all three axial load levels; two W360×347 specimens loaded at 35 and 55% of their axial yield capacity; and finally, one W360×551 specimen loaded at 35% of its axial capacity. Fig. 2-1 shows the deformed shape of the W360×196 column specimen loaded to $0.75AF_y$ at 4% and 10% storey drift and the moment versus drift response.

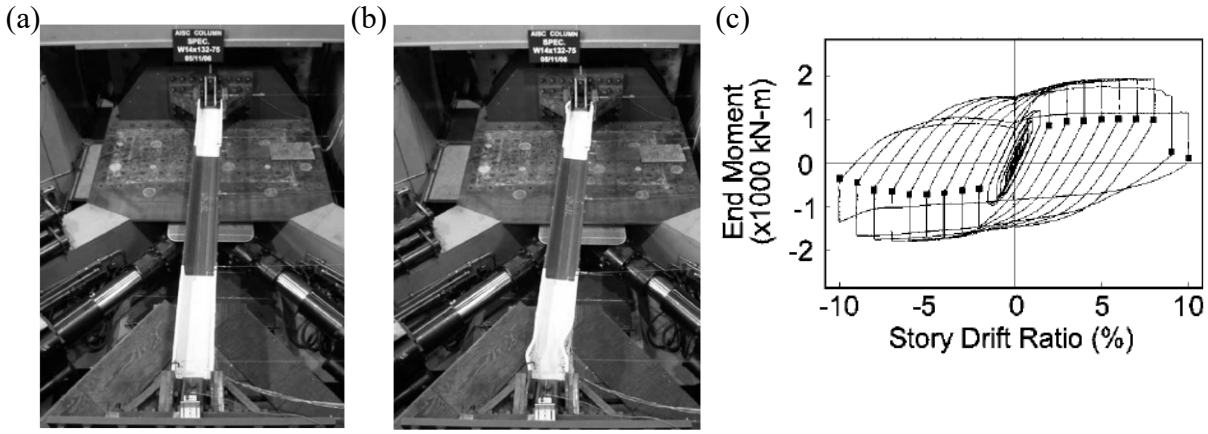

Figure 2-1. W360×196 column specimen loaded to 75% of its axial capacity: (a) 4% storey drift; (b) 10% storey drift; (c) end moment versus storey drift response (Newell and Uang 2008).

As shown in Fig. 2-1, the W360×196 specimen, the most slender specimen in the test matrix, provides a stable response with minimal local buckling at 4% storey drift even under a very large constant axial load of $0.75AF_y$. At 10% storey drift, the specimen exhibits more pronounced flange local buckling at both the top and bottom, but no global buckling is present. The column moment capacities decreased as the axial load was increased in the experiments. This study's column storey drift capacity was defined as when the peak-end moment degraded by 10%. Overall, the W360 specimens exhibited storey drift capacities of 7-9% even at high axial load demands up to $0.75AF_{y,}$ with local flange buckling being the dominant buckling mode. It was concluded that such large deformation capacities were possible for these sections due to the stabilizing effect provided by the stocky column web delaying the flange local buckling. No global buckling was observed in any of the specimens. The specimens also exhibited plastic rotation capacities 14-23 times the actual yield rotation at axial load ratios greater than 0.5. These findings show the remarkable stability of square wide-flange column sections under cyclic loading and can be used as a baseline for comparison for deep wide-flange column sections.

In 2011, Lamarche and Tremblay tested 4 W310×129 ($d/b_f \approx 1$) columns with global slenderness (L_b/r_y) equal to 48 under several monotonic and cyclic axial loading protocols. Axial load was applied eccentrically to one of the specimens and then concentrically to the remaining columns. The columns were tested under quasi-static cyclic and dynamic cyclic loading protocols. An axial load equal to 60% of the column nominal compressive strength was first applied, followed by cyclic axial displacements to simulate seismic demands expected in columns of braced frames. All the specimens exhibited weak-axis buckling and formed a plastic hinge at the mid-height. The column specimens were able to carry the applied gravity loads up to axial deformation of 0.53%L and out-of-plane displacements at column mid-height of 3.7%L. The cyclic tests showed that large strain rates could increase the column buckling and post-buckling compressive strength. Fig. 2-2 provides images of the deformation response of a concentrically loaded W310×129 specimen under cyclic loading.

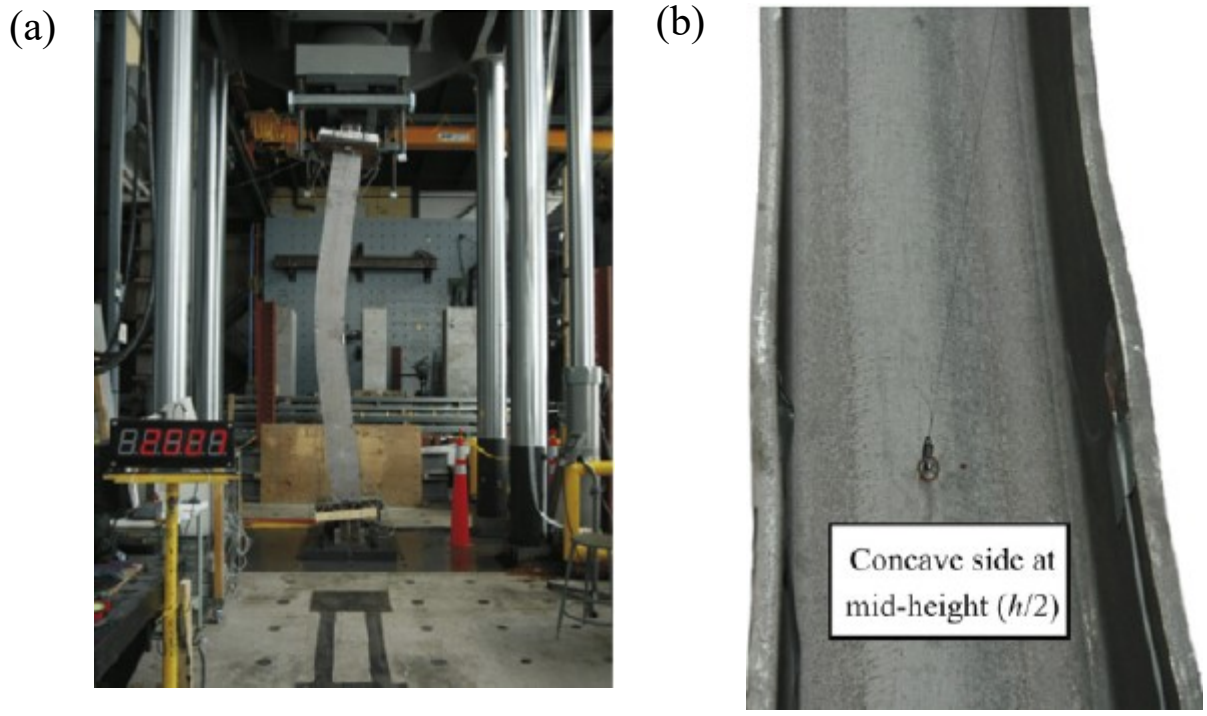

Figure 2-2. W310×129 specimen post-buckling deformed shape: (a) global buckling shape; (c) flange local buckling at mid-height (Lamarche and Tremblay 2011).

2.4 Cyclic Behaviour of Deep Wide-flange Columns

Deep wide-flange sections ($d/b_f \geq 1.7$) have become more popular in constructing steel MRFs. This is due to the larger in-plane stiffness and strength provided by deep sections at the same weight, allowing designers to meet the stringent storey drift limits at reduced structural steel weights since lighter beam and column sections can be used.

Recently, the hysteretic behaviour of deep wide-flange columns representing typical members in the first storey of MRFs was investigated by Elkady and Lignos (2018a) in a comprehensive full-scale testing program. The tests were completed with a 6 degrees-of-freedom (DOFs) system capable of applying translations and rotations at the top end of the specimen in force- or displacement-controlled mode or the combination of both. The test matrix included 10 column specimens, including six W610×217 and four W610×125 sections of 3900 mm in clear height, and was subjected to both unidirectional and bidirectional loading using fixed-fixed and fixed-flexible end boundary conditions. The fixed-flexible cases represent the real boundary conditions at the first storey of a typical MRF. The bidirectional loading sequence was created by placing a predefined displacement history at the column top in the direction perpendicular to the column web. All the specimens were fixed at the ends about their weak axis bending direction, and torsion was restrained. Two lateral displacement protocols along the plane of the web were employed for the tests, the AISC symmetric cyclic loading protocol and a collapse consistent loading protocol created to represent earthquakes' ratcheting behaviour using a few inelastic load cycles followed by large monotonic pushes in one direction. The column specimens were placed under constant axial loads of $0.20AF_y$ and $0.50AF_y$ to represent interior first-storey columns in MRFs, which are more critical than end columns that are subject to largely fluctuating axial loads due to dynamic

overturning effects. Fig. 2-3 shows a photo of the W610×217 test specimen subjected to the AISC symmetric loading protocol under a constant axial load of $0.20AF_y$ along with its base moment versus chord rotation response. Chord rotation represents the drift of the member computed while considering the reduced length due to axial shortening. The column is under fixed-fixed boundary conditions similar to the tests carried out on W360 sections. Comparing the response of the W360×196 section in Fig. 2-1 to the W610×217 section in Fig. 2-3 highlights the more stable response provided by square columns compared to their deep counterparts. Even with a three times higher normalized axial load, the W360×196 section exhibits barely any local buckling at 4% drift (Fig. 2-1a) and can reach drifts of 10% (Fig. 2-1b) to achieve a similar flange local buckling response compared to the W610×217 section at 4% drift (Fig. 2-3b). The W360×196 section has flange ($b_f/2t_f$), web (h/t_w) and global member slenderness ratios (L_b/r_y) equal to 7.2, 17.7 and 47.9, respectively, while the W610×217 section has $b_f/2t_f$ =6.1, h/t_w =33.3 and L_b/r_y = 51.7, respectively for the same parameters. The global slenderness ratios are close to one another due to the 4570 mm length of the W360 specimen compared with the 3900 mm length of the W610 section, even though the r_y of the W360×196 specimen is larger by about 25%. The web slenderness ratio of the W610×217 section is 90% larger than the web slenderness of the W360 section, which is common for deep columns and resulted in much more pronounced web local buckling, as shown in Fig. 2-3b.

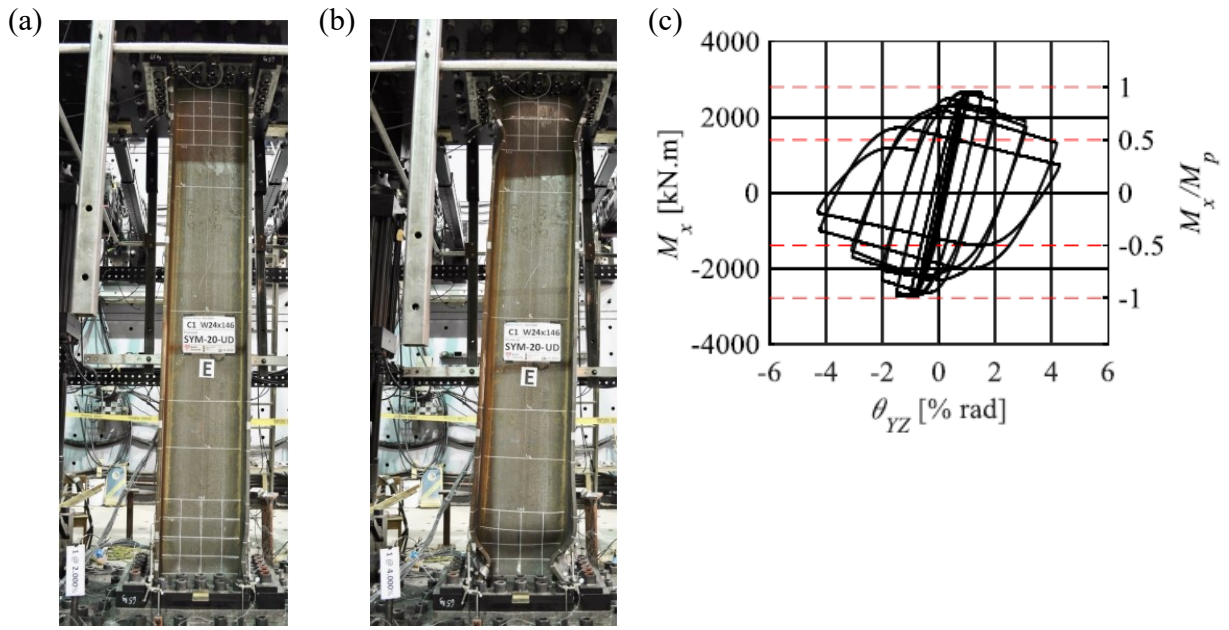

Figure 2-3. W610×217 specimen under 20% of axial load capacity: (a) 2% drift; (b) 4% drift; (c) base moment versus chord rotation response (Elkady and Lignos 2018a).

Summary of major observations from the review of the tests run by Elkady and Lignos (2018a) includes the following:

- Web and flange local buckling is usually triggered between 1.5 to 2.0% storey drift and formed at a distance of 0.5d to 0.7d from the member ends.
- None of the specimens could achieve a capacity above 0.80M_{px} at 4.0% drift at the base when subjected to the symmetric cyclic loading protocol.
- Axial shortening is a controlling failure mode for deep columns undergoing reversed cyclic loading and is heavily influenced by the magnitude of axial load. As a result, an upper limit on axial load is necessary for design practice, especially when considering low probability seismic events (2% in 50 years) to limit it below 1%L.
- Loading protocol heavily influenced the response of the deep wide-flange columns. Columns subjected to a collapse-consistent loading protocol shortened 5 times less than those subjected to symmetric cyclic loading protocol suggesting the importance of using

protocols representing realistic seismic demands to appropriately characterize the response of columns.

- Column end boundary conditions can affect their stability and strongly influences their global failure modes, and typically fixed-flexible boundary conditions lead to lower strength deterioration compared to fixed-fixed conditions.

Based on findings from the experiments conducted by Elkady and Lignos (2018a), a parametric finite element study was completed on more than 50 wide-flange columns to characterize cyclic performance indicators such as axial shortening and plastic hinge length. Particularly, an equation to quantify the extent of axial shortening was developed using the previous research conducted by MacRae et al. (1990). The result is the following equation provided by Lignos and Elkady (2018b):

$$\Delta_{\text{axial}} = 13.62 \sum \theta_{\text{pl}}{}^{1.596} \left(\frac{h}{t_{\text{w}}}\right)^{0.769} \left(1 - \frac{C_{\text{f}}}{AF_{\text{y}}}\right)^{-1.819} \tag{2-5}$$

where axial shortening Δ_{axial} is calculated in mm based on the web width-to-thickness ratio h/t_{w}, axial load ratio $C_{\text{f}}/AF_{\text{y}}$, and the cumulative plastic rotation $\sum\theta_{pl}$. The current S16 web slenderness limit of 37.0 can be obtained using Eq. 2-5 assuming a column with an unbraced length of 4600 mm and an axial load ratio of $0.30AF_{\text{y}}$ by limiting axial shortening to $1\%L$ (= 46 mm) when the cumulative plastic rotation $\sum\theta_{pl}$ = 0.25 is attained. A limit of $1\%L$ is used for axial shortening due to the observation of large out-of-plane deformations near the base plastic hinge occurring once axial shortening exceeds $1\%L$. Furthermore, it was found that the axial load cannot exceed $0.15AF_{\text{y}}$ when the web slenderness limit for high ductility members in AISC 341 or Class 1 sections in S16 is used.

Ozkula et al. (2017a) completed a large set of experiments on deep wide-flange columns as part of a comprehensive experimental program created by the National Institute of Standards and

Technology (NIST). The test matrix consisted of W610×82, W610×125, W610×155, W610×195, and W610×262 sections to cover a wide range of global, web, and flange slenderness ratios for lateral-torsional and weak-axis flexural buckling. 25 tests were completed with specimens subjected to three constant axial load ratios consisting of 20, 40, and 60% of the specimen axial capacity. The test consisted of fixed-fixed boundary conditions at member ends with displacement applied at one end based on a symmetric loading protocol representing unidirectional loading. Results from 21 specimens were discussed in the 2017 paper, 17 of which were subjected to strong axis bending, three to weak axis bending, and one to biaxial bending, respectively. Of 21 specimens, 17 were subjected to strong axis bending, three to weak axis bending, and one to biaxial bending, respectively. Fig. 2-4 shows the deformed shape of the W610×195 column at the four different levels of axial loading at 0, 20, 40, and 60% of axial capacity. A 0% axial load level specimen was included with this section to view the effect of axial load.

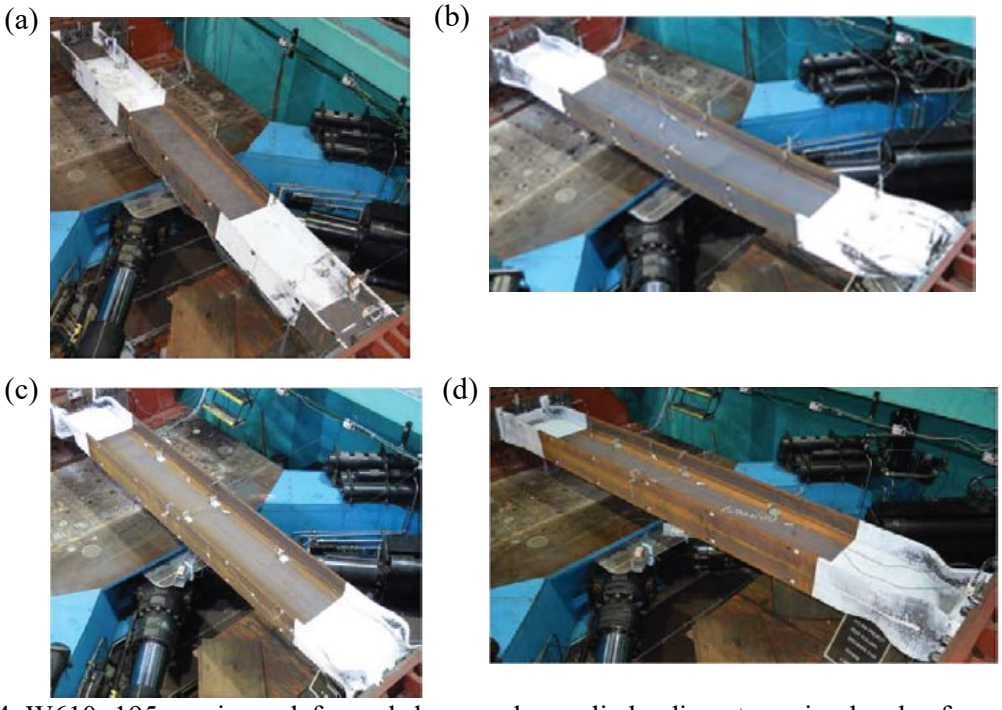

Figure 2-4. W610×195 specimen deformed shape under cyclic loading at varying levels of normalized axial load: (a) 0% axial load; (b) 20% axial load; (c) 40% axial load; (d) 60% axial load (Ozkula et al. 2017a).

Fig. 2-4 shows that increasing the axial load triggered more pronounced local buckling at lower drift and increased strength deterioration. The plastic moment capacity of the members decreased as the axial load was increased. The W610×195 specimen loaded with no axial load reached 7% drift without strength degradation or significant local buckling. In contrast, the specimens loaded with 20, 40, and 60% axial load levels were tested to only 4, 3, and 1.5% drift, respectively, since increasing the axial load level decreased the members' deformation and energy dissipation capacity. Local buckling was triggered at 3% drift for the 20% axial level specimen compared with 0.75% drift cycle at 60% axial load level. The degree of axial shortening increased as the axial load level increased, as shown in Fig. 2-5, where the axial shortening more than doubled at 1.5% storey drift when the axial load increased by 20% each time.

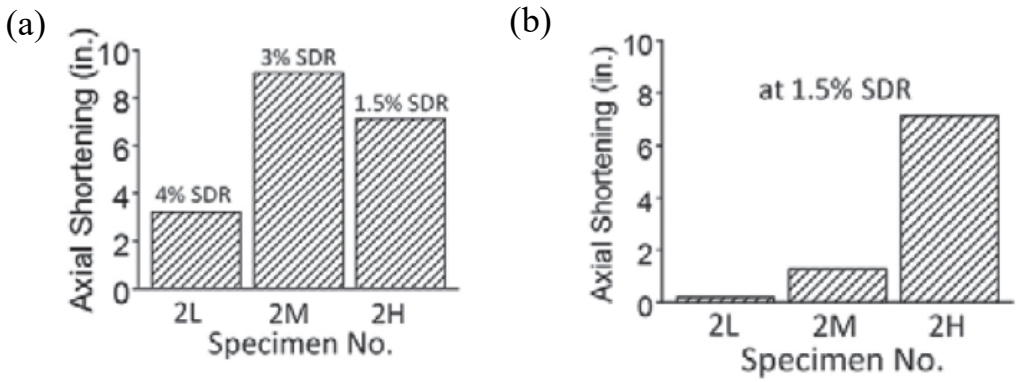

Figure 2-5. Axial shortening in inches at various storey drift ratios (SDR) for W610×195 specimens under 20% (2L), 40% (2M) and 60% (2H) axial load: (a) at end of test; (b) at 1.5% storey drift (Ozkula et al. 2017a).

The key findings of the experimental study by Ozkula et al. (2017a) are given as follows:

- The slenderness ratios for local buckling and LTB influenced the type of failure mode (local versus global buckling).
- The plastic rotation capacity of the columns decreased as the axial load was increased, and most of the strong axis bending specimens could not achieve 0.03 rad. plastic rotation.

- Axial loads caused significant local buckling and shortening.
- Sections with very low cross-section width-to-thickness ratios may trigger lateral-torsional buckling (LTB) after local buckling due to significant strain hardening increasing the yield length.

The results from the Ozkula et al. (2017a) experiments showed the critical effect of the web slenderness ratio on the response of deep columns under hysteretic loading. As a result, more stringent cross-section web width-to-thickness limits were proposed by Ozkula et al. (2021) based on the flowing equation for special moment-resisting frames (SMRF), which are the equivalent of Ductile (Type D) MRFs in S16.

$$\lambda_{hd} = \frac{h}{t_w} = 2.5(1 - C_a)^{2.29}\sqrt{\frac{E}{R_y F_y}} \tag{2-6}$$

where λ_{hd} is the term corresponding to the high ductility web slenderness limit, C_a represents the column axial load ratio based on the expected axial capacity AR_yF_y. Eq. 2-6 yields a reduced web slenderness ratio limit as the axial load increases. The experiments performed by Ozkula et al. (2017a) had fixed-fixed boundary conditions and were subjected to symmetric loading protocols. However, first-storey columns in MRFs consist of fixed-flexible members subjected to random excitations due to a seismic event. As a result, Eq. 2-6 was created using implicit factors accounting for boundary conditions and loading protocol that would better represent the actual conditions of a first-storey interior MRF column in a seismic event. Fig. 2-6 shows the proposed web slenderness limit by Ozkula et al. (2021) against the current AISC 341-16 limit for SMRFs.

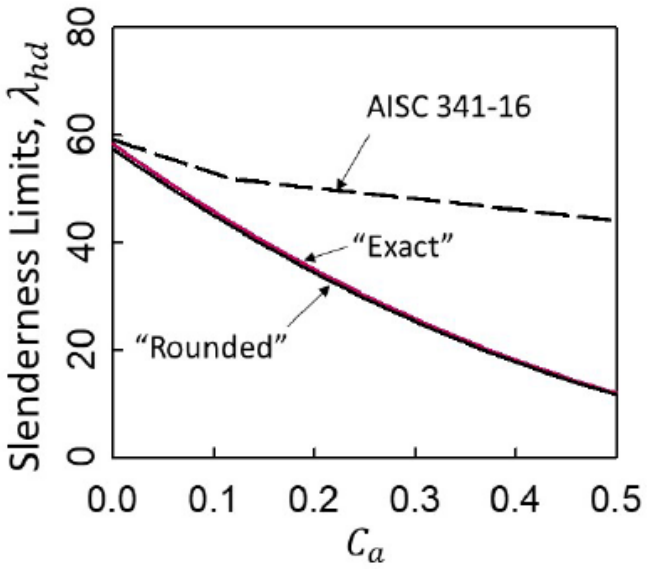

Figure 2-6. Web slenderness limits as a function of axial load proposed by Ozkula et al. (2021).

It was concluded by Ozkula et al. (2021) that the global slenderness ratio (L_b/r_y) did not significantly impact the cyclic response of columns as long it is not higher than 120. This contrasts with the current prescribed value of 50, assuming a $\kappa = 0$ and $F_y = 350$ MPa provided in Eq. 2-3 in CSA S16-19, suggesting this limit may be conservative.

Cyclic tests on 12 steel wide-flange cantilever columns under axial load and lateral drift demands were completed by Cravero et al. (2020) to investigate the influence of various loading and geometric properties, including axial loading history and cross-section width-to-thickness ratios. The test of this experimental study consisted of 1800mm-long W360×91, W460×82, and W360×122 (four of each size) under monotonic and symmetric cyclic loading protocols and varying axial load levels. The experiments showed that high compressive axial loads could compromise steel column seismic stability, but this is heavily influenced by axial loading history. Particularly, members under varying axial due to transient effects experienced local buckling initiation at the column flange experiencing the high compressive stresses while in the opposite

loading direction, the flexural resistance of the column remains at least 80% of the maximum moment up to 4% drift demand due to local buckling straightening in tension.

2.5 Reduced Beam Section Beam-to-column Moment Connections

Several pre-qualified beam-to-column connections have been utilized to design and construct steel MRFs in North America. Examples include the reduced beam section (RBS) or dog bone connection, bolted stiffened or unstiffened end plate connection, and bolted flange plate connection. The RBS connection is selected and used for the MRFs designed in this study due to its popularity after the 1994 Northridge earthquake, and there is a significant amount of research verifying the adequacy of this type of connection in providing sufficient strength and ductility under cyclic loading. Fig. 2-7 illustrates a typical RBS connection in a steel MRF.

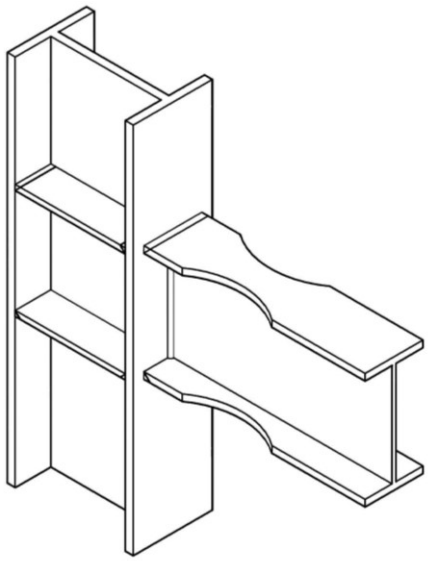

Figure 2-7. Typical RBS beam-to-column connection detail.

In RBS connections, a portion of the top and bottom beam flanges on both sides of the web are trimmed in theoretical plastic hinge locations. The flange reduced areas are located at a predetermined code prescribed distance away from the face of the column, thus ensuring that

plastic hinges form near the flange cutout and a small distance away from the column face. This prevents premature weld or connection plate fracture.

2.5.1 RBS Connections to Deep Columns

Numerous experimental test programs have been completed in the past to investigate the cyclic behaviour of RBS moment connections attached to deep wide-flange columns. Chi and Uang (2002) completed experimental tests on 3 full-scale specimens consisting of a 3.5m-long RBS connected to a 4m-long deep wide-flange section subjected to the AISC symmetric cyclic loading protocol. The test matrix was comprised of the following 3 RBS beam-to-column connections: W920×223 RBS connected to a W690×217 column section, W920×223 RBS connected to a W690×289 column section, and W690×289 RBS connected to a 690×289 column. The experiments showed that deep column sections are prone to twist due to inelastic out-of-plane buckling of RBS beams within the protected zone. An example of the out-of-plane displacement of the RBS is provided in Fig. 2-8. It is important to note that the experiments carried out by Chi and Uang (2002) consisted of only one beam-to-column moment connection representing an exterior column in an MRF.

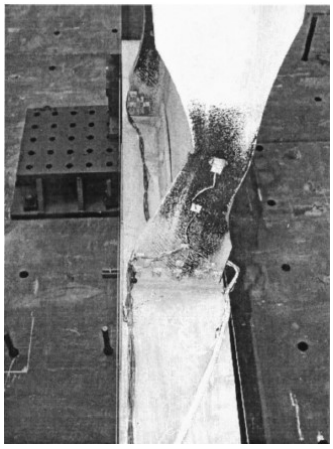

Figure 2-8. W920×223 RBS out-of-plane buckling at 4% drift (Chi and Uang 2002).

Zhang and Ricles (2006) conducted an experimental program consisting of 6 full-scale RBS beams connected to deep wide-flange columns ranging from W610 to W920 column sections. A composite floor slab was connected to four of the specimens. The two remaining specimens had no floor slab and only supplemental lateral bracing at the end of the reduced section. The specimens of this study represented the moment connection at an interior column in an MRF with moment connections on both sides of the column. The experiments showed that the composite floor slab and supplemental lateral brace effectively reduced RBS lateral movement and column twist. It is important to note that specimens with lateral bracing exhibited the least amount of column twist, suggesting that the concrete slab may have been less effective due to cracks developing in the slab at larger drifts. Figure 2-9 shows a photograph of the floor slab damage near the column face after the test.

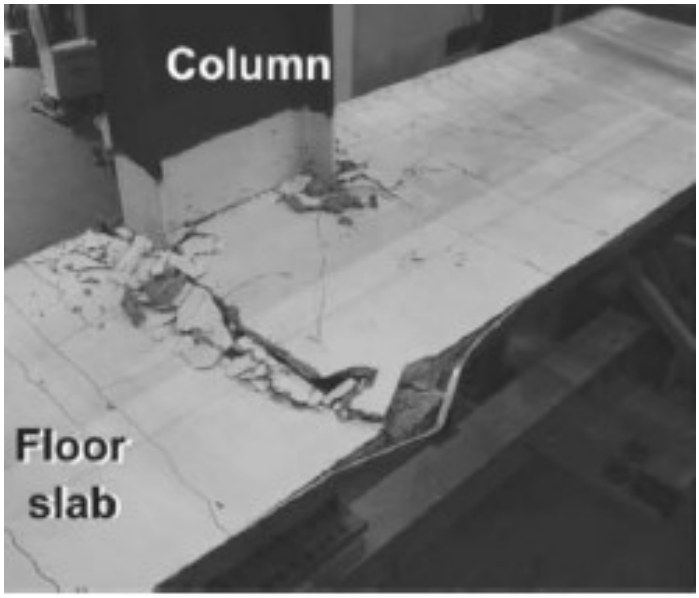

Figure 2-9. Floor slab damage at column face comprised of W920×344 RBS connected to W920×223 column (Zhang and Ricles 2006)

2.6 Numerical Modelling Techniques for Steel MRFs

Several modelling techniques have been developed to numerically characterize the behaviour of steel MRFs. This section reviews the main modelling approaches used to construct MRF models in this study.

2.6.1 Concentrated Plasticity-based Models

The nonlinear response of beams and beam-columns can be simulated using either a concentrated plasticity-based approach or a distributed plasticity approach. In the concentrated plasticity approach, beams and columns are modelled using elastic beam-column elements, and the nonlinearity of the members is lumped using zero-length rotational springs with a predefined backbone curve simulating its moment–rotation response. In the distributed plasticity approach, the member is modelled by discretizing the length into several force- or displacement-based elements with a cross-section discretized using fibres to which the nonlinear material is assigned. Concentrated plasticity models consider component deterioration at plastic hinge locations and offer computationally efficient analysis, while distributed plasticity models can explicitly capture the interaction between axial load and bending.

The modified Ibarra-Medina Krawinkler (IMK) deterioration model proposed by Lignos and Krawinkler (2011) has been widely adopted in the seismic analysis of MRFs. This model uses a monotonic backbone curve for every nonlinear element based on a moment-rotation response that accounts for the strength and stiffness deterioration of the member. Figs. 2-10 depicts the monotonic backbone curve and the modes of cyclic deterioration considered in the model.

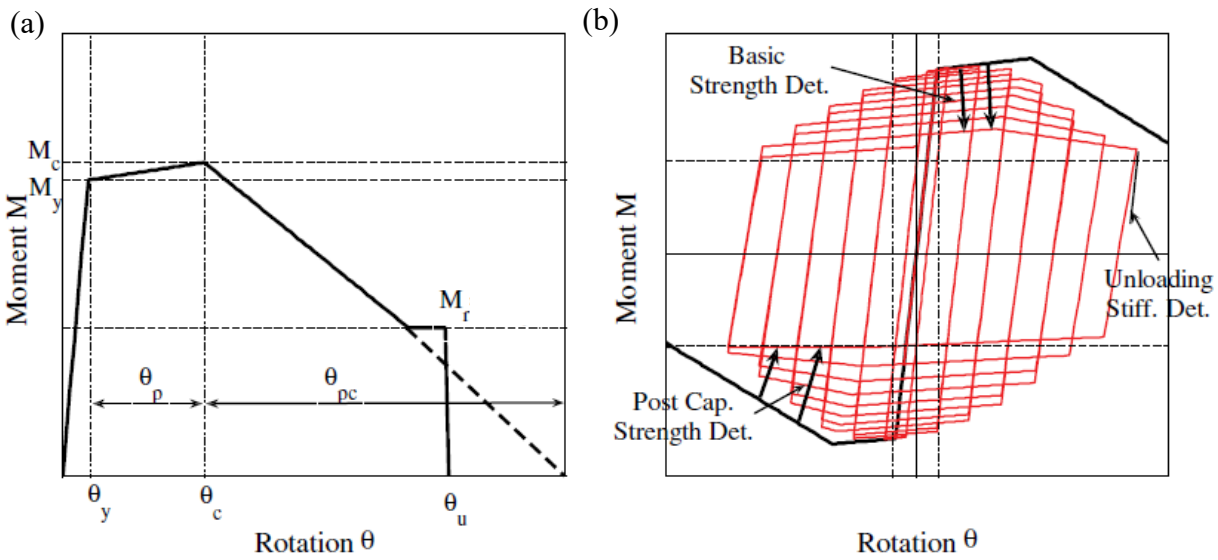

Figure 2-10. Modified IMK deterioration model: (a) monotonic curve; (b) basic modes of cyclic deterioration (Lignos and Krawinkler 2011).

In Fig. 2-10a, M_y, M_c, and M_r represent the yield, maximum or capping, and the residual moment of the member, while θ_y, θ_c, and θ_u are the yield, capping, and ultimate rotation, respectively. θ_p and θ_{pc} represent the pre-capping and post-capping rotation of the member. The modified IMK model explicitly considers strength, post-capping, and unloading stiffness deterioration. The model's moment, rotation, strength, and stiffness deterioration parameters have been calibrated using test specimens. The rotation and deterioration parameters of the beams are a function of the flange, web, global slenderness ratios, and nominal material yield strength as input parameters. For beam-column members subjected to axial loads such as the columns in MRFs, the axial load must be considered when calculating member moment, rotation, and deterioration capacities. Refined relationships are proposed by Lignos et al. (2019) for the input parameters of the monotonic backbone curves that account for the axial gravity loads applied to the beam-column.

2.6.2 Continuum-based Finite Element Models

A continuum-based finite element model (CFEM) is employed to create more accurate three-dimensional (3D) members to observe the cyclic response of structural members. In this method,

the columns and beams are discretized into fine mesh involving solid or shell elements that can explicitly capture deformations in the inelastic range of the material, strength and stiffness deteriorations, and instability. CFEMs account for residual stresses, initial imperfections, and a 3D response that cannot be observed using simplified 2D models.

2.7 Summary

This chapter summarized the 2019 Canadian steel design standard (CSA S16-19) for wide-flange steel columns part of MRFs. A summary of the extensive research on the cyclic response of wide-flange columns conducted over the past two decades but involved the design methodology adopted in the U.S. AISC Seismic Provisions was also provided. Finally, two modeling techniques often used for macro and micro modelling of steel MRF systems and components were presented.

Chapter 3. Seismic Performance of Wide-flange Columns in Ductile Steel Moment-Resisting Frames: Seismic-induced Demands, In-plane Response and Design Recommendations

3.1 Introduction

This chapter presents the evaluation of the seismic response of wide-flange steel columns of Ductile MRFs with emphasis on the stability requirements prescribed by the Canadian steel design standard and proposes improvements to the moment distribution factor used to verify column lateral bracing requirement of such columns. A combination of the concentrated plasticity-based numerical model of the MRF and continuum-based finite element model (CFEM) of the interior and exterior first-storey columns are used. A prototype Ductile MRF was used to feature three design scenarios, 1) square wide-flange columns with $d/b_f \approx 1.0$, where d and b_f are the depth and flange width of the cross-section, respectively, designed in accordance with the current CSA S16 provisions, 2) deep wide-flange columns with $d/b_f \approx 1.9$ designed in accordance with the current CSA S16 provisions, and 3) deep wide-flange columns with $d/b_f \approx 1.9$ designed excluding the special stability design provisions specified for MRF columns. Special attention is given to developing realistic seismic demands for the continuum-based finite element column model through the nonlinear response history analysis (NLRHA). The inelastic cyclic stability response of interior and exterior columns isolated from the selected MRFs are assessed using the CFEM, the proposed moment distribution factor, and the respective lateral bracing limit. Finally, the adequacy of the limiting width-to-thickness ratio for the web and axial load ratio is assessed.

3.2 Prototype Building and Loading

A five-storey office building located in Vancouver, British Columbia, Canada, on site class C was selected in this study. The building measures 63 × 45 m in the plan as shown in Fig. 3-1a with an equal beam span (= 9.0m) in both principal directions (seven bays in the longer direction and five bays in the shorter direction). The height of the first storey is 4.3m, and the upper stories are 4.0m-tall. Continuous columns are used over the first and second stories, with a splice at Storey 3 joining the lower storey columns to columns covering the rest of the building height. The lateral load-resisting system consists of Type D steel MRFs located on the perimeters in orthogonal directions. The corner columns and those between the perimeter frames only carry gravity loads. One of the perimeter MRFs in the longer direction was selected and designed in this study.

Loading was performed in accordance with the 2015 National Building Code of Canada (NBCC 2015). The live, dead, and snow load data is provided in Fig. 3-1a. The seismic load for the preliminary design was calculated using the equivalent static force procedure. The overstrength and ductility-related modification factors R_o and R_d are equal to 1.5 and 5.0, respectively. The selected building is of Normal importance with the seismic importance factor I_E = 1.0. The higher mode factor M_v is taken as 1.0. The design period, i.e., the minimum of the fundamental period obtained from a modal analysis and 1.5 times the period computed using the empirical equation, is T_a = 1.22 s, resulting in a design spectral acceleration of 0.388g. The seismic weight tributary to the selected MRF is W = 31,588 kN.

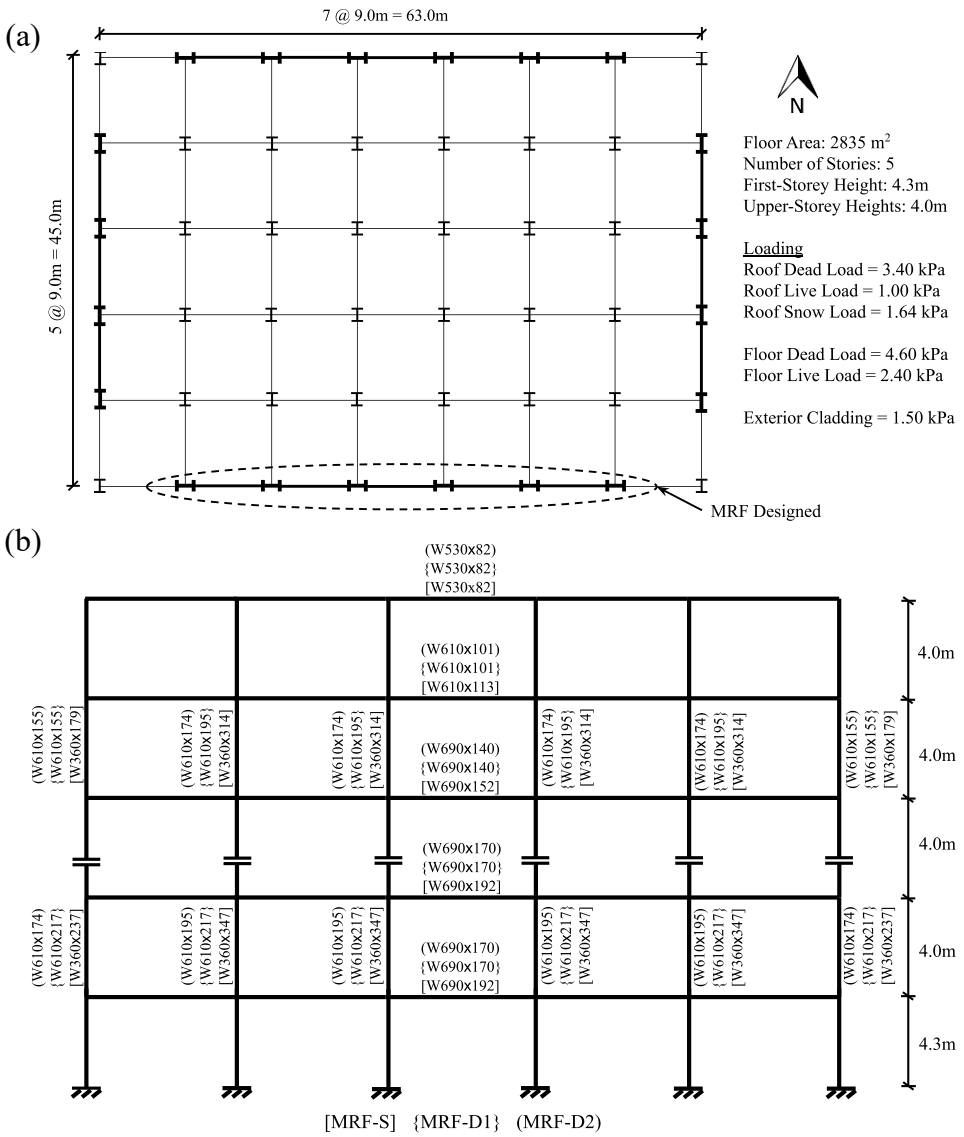

Figure 3-1. (a) Plan view of the five-storey office building selected; (b) MRF elevation and selected member sizes.

3.2.1 MRF Design

The selected MRF was designed in accordance with the 2019 edition of CSA S16. Beams and columns were selected from wide-flange (W-shape) sections conforming to ASTM A992 Gr. 50 steel with a nominal F_y and expected R_yF_y yield strength of 345 and 385 MPa. Three MRF design scenarios were examined, including 1) MRF consisting of square columns with $d/b_f \approx 1.0$ (MRF-S); 2) MRF consisting of deep columns with $d/b_f \approx 1.9$ designed to the current CSA S16 requirements (MRF-D1); and 3) MRF consisting of deep columns $d/b_f \approx 1.9$ designed to the

current S16 requirements excluding the special stability design provisions specified for columns in Eqs. 2-2 to 2-4 (MRF-D2). Deep columns are preferred in design because they can efficiently satisfy storey drift limits with a lower steel tonnage than square sections because of their higher moment of inertia for a given weight. Furthermore, deep sections provide a larger plastic moment capacity, making it possible to easily meet the strong column-weak beam check at the joints.

Reduced beam section (RBS) connections with circular radius cuts were adopted to ensure beam flexural plastic hinging occurs away from the face of the column. RBS connections were designed and detailed in accordance with CISC Moment Connections for Seismic Applications (CISC 2014). The same beam section is selected for all the bays in each storey (Fig. 3-1b). Maximum allowable flange cuts corresponding to 50% of the flange width were used for the RBS sections at the middle of the reduced area. This is preferred when drift limits govern beam sizes, as is often the case in steel MRFs.

The initial member design was performed using the equivalent static force procedure. The selected members were then used to construct an elastic numerical model in SAP2000 (CSI 2019). The lateral displacement of the frame at each storey was calculated using the model and used to adjust the member sizes so that the NBCC storey drift limit of 2.5% is met. In the model, gross cross-sections were assigned for the beams; however, the relative lateral displacements obtained from the model were amplified by a factor of 1.1 to account for the stiffness reduction in the beams due to RBS connections (CISC 2014). Once the preliminary sections were selected, a response spectrum analysis was performed to choose the final cross-sections for beams and columns. The strong column-weak beam ratio (Eq. 2-1) was verified at each design iteration at every joint. For MRF-S and MRF-D1, the stability of columns except the first-storey columns were verified using Eq. 2-2. The final sections for the three design scenarios are presented in Fig. 1b. As shown, W360

sections were selected for the columns of MRF-S, while the other two frames consist of deep W610 column sections. Both MRF-D1 and MRF-D2 have the same beam sizes to allow us easily compare only the column responses; however, heavier beams were used for MRF-S to increase the lateral frame stiffness in the presence of relatively flexible square W360 columns. The period of the first mode of vibration for MRFs-S, D1, and D2 is 1.87, 1.77, and 1.81 seconds, respectively. The reader is referred to the Elements of Earthquake Engineering and Structural Dynamics (Filiatrault et al. 2013) for additional details on the design of Type D steel MRFs.

Steel tonnage of the seismic force-resisting system members as a quantitative factor can shed light on the construction efficiency of each MRF design scenario. The comparison of steel tonnage between MRFs shows over 20% reduction in steel tonnage when deep columns are used, showing the advantage of using such sections to meet code-specified storey drift limits in design. MRF-D2 was found to be 5% lighter than MRF-D1 because of the relaxation offered when CSA S16 stability requirements are excluded.

For the first-storey columns of MRF-D1, κ in Eq. 2-3 was computed based on the moment distribution corresponding to the condition where the beams reach their full flexural capacity in the RBS region and the plastic moment capacity of the section is developed at first-storey column bases. For MRF-D2, the interior column (W610×195) has a web width-to-thickness ratio of 37.2, which is right at the limit as per Eq. 2-4, and the interaction equation for the lateral-torsional buckling limit state of columns in Storey 2 slightly exceeds unity (i.e., 1.04). The web width-to-thickness ratio for the exterior column (W610×174) is 41.0, which exceeds the limit prescribed by Eq. 2-4. This column is subjected to an axial load of $0.35AF_y$, which is above the $0.30AF_y$ limit.

Neither exterior nor interior columns of MRF-D2 satisfy the lateral bracing limit of 50 (i.e, L_b/r_y = 57 for W610×195 and L_b/r_y = 58 for W610×174).

3.3 MRF Global Response

3.3.1 Concentrated Plasticity-Based Model Development

A two-dimensional (2D) nonlinear numerical model of the MRFs shown in Fig. 3-1b was developed in the OpenSees program (McKenna et al. 1997) to study the global response of the frame using the nonlinear response history analysis (NLRHA) method. The model was constructed using elastic beam-column elements simulating the frame stiffness and overall geometry and nonlinear spring elements (i.e., zero-length) representing flexural plastic hinges at the ends of columns and beams. Beam springs were placed at the center of the RBS, while column springs were assigned outside the beam-to-column web panel zone joint at each storey. Column springs were placed at their ends at every storey to verify the possibility of plastic hinging above the base under design level seismic excitation. The properties of zero-length springs are based on the Ibarra Medina Krawinkler (IMK) deterioration model (Lignos and Krawinkler 2011). Additional details regarding this model are provided in Section 2.6.1. Nonlinear modeling parameters recommended by Lignos et al. (2019) were used to define the properties of the column springs. The moment capacity of both beams and columns in the spring models was calculated based on the expected yield strength $R_y F_y$ = 385 MPa. Using the modeling technique proposed by Zareian and Krawinkler (2009), the flexural stiffness of the rotational springs and elastic elements in between them were modified with a multiplier n = 10 to closely represent the flexural stiffness of a MRF beam-column. The strong-axis moment of inertia of beam elements was reduced by 15% to account for the negative effect of the RBS on the lateral stiffness of the frame. This reduction resulted in a 5 to 10% increase in the lateral displacement of the MRFs under the applied seismic load at each storey, which is consistent with the recommendations by FEMA 350 (FEMA 2000a). Beam-to-column

web panel zone joints were modeled using the parallelogram model (Gupta and Krawinkler 1999) with rigid elements representing the four boundaries of the panel zone joint and a trilinear rotational spring placed at one of the corners. The horizontal translation of beam-to-column joints at each storey was coupled to simulate a rigid diaphragm. The base of MRF columns was modeled as fixed support.

A P-Delta formulation was employed to account for geometric nonlinearities. A leaning column simulated by a truss element with relatively large axial stiffness and pin support at the base was included in the model to reproduce large P-Delta effects due to gravity columns tributary to the MRF. Two ends of the leaning column at each storey were simulated as a pin. The leaning column was connected to the MRF using a relatively rigid truss at each story. Lumped masses representing the tributary seismic mass of the frame were equally distributed at the top of columns at each storey. To construct the classical damping matrix, the Rayleigh damping approach with mass and stiffness proportional damping corresponding to a critical damping ratio of 2% in the first and second vibration modes was used. Mass proportional damping was assigned to the nodes with point masses, and stiffness proportional term was assigned to elastic elements (Zareian and Medina 2010). Gravity loads (C_{fg}) tributary to the MRF was applied to the top end of the MRF columns at each storey, and the remaining gravity loads were applied to the leaning column ($C_{P\Delta}$) at each storey. Nonlinear response history analyses were then performed by applying a set of ground motion accelerations in the horizontal direction. Fig. 3-2 depicts the concentrated plasticity model created in OpenSees.

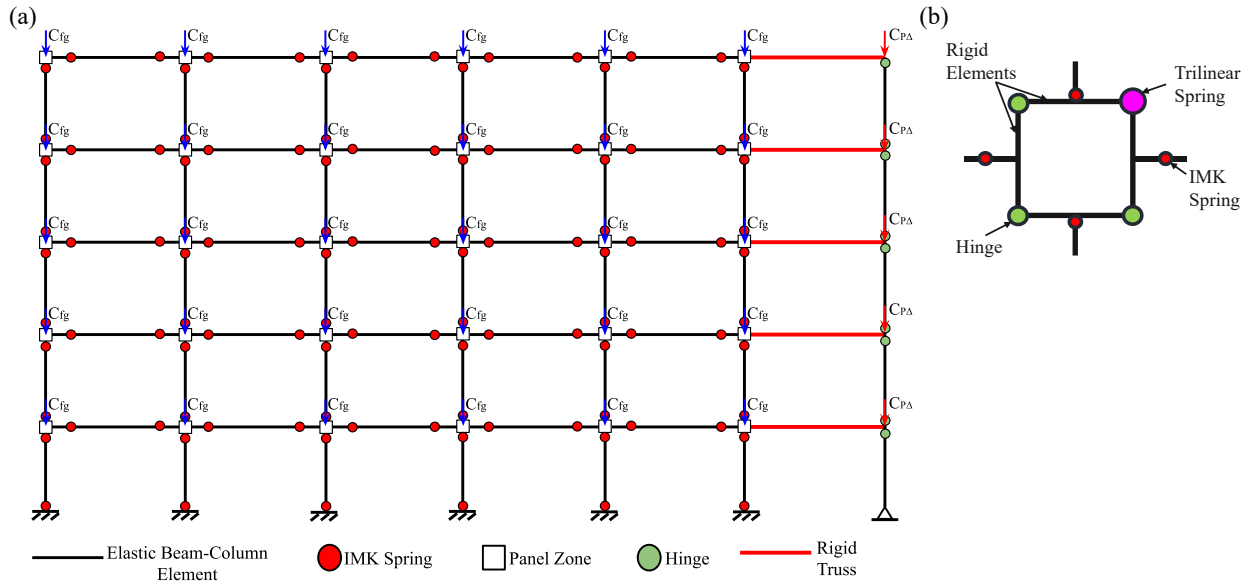

Figure 3-2. (a) Five-storey MRF concentrated plasticity model; (b) parallelogram model of beam-to-column joint panel zone.

3.3.2 Ground Motion Selection and Scaling

A suite of 33 earthquake ground motion records consisting of three earthquake scenarios likely in Vancouver, BC, crustal, deep in-slab, and interface subduction (11 records for each scenario) was selected and scaled to match on average the NBCC design response spectrum of the selected site. This corresponds to a hazard level representing a 2% probability of exceedance over 50 years of building life expectancy representing a major seismic event and is referred to as a design level excitation throughout the entire project. The selection and scaling procedures and the requirements on the various sources of earthquakes and the number of records follow the recommendations of Commentary J of the NBCC (NRC-Commentaries 2015) and those by Tremblay et al. (2015). The records were selected in each scenario using seismic deaggregation data corresponding to a hazard level of 2% probability of exceedance in 50 years in Vancouver, BC, Site Class C, based on the moment magnitude (M_w) and hypocentral distance R, defined as the distance from rupture to the recording station in km. The crustal earthquakes were selected from events having $M_w < 8.0$ and $R < 50$ km, deep in-slab records were obtained from events having $M_w < 8.0$ and $R > 50$ km, and

interface records were obtained from events having $M_w > 8.5$ and $R > 50$ km. Table 3-1 lists the event name, date, moment magnitude, and recording station for the full suite of 33 ground motions selected.

Table 3-1. Suite of Ground Motions

Source of Seismicity	ID	Event	M_w	Year	Recorded Station
Crustal	C01	San Fernando	6.6	1971	Castaic - Old Ridge Route
	C02	San Fernando	6.6	1971	Pasadena - CIT Athenaeum
	C03	Loma Prieta	6.9	1989	Coyote Lake Dam - Southwest Abutment
	C04	Loma Prieta	6.9	1989	Gilroy Array #6
	C05	Hector Mine	7.1	1999	Hector
	C06	Landers	7.3	1992	Desert Hot Springs
	C07	Northridge-01	6.7	1994	LA - Brentwood VA Hospital
	C08	Northridge-01	6.7	1994	Sunland - Mt Gleason Ave
	C09	Superstition Hills-02	6.5	1987	Superstition Mtn Camera
	C10	Morgan Hill	6.2	1984	Anderson Dam (Downstream)
	C11	Kern County	7.4	1952	Taft Lincoln School
Deep In-slab	D01	Nisqually, WA	6.8	2001	Seattle, WA Ship Canal Bridge Component
	D02	Nisqually, WA	6.8	2001	Seattle Crown Plaza
	D03	Nisqually, WA	6.8	2001	Olympia, WSDOT Test Lab
	D04	Geiyo, Japan	6.8	2001	1421a
	D05	Geiyo, Japan	6.8	2001	1421c
	D06	Geiyo, Japan	6.8	2001	4359a
	D07	Miyagi, Japan	7.1	2011	IWT026
	D08	Miyagi, Japan	7.1	2011	MYG016
	D09	Miyagi, Japan	7.1	2011	IWTH24
	D10	Olympia, WA	6.7	1949	Olympia Hwy Test Lab
	D11	Olympia, WA	6.7	1965	Seattle Federal Building
Interface	I01	Tohoku, Japan	9.0	2011	AKT017
	I02	Tohoku, Japan	9.0	2011	AKT017
	I03	Tohoku, Japan	9.0	2011	AOM008
	I04	Southern Peru	8.4	2001	POCONCHILE (A12P)
	I05	Pisco, Peru	8.0	2007	UNICA
	I06	Maule, Chile	8.8	2010	SSA2 (Santiago Centro)
	I07	Maule, Chile	8.8	2010	LACH (b)
	I08	Iquique, Chile	8.4	2014	PB09
	I09	Tohoku, Japan	9.0	2011	YMT002
	I10	Tohoku, Japan	9.0	2011	YMT009 (EW)
	I11	Tohoku, Japan	9.0	2011	YMT009 (NS)

To scale the ground motion records, a period range, 0.3 - 3.9 seconds, was selected to cover the anticipated fundamental periods of the MRFs in the study following the recommendations by Tremblay et al. (2015). Response acceleration spectra of the scaled records and the average of each suite over their corresponding period range for scaling are plotted in Fig. 3-3 against the design pseudo-spectral acceleration, S_a(g). As shown in this figure, three shorter scenario specific period ranges were then determined for each earthquake scenario. Additional information on the selection and scaling of the records can be found in Ashrafi and Imanpour (2021).

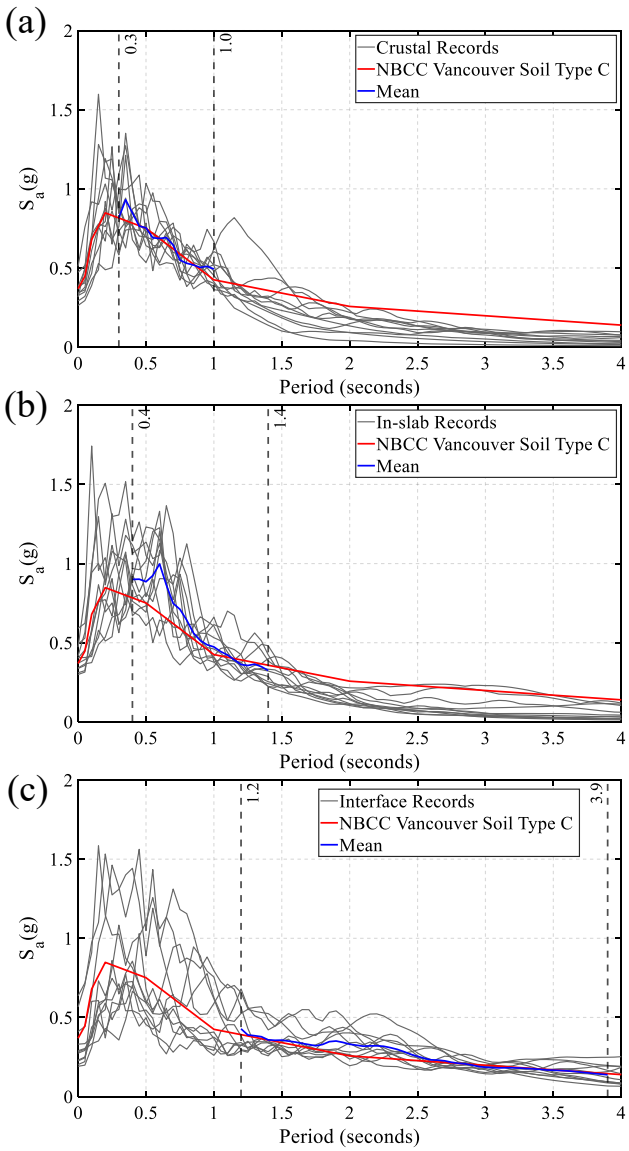

Figure 3-3. Pseudo spectral acceleration of scaled ground motion records: (a) crustal; (b) deep in-slab; (c) interface.

3.3.3 Deformation and Force Demands

The statistics of key seismic response parameters, including the storey drift ratio, column axial force, and bending moment demands, and column end rotations were calculated for each frame by taking the maximum of means over the earthquake ensembles of the peak response parameter obtained under each ground motion record as recommended by the 2015 NBCC-Commentary J (NRC 2015). It is important to recognize that interface subduction earthquakes often govern the statistics of the NLRHA for the MRFs studied here.

For all three MRFs studied, the nonlinear response involving plastic hinging at beam ends and the base of the first-storey columns was observed for the vast majority of the ground motions. Frame collapse, defined as the complete loss of storey shear resistance due to P-Delta effects accelerated by component stiffness and strength degradation (Suzuki and Lignos 2020), only occurred for MRF-D2 under the 2011 Tohoku, Japan - YMT002 (I09) record. The results associated with this record were discarded as an unacceptable response (NRC-Commentaries 2015), and the response parameters were determined using the results of the remaining records. Fig. 3a shows the profiles of storey drift ratios for the MRFs studied. As shown, MRF-S exhibits larger drift demands than the other two MRFs, which is attributed to lower flexural stiffness contributed by the columns of MRF-S. Moreover, the drift demands at the second and third stories of MRF-S exceed the code-specified limit of 2.5% mainly because of large displacements developed under 5 severe interface subduction records. The lateral displacement of MRF-D1 and MRF-D2 were appreciably lower than MRF-S for the bottom three stories, where the greatest drift demands were observed, with a reduction of 17% and 12%, respectively. This reaffirms the preference in utilizing deep wide-flange column sections to help satisfy the stringent storey drift limits prescribed by building codes. The comparison between the storey drift ratio in the first storey of MRF-D1 and MRF-D2 shows that the former experienced 16% lower drift. The statistics of residual storey drift ratios were also computed using the relative

lateral displacement of each storey at the end of each analysis. The profiles of residual storey drift ratios are shown in Fig. 3b. As shown, the residual displacements present in the building following the earthquake events created, on average, approximately 0.62, 0.54, and 0.72% drift ratio in MRFs-S, D1, and D2, respectively, across all the stories. Moreover, MRF-D2 experienced the largest residual drift ratio, on average about 20% higher than that recorded for MRF-S and 30% higher than that observed for MRF-D1 at each storey.

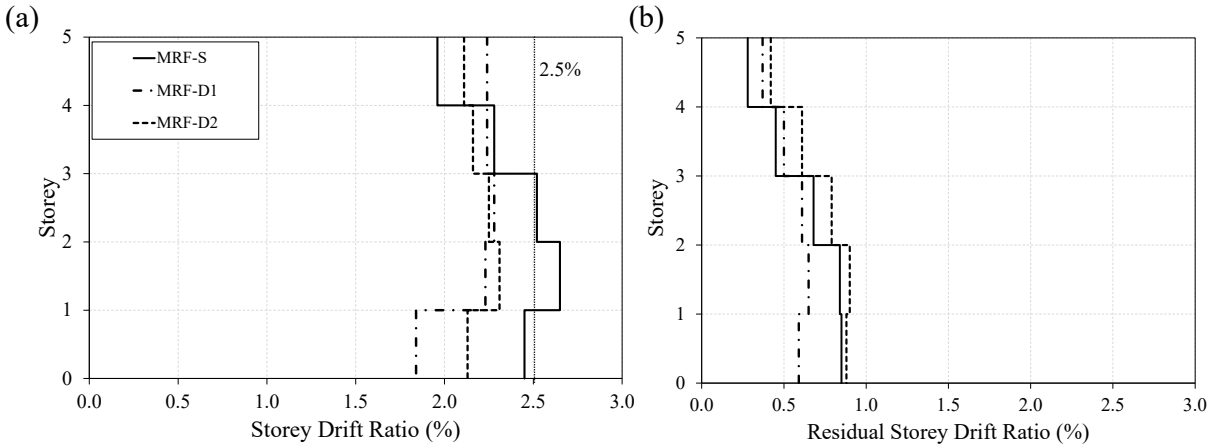

Figure 3-4. (a) Profile of peak storey drift ratios; (b) Profile of residual storey drift ratios.

Column flexural bending, axial force, and rotation at the member ends were normalized to the probable plastic moment capacity $M_{c,prob}$ given in Eq. 3-1 (Lignos et al. 2019), axial yielding capacity AF_y, and yield rotation using n = 10, respectively.

$$M_{c,prob} = 1.15 Z_x R_y F_y \left(1 - \frac{C_g}{2AR_yF_y}\right) \text{ when } \frac{C_g}{AR_yF_y} < 0.20 \quad (3\text{-}1)$$

where C_g and AR_yF_y are the column gravity load and the expected axial yield capacity, respectively. The peak response parameters and the range of each parameter are given in Table 3-2 for one of the interior columns and one of the exterior columns in Stories 1 – 5. It is worth noting that the force and rotation demands for all four interior columns and both exterior columns are nearly identical.

Table 3-2. Column bending moment, axial force, and rotation in Stories 1 – 5.

	Parameter	MRF-S		MRF-D1		MRF-D2	
		Interior	Exterior	Interior	Exterior	Interior	Exterior
5th Storey	M_x / $M_{c,prob}{}^{Top}$	0.39 (0.32-0.40)	0.36 (0.30-0.37)	0.42 (0.38-0.43)	0.28 (0.26-0.29)	0.48 (0.42-0.50)	0.28 (0.25-0.29)
	M_x / $M_{c,prob}{}^{Bottom}$	0.42 (0.25-0.60)	0.39 (0.23-0.57)	0.50 (0.29-0.66)	0.39 (0.22-0.54)	0.52 (0.30-0.68)	0.38 (0.20-0.54)
	θ_{PH} / $\theta_y{}^{Top}$	0.4 (0.4-0.4)	0.3 (0.3-0.3)	0.5 (0.3-0.5)	0.3 (0.3-0.3)	0.5 (0.5-0.5)	0.3 (0.3-0.3)
	θ_{PH} /$\theta_y{}^{Bottom}$	0.5 (0.2-0.6)	0.3 (0.2-0.6)	0.5 (0.3-0.7)	0.3 (0.2-0.5)	0.5 (0.3-0.7)	0.3 (0.2-0.5)
	C_f / AF_y	0.01 (0.01-0.01)	0.04 (0.04-0.04)	0.02 (0.02-0.02)	0.05 (0.04-0.05)	0.02 (0.02-0.02)	0.05 (0.04-0.05)
4th Storey	M_x / $M_{c,prob}{}^{Top}$	0.52 (0.36-0.62)	0.49 (0.34-0.59)	0.56 (0.31-0.66)	0.44 (0.21-0.54)	0.61 (0.36-0.72)	0.44 (0.23-0.56)
	M_x / $M_{c,prob}{}^{Bottom}$	0.60 (0.45-0.76)	0.57 (0.43-0.72)	0.75 (0.50-0.89)	0.62 (0.39-0.75)	0.80 (0.57-0.94)	0.61 (0.38-0.74)
	θ_{PH} / $\theta_y{}^{Top}$	0.5 (0.4-0.6)	0.5 (0.4-0.6)	0.5 (0.3-0.7)	0.5 (0.2-0.5)	0.7 (0.3-0.7)	0.5 (0.2-0.5)
	θ_{PH} /$\theta_y{}^{Bottom}$	0.6 (0.5-0.7)	0.6 (0.5-0.7)	0.7 (0.5-0.8)	0.7 (0.3-0.7)	0.9 (0.5-0.9)	0.7 (0.3-0.7)
	C_f / AF_y	0.03 (0.03-0.03)	0.10 (0.10-0.10)	0.06 (0.05-0.06)	0.12 (0.11-0.12)	0.06 (0.06-0.06)	0.12 (0.11-0.12)
3rd Storey	M_x / $M_{c,prob}{}^{Top}$	0.67 (0.34-0.78)	0.62 (0.32-0.73)	0.70 (0.33-0.83)	0.52 (0.26-0.74)	0.76 (0.39-0.88)	0.53 (0.27-0.79)
	M_x / $M_{c,prob}{}^{Bottom}$	0.69 (0.40-0.85)	0.65 (0.38-0.81)	0.73 (0.39-0.94)	0.55 (0.34-0.77)	0.80 (0.43-0.92)	0.55 (0.34-0.68)
	θ_{PH} / $\theta_y{}^{Top}$	0.6 (0.4-0.7)	0.6 (0.4-0.7)	0.7 (0.3-0.9)	0.5 (0.3-0.7)	0.7 (0.3-0.9)	0.5 (0.3-0.9)
	θ_{PH} /$\theta_y{}^{Bottom}$	0.7 (0.4-0.9)	0.6 (0.4-0.8)	0.7 (0.3-0.9)	0.5 (0.3-0.7)	0.9 (0.3-0.9)	0.5 (0.3-0.7)
	C_f / AF_y	0.06 (0.06-0.06)	0.18 (0.16-0.18)	0.09 (0.09-0.10)	0.20 (0.19-0.21)	0.10 (0.10-0.10)	0.20 (0.19-0.21)
2nd Storey	M_x / $M_{c,prob}{}^{Top}$	0.74 (0.40-0.82)	0.60 (0.34-0.67)	0.73 (0.46-0.86)	0.45 (0.29-0.61)	0.82 (0.48-0.92)	0.55 (0.32-0.69)
	M_x / $M_{c,prob}{}^{Bottom}$	0.66 (0.31-0.73)	0.53 (0.26-0.61)	0.73 (0.33-0.92)	0.44 (0.21-0.67)	0.80 (0.37-1.00)	0.52 (0.25-0.72)
	θ_{PH} / $\theta_y{}^{Top}$	0.7 (0.4-0.9)	0.6 (0.4-0.7)	0.7 (0.5-0.9)	0.5 (0.3-0.7)	0.9 (0.5-0.9)	0.5 (0.4-0.7)
	θ_{PH} /$\theta_y{}^{Bottom}$	0.6 (0.4-0.7)	0.5 (0.2-0.6)	0.7 (0.3-0.9)	0.5 (0.2-0.7)	0.9 (0.4-1.6)	0.5 (0.2-0.7)
	C_f / AF_y	0.07 (0.07-0.07)	0.21 (0.16-0.21)	0.12 (0.11-0.12)	0.22 (0.17-0.22)	0.13 (0.12-0.13)	0.27 (0.21-0.28)
1st Storey	M_x / $M_{c,prob}{}^{Top}$	0.69 (0.50-0.89)	0.59 (0.43-0.80)	0.61 (0.40-0.79)	0.41 (0.27-0.60)	0.75 (0.49-1.00)	0.57 (0.36-0.82)
	M_x / $M_{c,prob}{}^{Bottom}$	1.02 (0.73-1.04)	1.01 (0.69-1.06)	1.04 (0.70-1.08)	1.02 (0.62-1.08)	1.05 (0.76-1.09)	1.04 (0.71-1.08)
	θ_{PH} / $\theta_y{}^{Top}$	0.7 (0.4-0.9)	0.6 (0.4-0.8)	0.7 (0.3-0.8)	0.3 (0.3-0.7)	0.8 (0.5-1.5)	0.5 (0.3-0.8)
	θ_{PH} /$\theta_y{}^{Bottom}$	13.0 (0.8-32.6)	11.5 (0.7-30.3)	13.9 (0.7-28.2)	11.4 (0.7-25.3)	21.2 (0.8-33.4)	19.0 (0.7-31.7)
	C_f / AF_y	0.09 (0.09-0.09)	0.27 (0.18-0.28)	0.15 (0.14-0.16)	0.28 (0.19-0.29)	0.17 (0.16-0.17)	0.35 (0.23-0.36)

Referring to Table 3-2, the base moment and rotation results obtained from the base spring of the first-storey columns (both interior and exterior) indicate that flexural yielding occurred at their bases. The results of the peak base moments and rotations show that MRF-D2 columns, on average, experience the largest normalized base moments ($1.05M_{c,prob}$) and rotations ($21.2\theta_y$). The maximum value of the base moment reached $1.09M_{c,prob}$ for the interior column of MRF-D2, and the maximum

rotation $33.4\theta_y$ was observed at the base of the same interior column. No yielding occurred at the top end of the first-storey columns of MRF-S and MRF-D1; however, limited yielding was observed at the top end of the interior columns in MRF-D2 ($\theta_{PH} = 1.5\theta_y$) under the 2001 Southern Peru – POCONCHILE (I04) record, which could potentially result in the formation of a soft storey mechanism. Limited plastic rotation was also observed at the base of the second storey for the same interior column of MRF-D2 ($\theta_{PH} = 1.6\theta_y$) under the 2010 Maule-SSA2 (I06) record. Furthermore, as global frame instability occurred under the 2011 Tohoku, Japan-YMT002 (I09) record, a flexural plastic hinge formed at the top end of the interior first- and second-storey columns. Instances of flexural yielding at locations above the fixed base plastic hinge in MRF-D2 indicate that satisfying only the strong column-weak beam ratio (Eq. 2-1) may not be sufficient to ensure elastic response and prevent instability of the columns above the first storey. The verification of the in-plane and out-of-plane stability of such columns under the expected loads arising from flexural yielding in the beams are needed (i.e., Eq. 2-2). For MRF-S and MRF-D1, no yielding was observed in the upper-storey columns. The comparison between the flexural response reported for interior and exterior columns in Table 3-2 shows that exterior columns always experienced lower plastic rotations, indicating less local buckling and flexural strength degradation in such columns compared to their interior counterparts (Lignos et al. 2019). This is expected as the exterior columns are loaded by only a single connection as opposed to two for interior columns and experience fluctuating axial loads due to dynamic overturning effects compared to constant gravity loads likely in interior columns. As shown in Table 3-2, the axial loads in the interior first-storey columns of MRFs-S, D1, and D2, induced by gravity loads only, reached a maximum value of $0.09AF_y$, $0.15AF_y$, $0.17AF_y$, respectively. However, higher axial loads were observed in the exterior columns, namely, $0.27AF_y$ and $0.28AF_y$ in the first storey of MRF-S and MRF-D1, respectively, and $0.35AF_y$ in the first storey

of MRF-D2. The higher axial loads on the exterior columns are attributed to the dynamic overturning effects. The peak axial loads in the first-storey columns of MRF-S and MRF-D1 remained below 30% of the nominal axial capacity of the member, which matches well with design requirements, whereas the axial load in the first-storey columns of MRF-D2 exceeded this limit.

3.3.4 Evaluation of the Lateral Stability Requirement

The lateral bracing requirement of Eq. 2-3 was originally developed for I-shaped beams with flexural plastic hinging based on the experimental test data by Bansal (1971) (Bruneau et al. 2011). Unless the designer carries out a rational analysis, CSA S16 requires $\kappa = 0$ for the first-storey columns, which represents the moment diagram where the moment reaches nearly zero at the top end of the member while the base yields and develops its full plastic capacity under an earthquake ground motion (Imanpour et al. 2016). The factor κ was computed for the first-storey columns of the three MRF designs in this study. Fig. 3-5 shows the variation of κ with respect to the normalized top moment and storey drift ratio Δ/L, where Δ is the relative lateral displacement of the storey and L is the height of the first-storey column, for the interior and exterior columns of MRF-D1 and MRF-D2 under the 2007 Pisco-UNICA (I05) record. Since the moment at the column base is expected to reach the probable plastic moment of the section, the top moment is used here as it can represent the moment demand induced in the column under seismic loading. The top moment was calculated at the beam centreline by projecting the moment measured underneath the beam-to-column web panel zone to reproduce the moment typically used in design which is also aligned with the unbraced length of the column assumed in design.

It is apparent from Fig. 3-5 that κ tends to remain positive (i.e., member in double curvature) and often above 0.2 in particular when the storey drift ratio exceeds 2%. $\kappa \leq 0$ (i.e., member in single curvature) was observed only when the column moment demand is minimal (e.g., $< 0.2M_{c,prob}$). The observed trend for MRFs-D1 and D2, as shown in Fig. 3-5, is similar for all the columns of the three

design scenarios under all the ground motions. Additionally, interior columns always have a higher κ value than exterior columns. This is due to lower moment demands induced in exterior columns.

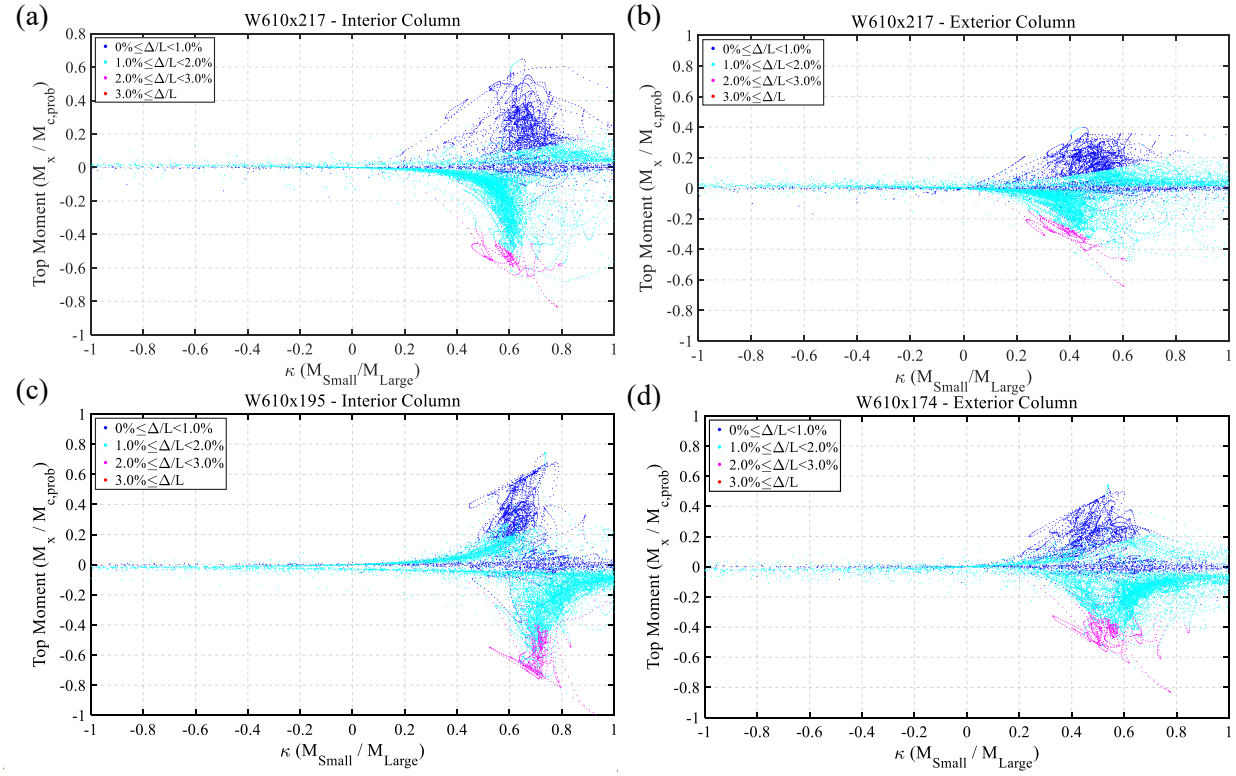

Figure 3-5. Variation of κ versus top moment and storey drift ratio for the first-storey columns under the 2007 Pisco-UNICA (I05) record: (a) MRF-D1; (b) MRF-D2.

A weighted average $\bar{\kappa}$ was computed using the κ values obtained from the NLRHA for all the first-storey columns:

$$\bar{\kappa} = \frac{\sum \kappa \times \Delta/L}{\sum \Delta/L} \tag{3-2}$$

In this equation, storey drift ratio is used as the weighting factor because column out-of-plane instability is unlikely at lower storey drift ratios with very limited yielding and local buckling at the column base (Ozkula et al. 2017a; 2017b, Elkady and Lignos 2018a). The statistics of the peak $\bar{\kappa}$ values including the range of variations are presented in Table 3-3. $\bar{\kappa}$ values vary between 0.26 and 0.77 for interior columns and between 0.11 and 0.64 for exterior columns of MRFs-D1 and D2, suggesting that the value currently prescribed by CSA, i.e., $\bar{\kappa}$ = 0, may not well represent the first-

storey column moment ratio under seismic loading. Using the minimum value of mean $\bar{\kappa}$ from Table 3-3, which is 0.63 for the interior deep columns and 0.45 for exterior deep columns and assuming F_y = 345 MPa, the lateral bracing limit from Eq. 2-3 increases to 78 for the interior and 70 for the exterior columns. This would permit the designer to use more slender columns such as W610×217 and W610×174 selected in this study for MRFs-D1 and D2, respectively. Such columns would be unacceptable for use in steel MRFs when applying the current CSA S16 provisions, i.e., the lateral bracing limit of 50. Furthermore, it was found that for both the interior and exterior columns, on average, κ remains positive over the entire set of ground motions, which is a more beneficial moment distribution for column stability, in nearly 90% of the duration of a ground motion. These results suggest the possibility of relaxing the lateral bracing limit by using a κ value larger than zero in the design of first storey MRF columns.

Table 3-3. Weighted average ($\bar{\kappa}$) for the first-storey interior and exterior columns.

Design Scenario	Location	Section	Mean $\bar{\kappa}$	$\bar{\kappa}$ Standard Deviation
MRF-S	Interior	W360×347	0.75 (0.33-0.83)	0.04
	Exterior	W360×237	0.66 (0.35-0.78)	0.07
MRF-D1	Interior	W610×217	0.63 (0.26-0.72)	0.03
	Exterior	W610×217	0.45 (0.11-0.58)	0.05
MRF-D2	Interior	W610×195	0.68 (0.35-0.77)	0.04
	Exterior	W610×174	0.53 (0.29-0.64)	0.04

3.4 First-Storey Column Response

3.4.1 Continuum-based Finite Element Model Development

A three-dimensional continuum-based finite element model (CFEM) of the first-storey column was created in the ABAQUS finite element program (Simulia 2020) to evaluate the local response of the MRF columns, in particular, verify the adequacy of the CSA S16-19 stability design requirements and propose potential improvements to these provisions. The CFEM can provide insight into the column local response with explicit consideration of initial geometric imperfections, residual

stresses, global and local buckling limit states. An isometric view of the CFEM is shown in Fig. 3-6a. The column extends from the column base to the beam centreline with a length corresponding to the MRF first storey (Fig. 3-1b). The column was simulated using four-node doubly curved, reduced integration, hourglass controlled shell elements with a uniform mesh size of 25 × 25 mm. The adjoining beams at the top end of the column, including the RBS connection and the beam outside of the reduced area were modelled using beam elements spanning half the beam span lengths (i.e., 4.5m on each side of the column centreline for the interior column and 4.5 m on one side of the column centreline for the exterior column). These beams were intended to represent the strength and stiffness of the adjoining first-storey beams assuming inflection points at the beam mid-span under the lateral seismic load. The RBS region was partitioned into five sections with the flange width adjusted along the RBS length to represent the reduced flange region. Material nonlinearity was incorporated in the model through the Maxwell-Huber-Hencky-von Mises yield criterion with associated flow rule. The nonlinear cyclic behavior of the steel material was reproduced using the Voce and Chaboche plasticity model that features combined isotropic/kinematic hardening (de Castro e Sousa et al. 2020; Hartloper et al. 2021). The material was defined using Young's modulus, E = 200 GPa, Poisson's ratio υ = 0.3, and the expected yield stress $R_y F_y$ = 385 MPa. The steel stress-strain behaviour is represented by kinematic hardening parameters consisting of C = 3378 MPa and γ = 20, while cyclic hardening parameters are equal to $Q_\infty = 90$ MPa and b = 12 (Elkady and Lignos 2018b). The residual stress distributions proposed by Galambos and Ketter (1958), in which a linear distribution is assumed in the flange and uniform tension stress is assigned to the web, were considered as shown in Fig. 3-6b. An elastic perfectly plastic material model with the expected yield stress was assigned to the RBS elements while the rest of the member outside of the reduced region was simulated using an elastic material.

Initial geometric imperfections were introduced to trigger local and global buckling in the column, as shown in Fig. 3-6c. Local imperfections were created in the web and flanges at both ends of the column to reproduce anticipated manufacturing errors (ASTM 2003) with maximum amplitudes of $b_f/150$ and $d/150$ in the flange and web, respectively. The global out-of-straightness, which is affine to the global buckling mode of the column about its weak-axis, was created in the model with a maximum amplitude of 1/1000 times the member unsupported length (AISC 2016).

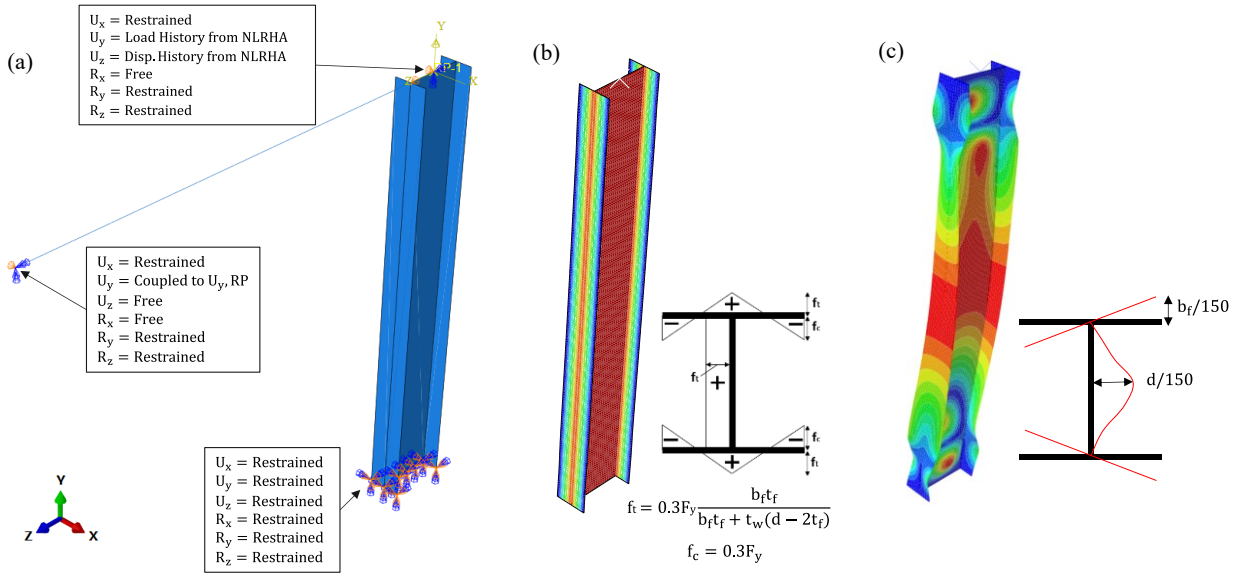

Figure 3-6. Continuum-based finite element model: (a) Boundary conditions (exterior column shown); (b) Residual stress distributions; (c) local plus global initial geometric imperfections.

Fig. 3-6a shows the boundary conditions of the CFEM. At the column base, both the translational and rotational DOFs were restrained. At the top end of the column, the translation and rotation of the column nodes were coupled to a reference point (RP in Fig. 3-6a) at the middle of the column web. The out-of-plane translation at the RP was restrained, representing the lateral support provided by perpendicular beams framing into the column at the storey level. The other two translational DOFs, including axial displacement along Y-axis and lateral displacement along Z-axis, were controlled by the axial load and displacement histories obtained from the NLRHA performed in the OpenSees. The rotation about X-axis was released as it is explicitly reproduced using the first-storey

beams, while the rotations about the other two axes were restrained to represent the flexural, torsional, and warping stiffness offered by upper-storey columns not simulated here. The translational and rotational DOFs of the beam ends are tied to those of the top end of the column to simulate the rigid beam connection. At the far end of the beams, the longitudinal movement along Z-axis and rotation about X-axis were released while the translation along X-axis and rotations about Z- and Y-axes were restrained. The vertical translation along Y-axis was set equal to the longitudinal displacement of the top end of the column. The groove welds between the beam flange and column flange and the beam web connection plates were not explicitly simulated in the CFEM. Furthermore, the beneficial effects of the concrete slab on providing the lateral support to the beams were ignored since concrete may not be effective after cracking at large storey drift ratios (Ricles et al. 2004), which is expected under major earthquake events. Geometric nonlinearity was considered through large-displacement formulations.

The CFEM was validated using the experimental test data of wide-flange MRF columns by Elkady and Lignos (2018a). For the validation study, two-column specimens consisting of W610×217 sections and two end conditions consisting of fixed-fixed and fixed-flexible were considered. Identical modeling assumptions as those described for the CFEM were used to develop the numerical model of the selected experimental specimens except that the first-storey beams of Fig. 3-6a were removed in the calibration model. Figs. 3-7a and 3-7b show base moment – chord rotation and axial shortening – chord rotation responses obtained from the CFEM developed here compared to the physical test data for the fixed-fixed and fixed-flexible specimens, respectively. It should be noted that chord rotation represents the column drift based on the length of the column decreasing due to axial shortening; this parameter is commonly used for plots throughout this

study. In this figure, M_{px} is the plastic moment capacity about the major section axis based on measured material and geometric properties, and L is the height of the column specimen.

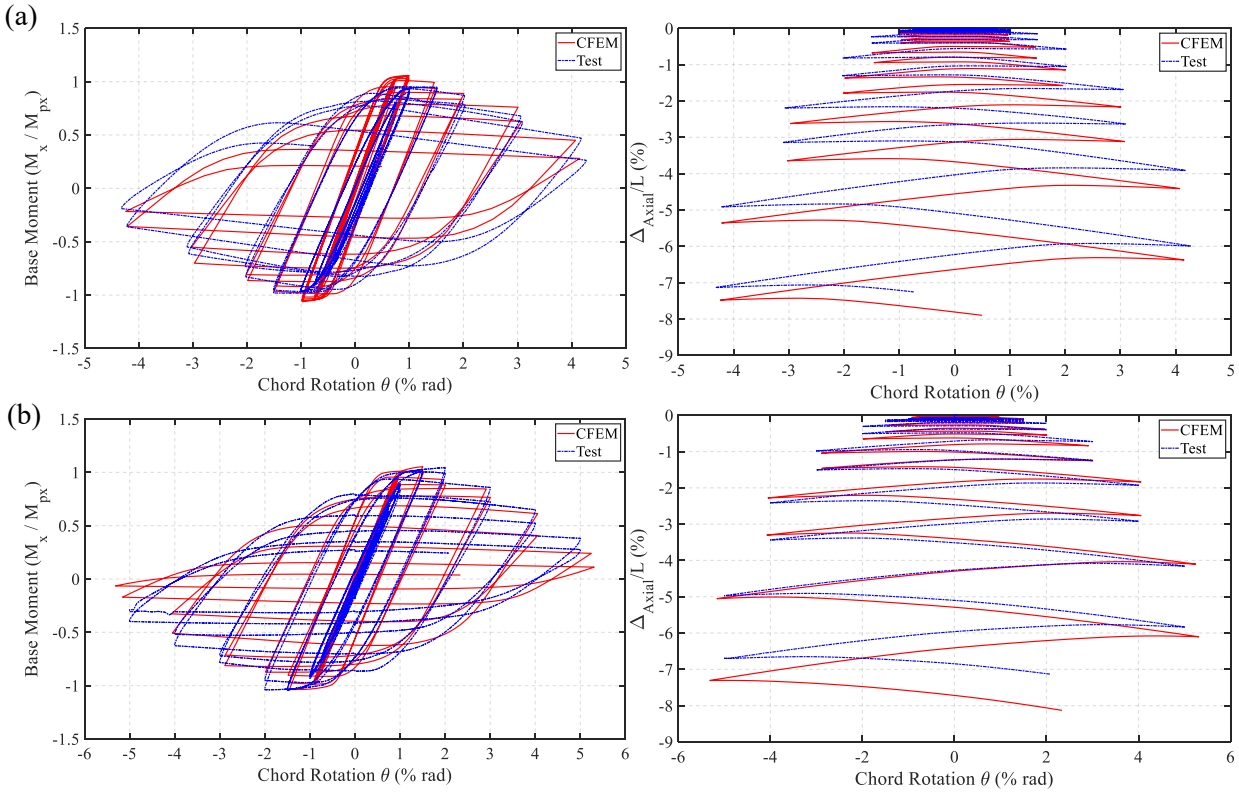

Figure 3-7. CFEM validation: (a) W610×217 specimen with fixed-fixed end condition; (b) W610×217 specimen with fixed-flexible end condition.

The comparisons shown in Figs. 3-7a and 3-7b confirm that the CFEM can appropriately reproduce the cyclic inelastic behavior of wide-flange steel columns, including flexural strength and stiffness degradations due to the flange and local web buckling as well as lateral out-of-plane deformations. The slight overestimation of the specimen moment capacity by the CFEM (Fig. 3-7a) can be attributed to the minor flexibility of the testing equipment (Imanpour 2015), which affected more the response of a fixed-fixed column specimen compared to the fixed-flexible case. The overestimation of the extent of axial shortening in both fixed-fixed and fixed-flexible cases can stem from a more critical initial imperfection amplitude used, which is likely higher than the actual initial

imperfection amplitude of the specimens (Elkady and Lingos 2018b), e.g., because of advanced fabrication practice.

3.4.2 Cyclic Response

The interior and exterior first-storey columns of the three design scenarios (MRF-S, MRF-D1, and MRF-D2) studied were analyzed using the CFEM developed here under the time history of the in-plane displacement along the Z-axis, creating strong-axis bending and the time history of the axial load along Y-axis. The displacement and load histories were obtained from the NLRHA performed using the concentrated plasticity-based model in OpenSees and were applied at the top end of the CFEM. Table 3-4 summarizes the cross-sectional properties for the interior and exterior first-storey columns.

Table 3-4. Cross-sectional properties and force capacities for first-storey columns.

Design Scenario	Location	Section	L_b/r_y	$b_f/2t_f$	h/t_w	I_x (mm^4)	C_w (mm^6)	J (mm^4)	AR_yF_y (kN)	R_yM_{px} (kNm)
MRF-S	Interior	W360×347	41.3	4.6	11.7	1.3E+09	1.6E+13	2.5E+07	17017	2749
	Exterior	W360×237	42.2	6.6	17.0	7.9E+08	9.6E+12	8.2E+06	11589	1810
MRF-D1	Interior	W610×217	56.2	5.9	34.6	1.9E+09	1.5E+13	5.6E+06	10665	2637
	Exterior	W610×217	56.2	5.9	34.6	1.9E+09	1.5E+13	5.6E+06	10665	2637
MRF-D2	Interior	W610×195	57.0	6.7	37.2	1.7E+09	1.3E+13	4.0E+06	9587	2333
	Exterior	W610×174	57.6	7.5	41.0	1.5E+09	1.1E+13	2.8E+06	8547	2064

For each design scenario, the record associated with each of the three earthquake ground motion suites (crustal, deep in-slab, interface) that yielded the largest storey drift ratio in the first storey of MRF-D2 was selected to perform the analyses and examine the design limits. The selected records were 1992 Landers – Desert Hot Springs (C06), 1949 Olympia – Highway Test (D10), and 2011 Tohoku, Japan – YMT002 (I09) for crustal, deep in-slab and interface subduction earthquakes, respectively. Among these records, the interface subduction event always produced the largest drift demands on the column compared to the other two scenarios. For MRF-D2, the 2011 Tohoku, Japan – YMT002 (I09) record resulted in frame instability at 150 seconds; thus, the analysis was only completed for the portion of the record until a chord rotation of 6.5% was reached. The applied axial

load history obtained from the selected response history analysis was relatively constant for the interior columns; however, the exterior columns were subjected to varying axial loads due to overturning effects.

Fig. 3-8 shows the normalized base and top moments versus the respective chord rotations for the interior MRF columns under the 2011 Tohoku, Japan – YMT002 (I09) record. The W360×347 column of MRF-S exhibited a stable response with significant strain hardening and without any noticeable flexural strength degradation or local buckling despite a relatively high drift demand of 4.3%. The column experienced minimal flange local buckling at its base at the end of the analysis, as shown in Fig. 3-8a. The flexural strength of the W610×217 column of MRF-D1 at its base reached $1.15R_yM_{px}$ prior to degradation at 2.8% chord rotation ratio ($1.09R_yM_{px}$) due to flange and web local buckling, which is initiated at 2.0% chord rotation but exacerbated at higher drift demands. Both W360×347 and W610×217 columns experienced minor axial shortening at the end of the ground motion with an amplitude of 0.16%L and 0.24%L, respectively. Limited yielding without local buckling was observed at the top end of these two columns.

The W610×195 column selected for MRF-D2, which is the most slender member between the interior columns of the three MRFs studied here and has a web width-to-thickness ratio close to the CSA S16 limit, experienced significant local buckling combined with limited out-of-plane deformation at the base plastic hinge, which led to significant flexural strength degradation compared to the interior column of the other two designs. The moment capacity at the base was reduced to $0.89R_yM_{px}$ at 4.0% chord rotation, which is above the threshold of $0.80R_yM_{px}$ typically used as the performance measure for beam-to-column moment connections (AISC 2016), and to $0.84R_yM_{px}$ at 6.5% rotation precipitated by severe local buckling and out-of-plane deformation at the base. Additionally, local buckling and significant flexural strength degradation occurred at the

top end of the column, confirming the soft storey mechanism observed in the NLRHA. The W610×195 column was subjected to higher axial load demands compared to the other interior columns with a maximum value of $0.17AF_y$, which combined with limited out-of-plane deformation at the base plastic hinge, and flange and web local buckling initiated at 1.6% chord rotation ratio at the base resulted in an axial shortening of $1.1\%L$ at the end of the analysis. This axial shortening is approximately four times more than the axial shortening observed for the other two interior columns.

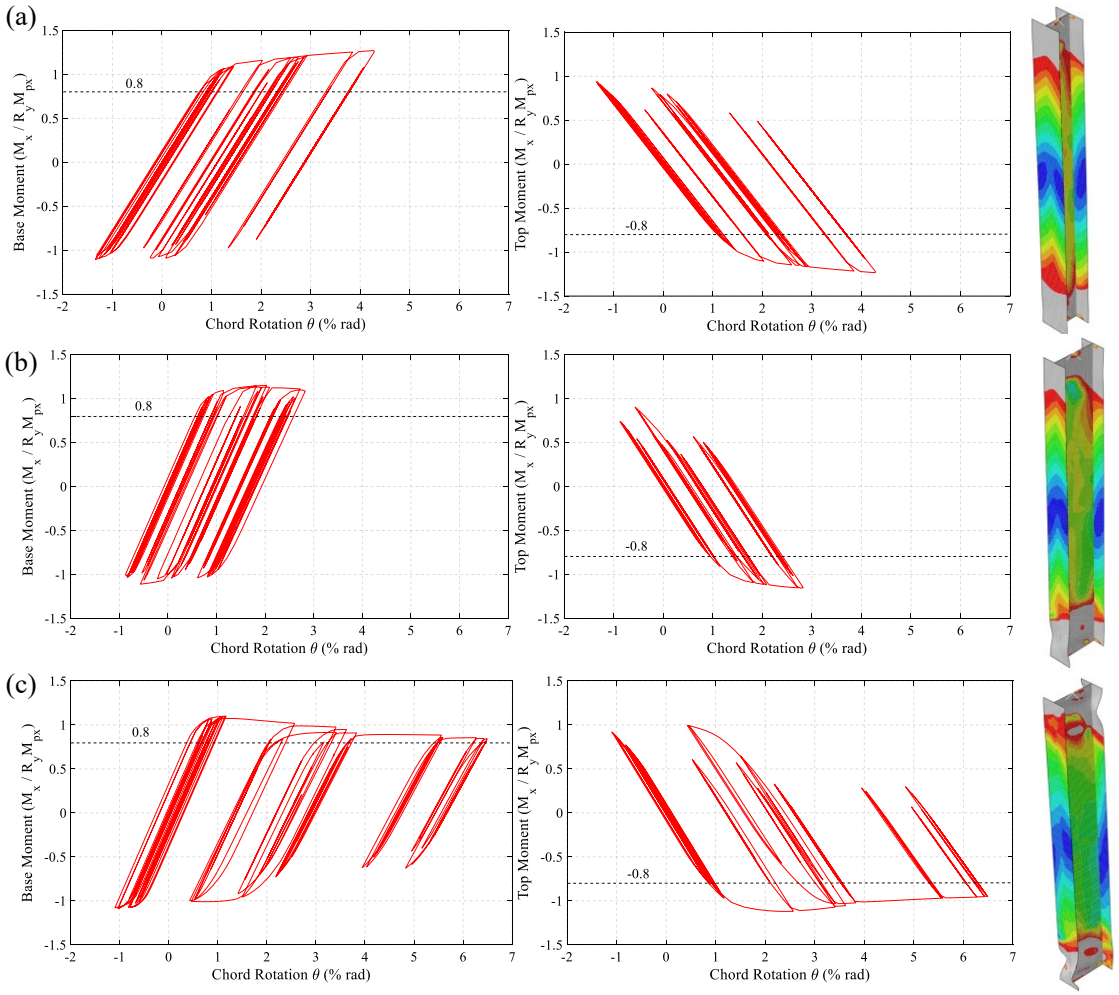

Figure 3-8. Moment – chord rotation response and deformed-shape corresponding to maximum chord rotation for the interior first-storey columns under the 2011 Tohoku, Japan – YMT002 (I09) record: (a) W360×347 of MRF-S1; (b) W610×217 of MRF-D1; (c) W610×195 of MRF-D2 (gray area represents yielding region).

The moment responses of the exterior columns subjected to the 2011 Tohoku, Japan – YMT002 record are shown in Fig. 3-9. The W360×237 column of MRF-S and W610×217 of MRF-D1 exhibit significant strain hardening without noticeable flexural strength degradation. Limited flange local buckling was observed only at the base of these columns (Figs. 3-8a and Fig. 3-8b). The maximum axial shortening reached 0.09%L and 0.08%L for W360×237 and W610×217, respectively. The W610×174 column of MRF-D2 exhibited more pronounced local buckling in the web and flanges. Local instability combined with out-of-plane deformation at the base plastic hinge reduced the moment capacity of the column to $0.97R_yM_{px}$ at 6.5% rotation. The maximum axial shortening recorded at the end of the analysis was equal to 0.6%L, which is nearly six times that of W360×237 and W610×217 columns. The W610×174 column has a web slenderness ratio of 41.0 and experienced a maximum axial load of $0.35AF_y$; both values are above the code-specified limits for columns with anticipated base plastic hinging. Exterior columns, on average, experienced lower flexural strength degradation than interior columns, which are under higher bending and a constant gravity-induced axial load.

The responses of the interior and exterior columns under the crustal and deep in-slab ground motion records followed the trend observed under the interface subduction record with the column sections of MRF-D2 showing the most severe local instability and greatest strength degradation, although no collapse was recorded under the crustal and deep in-slab records. Moment and drift demand under the crustal and deep in-slab records was always less than the interface ground motions. For instance, storey drift ratios remained below 2.5%, and the first-story columns' moment capacity did not fall below $1.0R_yM_{px}$. It is worth noting that the stable responses observed for the W360 sections of MRF-S align well with past experimental studies (Newell and Uang 2008).

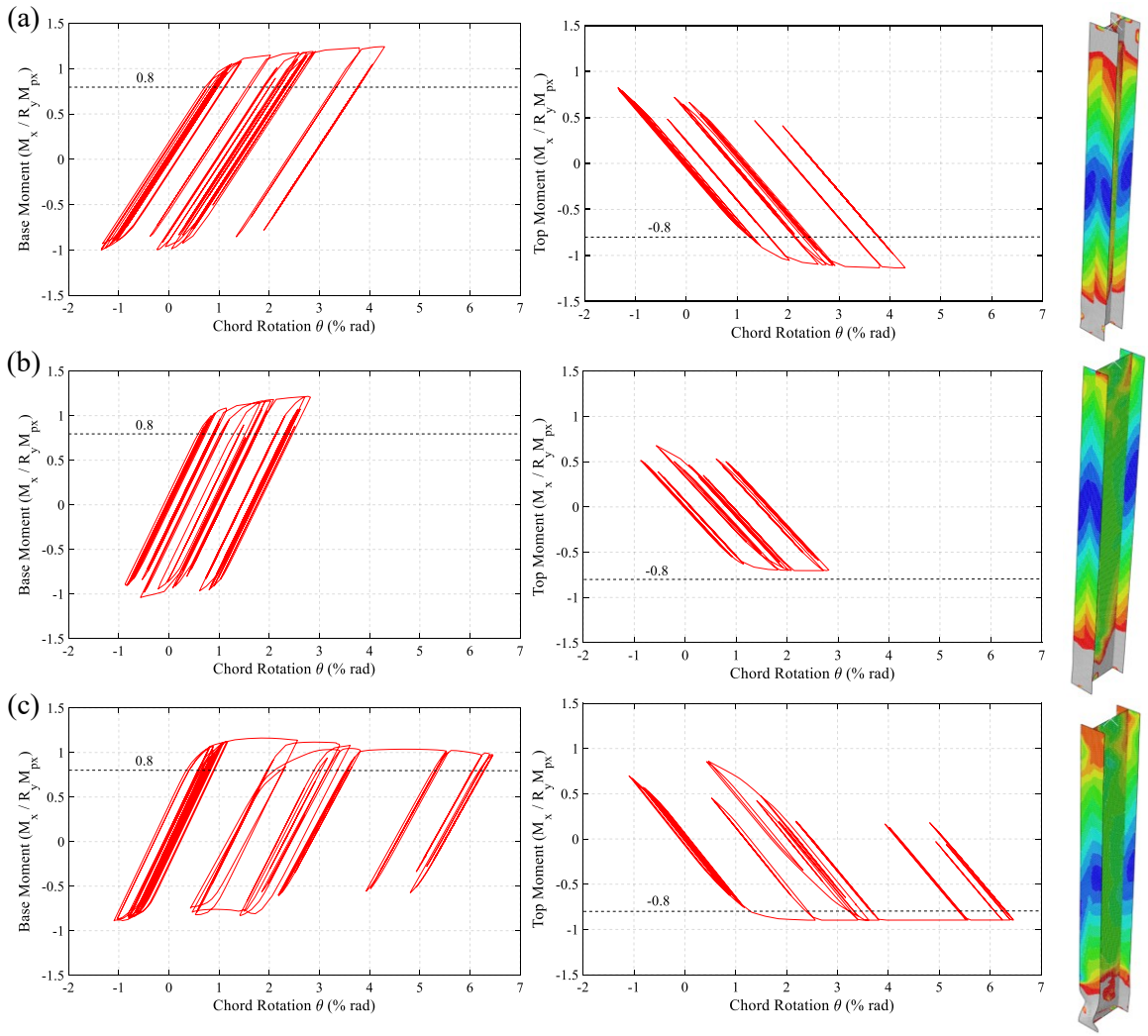

Figure 3-9. Moment – chord rotation response and deformed-shape corresponding to maximum chord rotation for exterior first-storey columns under the 2011 Tohoku, Japan – YMT002 (I09) record: (a) W360×237 of MRF-S1; (b) W610×217 of MRF-D1; (c) W610×174 of MRF-D2 (gray area represents yielding region).

The results of the CFEM analyses showed no member instability or excessive out-of-plane deformations for the deep interior and exterior columns of MRF-D1, which both violate the lateral bracing limit of 50 assuming κ = 0 (see Eq. 2-3). As such, this lateral bracing requirement is deemed conservative. This observation is further reinforced by the findings of the NLRHA for the κ factor described in Section 3.3.4. Moreover, the comparison between the results of MRF-D1 and MRF-D2 columns shows the necessity of stability requirements such as Eqs. 2-2 and 2-4 for MRF columns with base plastic hinging. Had such stability requirements been neglected in the design

of MRF-D1 columns, the instability mode similar to that observed under the 2011 Tohoku, Japan – YMT002 (I09) record would have been expected, which could have led to frame collapse.

3.4.3 Influence of Axial Load

Column axial shortening was used to evaluate the compressive axial load limit for the first-storey columns. For the columns studied here, the record associated with each of the three earthquake ground motion suites (crustal, deep in-slab, interface subduction) yielded the largest storey drift ratio in the first storey MRF-D2 was used. The maximum normalized axial shortening Δ_{axial}/L under each ground motion record is plotted against the maximum value of the normalized compressive axial load $C_{f,max}/AF_y$ under the same record in Fig. 3-10a, and the maximum normalized out-of-plane displacement along the member length $\Delta_{out\text{-}of\text{-}plane}/L$ is plotted against the member slenderness ratio L_b/r_y in Fig. 3-10b. The interface subduction ground motion yielded the largest values for both parameters.

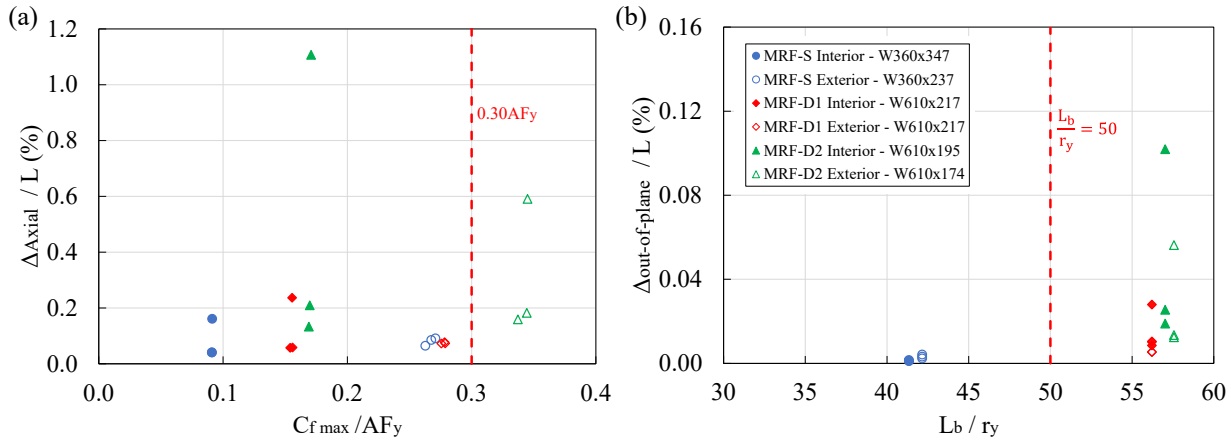

Figure 3-10. (a) Normalized axial shortening versus compressive axial load ratio; (b) Normalized out-of-plane deformation along the member length.

Referring to Fig. 3-10a, axial shortening increased due to higher axial loads, confirmed by the past experimental studies (Elkady and Lignos 2018a). Moreover, the columns of MRF-D2 experienced the largest axial shortening (i.e., 1.1%L for interior and 0.6%L for exterior columns). Past full-scale

experimental tests (Elkady and Lignos 2018b) showed that large out-of-plane deformations are expected near the base plastic hinge region when the column axial shortening exceeds 1%L. Such out-of-plane deformations can cause considerable weak-axis moments due to member P-Delta forces, particularly when the column experiences large drift demands. The current stability design requirements in CSA S16 neglects explicitly checking column axial shortening and instead attempts to control axial shortening by limiting the width-to-thickness and compressive axial load ratios. Both are more quantitative design parameters as compared to axial shortening. Finally, the evaluation of the axial load demand for interior columns shows that the gravity-induced axial load of interior columns in a well-designed MRF is significantly lower than $0.30AF_y$, i.e., $0.09AF_y$, $0.16AF_y$, and $0.17AF_y$ in MRF-S, MRF-D1, and MRF-D2, respectively. The axial load ratio can be higher (e.g., $0.40AF_y$) in existing MRFs (Bech et al. 2015).

The most critical peak out-of-plane displacements were observed for the W610×195 column with an amplitude of 0.10%L (Fig. 9b). Although this column meets the axial load ratio of $0.30AF_y$, the out-of-plane deformation combined with the observed axial shortening of 1.1%L suggests that the axial load limit alone may not be sufficient to limit axial shortening and subsequent strength degradation.

Referring to Figs. 3-10a and 3-10b, exterior columns of all three design scenarios always have smaller shortening and out-of-plane displacement compared to their interior counterparts. Although the axial load of an exterior column can reach and exceed the $0.30AF_y$ limit, they experienced lower axial shortening (e.g., <1.0%L) due to the benefit of dynamic overturning effects, which reduces their axial compression load. This suggests that the axial load limit of $0.30AF_y$ can be relaxed for exterior columns.

3.4.4 Influence of Section Compactness

Web and flange out-of-plane deformation near the column base plastic hinge where local buckling develops were measured for the columns studied. Fig. 3-11 shows the peak values of web and flange deformations normalized by the web clear depth h and half of the flange width $0.5b_f$, respectively. As shown, the smallest amplitude was always observed for the columns of MRF-S. This is partly attributed to the role of lower section slenderness ratios in delaying local buckling, which is consistent with the observations of past experimental studies (Newell and Uang 2008). Although sections conforming to Class 2 web or flange were not investigated in this study, the trend observed in Figs. 3-10a and 3-10b suggest that the specified Class 1 limit for the flange, Class 1 limit for the web of the columns with an axial load ratio lower than $0.15AF_y$, and $700/(F_y)^{0.5}$ limit for the web of the columns with an axial load ratio exceeding $0.15AF_y$ are necessary to prevent severe local buckling at the plastic hinge region and in turn limit axial shortening. Referring to Figs. 3-11a and 3-11b, both interior and exterior columns of MRF-D2 showed the largest local buckling amplitudes. Notably, the web deformations observed in MRF-D2 columns with a width-to-thickness ratio near the limit of (i.e., 37.0) are more than two times those recorded for MRF-D1 under the same ground motion record.

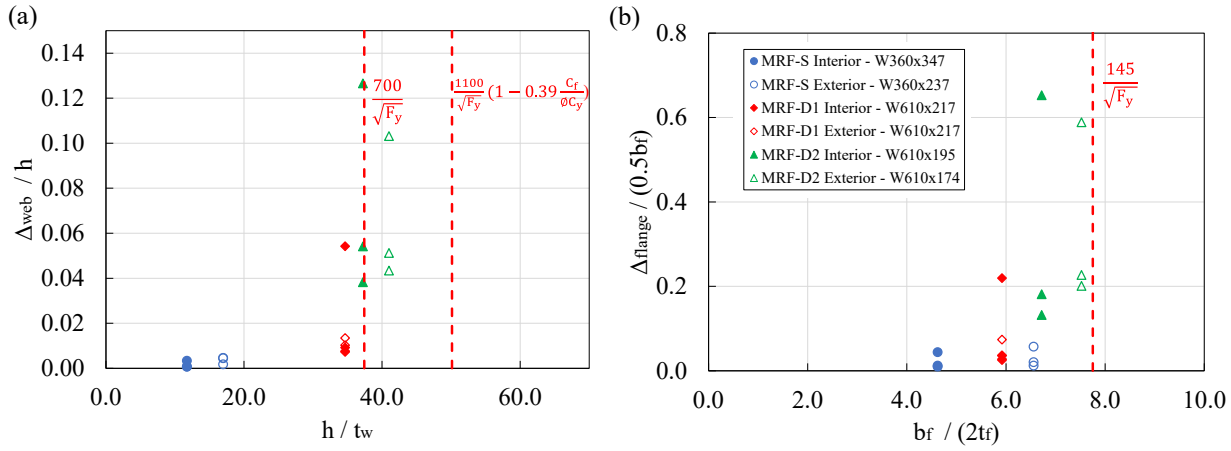

Figure 3-11. (a) Normalized web displacement – web slenderness ratio; (b) Normalized flange displacement – flange slenderness ratio.

Flexural strength degradation and local buckling amplitudes observed in this study for the W610×195 column of MRF-D2 reaffirms the need for a strict width-to-thickness limit for such first-storey fixed-base columns in steel MRFs. This is consistent with a more stringent width-to-thickness ratio for the web proposed in Eq. 2-5 and more recently by Ozkula et al. (2021) in Eq. 2-6 based on full-scale experimental testing of deep wide-flange columns. The current width-to-thickness limit of 37.0 for the columns under axial load ratios above $0.15AF_y$ is based on the relationship between axial shortening, cumulative plastic rotation demand, axial load, and web width-to-thickness ratio as given in Eq. 2-5. The web width-to-thickness ratio in both Eq. 2-5 and 2-6 decreases as the member axial load increases, as shown in Fig. 3-12.

Figure 3-12 also compares the limits of Eqs. 2-5 and 2-6 with that of the CSA S16-19 by varying the axial load ratio. The web slenderness limit for Class 1 sections is used for the axial load ratios below $0.15AF_y$ in the figure for CSA S16. The web width-to-thickness ratio of the first-storey columns of the MRFs studied here are also shown at the maximum axial compression load observed under the 2011 Tohoku, Japan - YMT002 (I09) record. As shown in Fig. 3-12, the CSA S16 limit is less conservative when compared to the limit proposed by Ozkula et al. (2021), while Eq. 2-5 yields a more relaxed limit. This can be attributed to the fact that Eq. 2-6 does not explicitly account for the effect of axial shortening and takes a more conservative approach to account for boundary conditions, loading protocol, and axial load history. Moreover, the CSA S16 limit beyond the axial load ratio of 0.3 is not applicable because columns having an axial load ratio exceeding 0.3 are not permitted for the first storey by this standard. Furthermore, the limits were based on interior columns and are on the conservative side for exterior columns since such columns benefit from heavily fluctuating axial loads due to dynamic overturning effects. It should be noted

that higher axial load levels than what is assumed here should be considered in future studies to further evaluate the S16 limit. Section 4.6.6 presents the results for one set of higher axial loads.

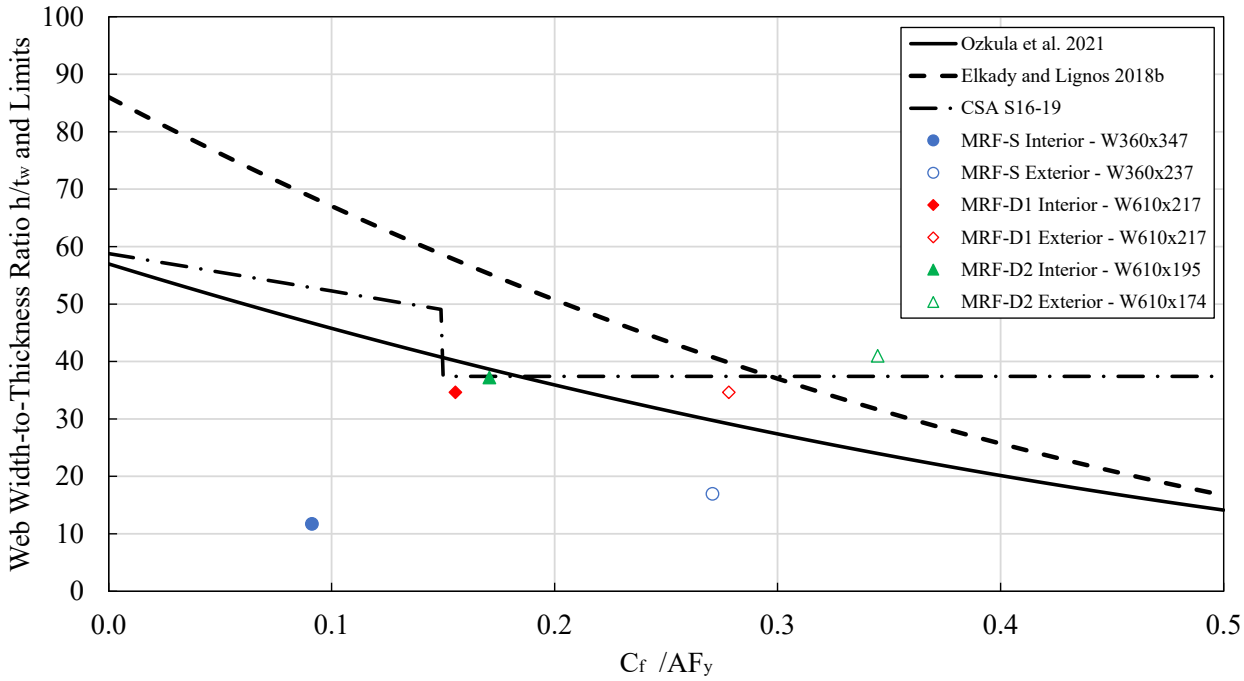

Figure 3-12. Comparison of web width-to-thickness ratios and limits.

3.4.5 Modelling Limitations and Differences

This chapter used two modelling techniques: the two-dimensional concentrated plasticity-based model of the MRFs and the three-dimensional continuum-based finite element model of the isolated first-storey column. The concentrated plasticity-based model utilizes an empirical moment-rotation backbone curve based on past experimental data, which implicitly accounts for isotropic and kinematic hardening of steel. The CFEM model, however, explicitly accounts for the stress-strain response of steel, including kinematic and cyclic responses, residual stresses, initial geometric imperfections, and 3D effects such as local buckling and axial shortening. The results obtained from the concentrated-based model should be treated with caution due to several modelling assumptions implicit in this technique. For instance, Fig. 3-13 compares the moment-chord rotation response of the interior W610×217 column of MRF-D1 under the 2011 Tohoku, Japan – YMT002 earthquake. As shown in Fig. 3-13a, the strength degradation at large chord

rotations was not well predicted by the concentrated-plasticity modelling technique. This stems from the fact that local buckling explicitly accounted for in the continuum-based model is triggered earlier than implicit consideration of local buckling in the concentrated plasticity-based model. Additionally, it is important to note that the moment response at the top end of the column was overestimated in the continuum-based model; the moments from the two adjoining beams would be distributed among the first and second storey columns as was the case in the concentrated-plasticity based model. This top moment from ABAQUS is deemed to be on the conservative side.

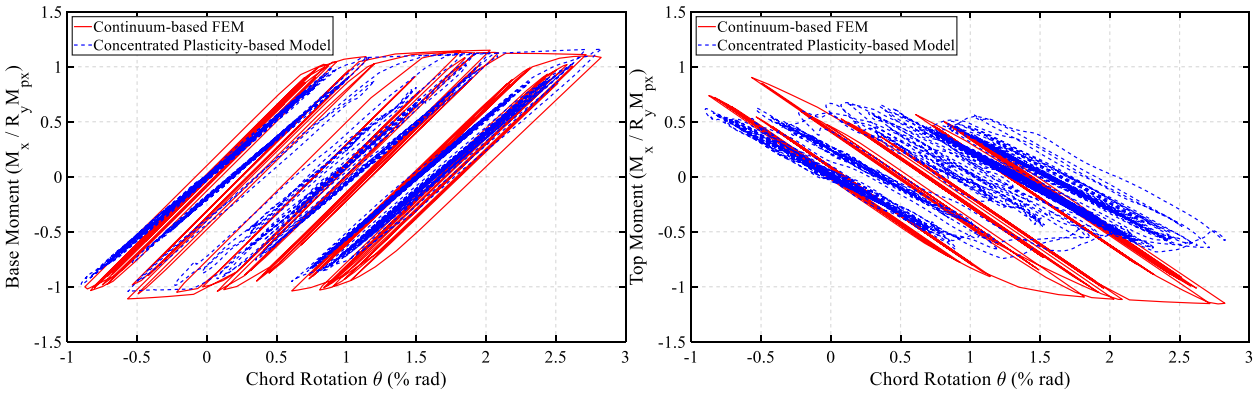

Figure 3-13. Moment – chord rotation response of the interior first-storey column of MRF-D1 (W610×217) under the 2011 Tohoku, Japan – YMT002 earthquake, ABAQUS vs. OpenSees.

3.4.6 Summary

The stability design requirements prescribed by the 2019 Canadian steel design for columns of Ductile MRFs significantly improved the seismic performance of such frames under major seismic events expected in high seismic regions of Canada. However, these requirements can be improved further.

The NLRHA results confirmed that the current CSA S16 lateral bracing limit of $L_b/r_y = 50$ (assuming $\kappa = 0$ and $F_y = 345$ MPa) is highly conservative, and $\kappa = 0.45$ can be used in design, which results in $L_b/r_y = 70$. This new limit would permit more deep W-shape sections as columns in steel MRFs, creating a broader column selection for designers. This relaxation is supported using the results obtained from CFEM analyses of wide-flange columns exceeding the current lateral

bracing limit as neither member instability nor excessive strength degradation was observed under gravity plus seismic-induced demands.

The current CSA S16 axial load limit of $0.30AF_y$ primarily influences the selection of exterior columns for which the axial load can approach or exceed this limit due to dynamic overturning effects. This limit can be increased to $0.35AF_y$ for the exterior columns as they are subjected to lower moments and varying axial load demands, making them less prone to severe strength degradation.

The limiting width-to-thickness ratio h/t_w of 37 for the web of wide-flange members in CSA S16 appears to be adequate based on CFEM analyses for columns around an axial load ratio of $0.15AF_y$ performed considering the effects of influential parameters including axial shortening, cumulative plastic rotation demand, and axial load. However, this limited still needs to be confirmed under constant axial load ratios larger than $0.15AF_y$.

Chapter 4. Seismic Performance of Wide-Flange Columns in Ductile Moment-Resisting Frames: Three-Dimensional Response and Stability Design Recommendations

4.1 Introduction

This chapter aims to propose new seismic design recommendations for the wide-flange steel columns located in the first-storey of steel moment-resisting frames by leveraging the numerical results obtained from a more comprehensive CFEM that includes the beams and columns of the upper stories, referred to as subassembly model, and by building on the findings presented in Chapter 3 concerning the seismic design requirements specified in the current Canadian steel design standards. The selected perimeter frame of the five-storey prototype building presented in Section 3.2 was designed in this chapter with the first-storey column sections that have a global slenderness ratio L_b/r_y higher than 80 and a d/b_f larger than 2.0 as such cross-sections can be prone to global instability under cyclic loading at high drift demands (Elkady and Lignos 2018b). The CFEM of the selected MRF's subassembly that includes all five stories five-storey was then created. The subassembly model was meant to undo simplifications made in the isolated column model of Chapter 3, i.e., the beam-to-column RBS connections, beam-to-column web panel zone joint, adjacent exterior column, upper-storey columns, and beams, which would better reproduce the seismic-induced demands on the first-storey column considered here by taking into account the redistribution of plasticity, stiffness of the adjoining beams and columns, influence of exterior column uplift, and torsional and out-of-plane moment demands arising from the RBS connections. The results from the NLRHA of the subassembly model were subsequently used to develop a loading protocol representing the out-of-plane bending anticipated on the interior first-storey column. A virtual test matrix of 26 isolated first-storey interior columns was created by varying

L_b/r_y, h/t_w, and d/b_f ratios. The virtual specimens are subjected to the cyclic loading protocols in and out-of-plane in the presence of a constant axial load. The results of this parametric study were finally used to make seismic design recommendations for enhanced design of wide-flange columns located in the first storey of steel MRFs in the framework of the Canadian steel design standard.

4.2 Building Selected and Loading

A five-storey office building located in Vancouver, British Columbia, Canada (representing a high seismic region in Canada) on site class C was selected to evaluate the seismic response of steel MRFs, focusing on the stability of first-storey wide-flange columns. The plan view of the building is shown in Fig. 4-1a. The dimensions of the building in the plan are 52.5 × 37.5 m. The loading data and storey heights are kept the same as those described in Section 3.2. One of the perimeter frames in the long direction, as shown in Fig. 4-1a, was selected and designed as a Ductile (Type D) MRF.

Loading calculations were performed in accordance with the 2015 NBCC. In the calculation of gravity loads, it was assumed that the secondary beams run in the North-South direction of the plan view and transfer gravity loads to the beams of the MRF considered here. The seismic base shear for the preliminary design was calculated using the equivalent static force procedure performed by hand. The building is of Normal importance with the seismic importance factor I_E = 1.0. The higher mode factor M_v is taken as 1.0. The overstrength and ductility-related modification factors specified for Ductile MRFs are R_o = 1.5 and R_d = 5.0, respectively. The design period, i.e., the minimum of the fundamental period obtained from a modal analysis and 1.5 times the period computed using the empirical equation, is T_a = 1.22 s, resulting in a design spectral acceleration of 0.388g. The seismic weight tributary to the selected MRF is W = 22,347 kN. The accidental torsion, notional load, and P-Delta effects were considered in the calculation of the design base

shear. Response spectrum analysis was then performed to obtain a more realistic seismic force distribution and lateral deflections of the frame using a computer model constructed in SAP2000 (CSI 2019). As per NBCC, the base shear obtained from the response spectrum analysis was scaled using the base shear obtained from the equivalent static force procedure.

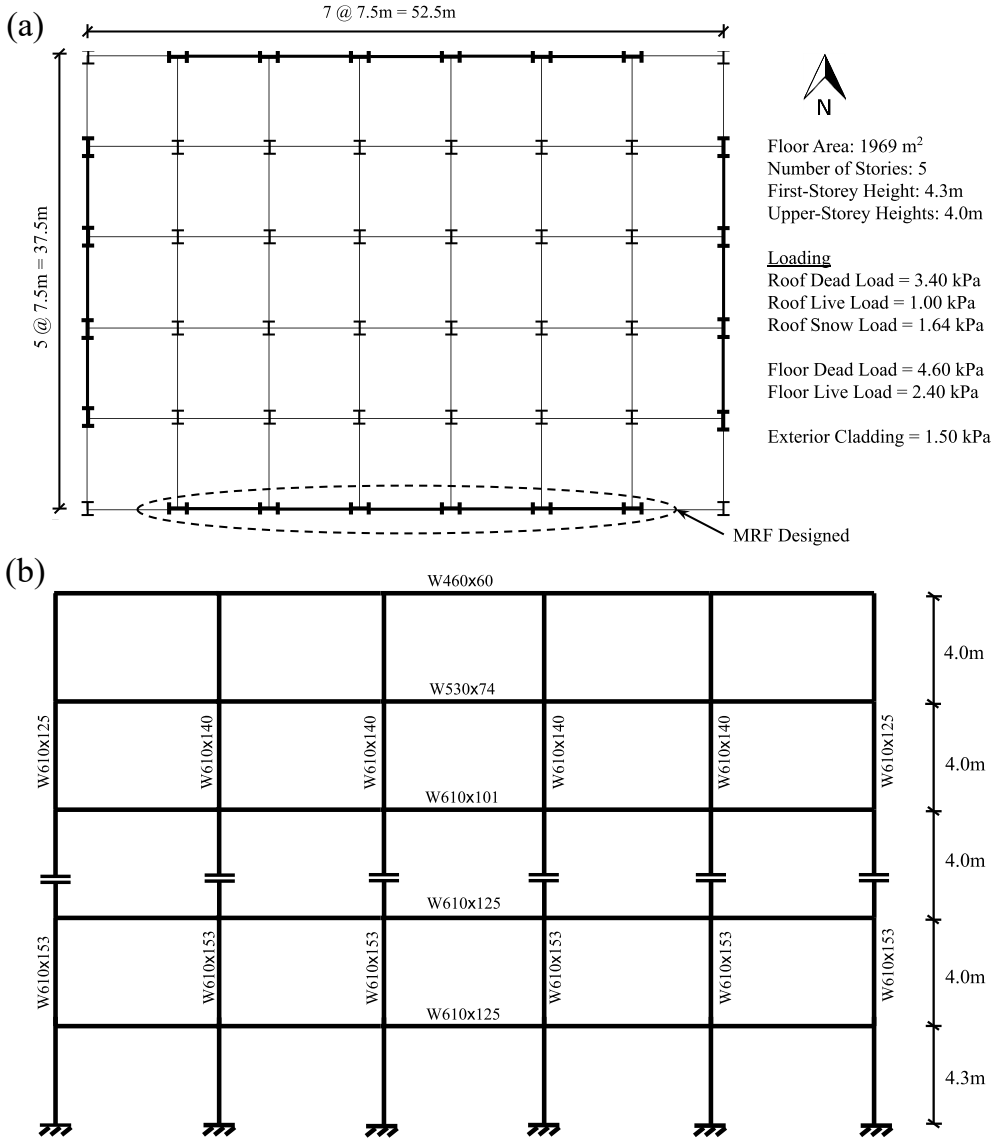

Figure 4-1. Selected five-storey office building: (a) Plan view; (b) Elevation view of the selected perimeter MRF and selected member sizes.

4.3 Member Design

The MRF was designed following CSA S16-19 using wide-flange (W-shape) sections for beams and columns conforming to ASTM A992 Gr. 50 steel with a minimum specified yield strength F_y = 345 MPa and probable yield strength R_yF_y = 385 MPa. Beam-to-column moment connections consist of reduced beam section (RBS) connections designed in accordance with the CISC Moment Connections for Seismic Applications (CISC 2014) with the maximum allowable flange cut (=50% of b_f). Identical wide-flange profiles were used throughout each storey. The columns were spliced at Storey 3, 1.2 m above the storey level, as shown in Fig. 4-1b.

The design of the MRF was an iterative process where the strength requirements and the drift limit were verified in each iteration. The beams were first designed as a flexural member under gravity plus seismic load effects, while their sections were adjusted subsequently to meet the stringent storey drift ratio limit and RBS connection requirements. Within each design iteration, the strong column-weak beam ratio (Eq. 2-1) at each beam-to-column joint, in and out-of-plane stability of the columns (Eq. 2-2) in Stories 2-5 were verified. The storey drifts were then checked against the 2.5% limit taking into account the effects of reduced stiffness due to RBS through a 10% amplification applied to the elastic drift of the structure (CISC 2014). Fig. 4-1b shows the selected member sizes for the MRF. The member design was mainly governed by the drift check, performed using a longer design period T_a = 1.79 s computed as the minimum of the analytical period from a modal analysis in SAP2000 and an upper bound limit of 2.0 s.

A W610×153 column section with a $d/b_f \approx 2.7$ and an $L_b/r_y \approx 85.0$ was selected for the interior and exterior first-storey columns. This section does not meet the current CSA S16 special provisions for the first-storey Ductile MRFs. The global slenderness ratio of the W610×153 column exceeds the limit (= 50 with κ = 0 and F_y = 345 MPa as given in Eq. 2-3). Moreover, it possesses a web

width-to-thickness ratio of 40.9, above the limit of 37 specified for columns with an axial compression load equal to or exceeding $0.15AF_y$ (see Eq. 2-4). It should be noted that the interior W610×153 column was subjected to a maximum axial compression load of just $0.15AF_y$. The exterior W610×153 column was subjected to a maximum axial compression load above $0.30AF_y$ from design. Still, it was deemed through the results obtained in Chapter 3 that the requirements of Eq. 2-4 and the axial load limit of $0.30AF_y$ is on the conservative side for exterior columns, which heavily benefit from largely fluctuating axial loads due to dynamic overturning effects. However, this selection was performed deliberately to critically evaluate the current section and global slenderness ratios prescribed by CSA S16 for first-storey columns of Ductile steel MRFs (Imanpour et al. 2016) and match the test specimen already donated to this project. However, the experimental phase of this project was eliminated due to laboratory space constraints and the project timeline.

4.4 Concentrated Plasticity-based Numerical Model and Ground Motion Accelerations

A concentrated plasticity-based model of the prototype frame was created in the OpenSees (Mckenna et al. 1997) environment. The same modelling technique described in Chapter 3 was used to develop the numerical model of the MRF in this chapter.

The NLRHA was performed on the MRF under the suite of 33 ground motion records given in Table 3-1 applied in-plane in the horizontal direction. The same scaling factors provided in Table 3-1 were used as the fundamental period of the MRF was within the scaling period range used for the MRFs of Chapter 3. The resulting drifts from the NLRHA, including storey drift ratios, are given in Table 4-1.

Table 4-1. NLRHA storey drifts

Source of Seismicity	ID	Storey 1	Storey 2	Storey 3	Storey 4	Storey 5
Crustal	C01	0.68	0.85	0.92	1.26	1.57
	C02	0.73	0.98	1.02	1.49	1.52
	C03	1.01	1.47	1.77	2.21	2.38
	C04	1.28	1.74	1.67	2.53	2.98
	C05	0.89	1.27	1.67	2.01	2.17
	C06	1.15	1.59	1.48	1.50	1.53
	C07	1.06	1.47	1.79	1.69	2.10
	C08	1.04	1.38	1.40	1.55	2.03
	C09	0.63	0.66	0.74	1.12	1.58
	C10	0.84	0.83	0.81	1.20	1.57
	C11	0.76	0.99	1.38	1.57	1.66
Deep In-slab	D01	1.15	1.51	1.81	1.78	1.78
	D02	0.99	1.17	1.34	1.88	2.36
	D03	1.16	1.05	1.30	2.00	2.78
	D04	1.20	1.36	1.34	1.53	1.96
	D05	0.91	1.18	1.19	1.65	2.68
	D06	0.96	1.42	1.67	1.54	1.96
	D07	0.99	1.17	1.60	1.79	2.62
	D08	0.86	1.12	1.30	1.74	1.89
	D09	1.14	1.27	1.40	2.45	2.86
	D10	1.25	1.79	1.57	2.21	2.41
	D11	1.07	1.25	1.17	1.51	1.94
Interface	I01	1.58	2.11	1.93	1.86	1.68
	I02	1.23	1.80	1.86	1.91	1.60
	I03	1.76	2.00	2.04	2.06	1.74
	I04	2.40	2.10	2.30	2.25	2.21
	I05	2.80	3.20	3.24	3.19	2.82
	I06	2.56	2.77	2.72	2.46	2.17
	I07	1.40	2.07	2.55	3.23	2.97
	I08	1.88	2.39	2.78	2.55	1.96
	I09	Global Frame Collapse				
	I10	1.43	2.08	2.31	2.08	1.60
	I11	1.11	1.66	1.66	1.84	1.68

Three ground motion records that created the three largest storey drift ratios in Storey 1 were selected to study the 3D response of the MRF here. The selected records belong to the interface scenario and consist of the 2007 Pisco, Peru – UNICA earthquake (I05), 2010 Maule, Chile – SSA2 (I06) earthquake, and 2011 Tohoku, Japan – YMT002 earthquake (I09). The last one yielded the largest displacement demand on the first-storey column, while the second record created the third greatest displacement in Storey 1. Fig. 4-2 shows the scaled pseudo acceleration spectra $S_a(g)$ of the records compared to the NBCC design spectra for the selected site, i.e., Vancouver Soil Type C. The period range over which the scaling was performed is also provided in the figure.

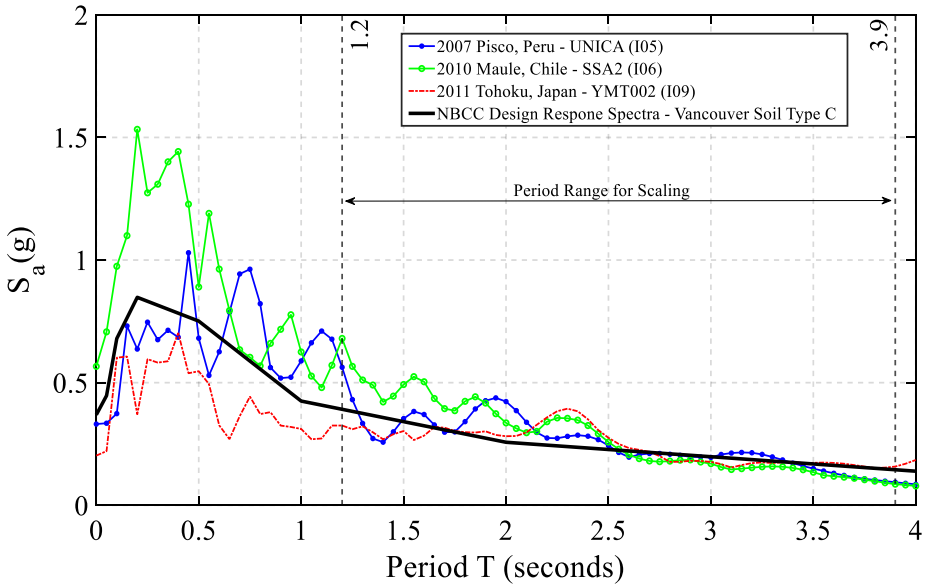

Figure 4-2. Pseudo acceleration spectra of scaled ground motion records selected to study the three-dimensional response of the MRF subassembly.

4.5 Three-Dimensional Response of Steel MRF

4.5.1 Continuum-based Finite Element Model of MRF Subassembly

A three-dimensional Continuum-based Finite Element Model (CFEM) of the MRF subassembly was developed in the ABAQUS program (Simulia 2020) for a subassembly isolated from the five-storey MRF, as shown in Fig. 4-3. The subassembly model consisted of the exterior bay plus half of the adjacent interior bay, assuming an inflection point at beam mid-span of the MRF in which

the beams, columns, and beam-to-column connections were explicitly modelled. This model was intended to study the 3D response of steel MRFs when subjected to ground motion accelerations, focusing on the seismic demands induced in wide-flange first-storey columns as affected by the nonlinear response of upper stories. Furthermore, the subassembly model can aid in further improving the understanding of the stability response of slender ($L_b/r_y > 50$) wide-flange columns in the first storey of MRFs under seismic loading and help develop enhanced seismic design requirements for such columns.

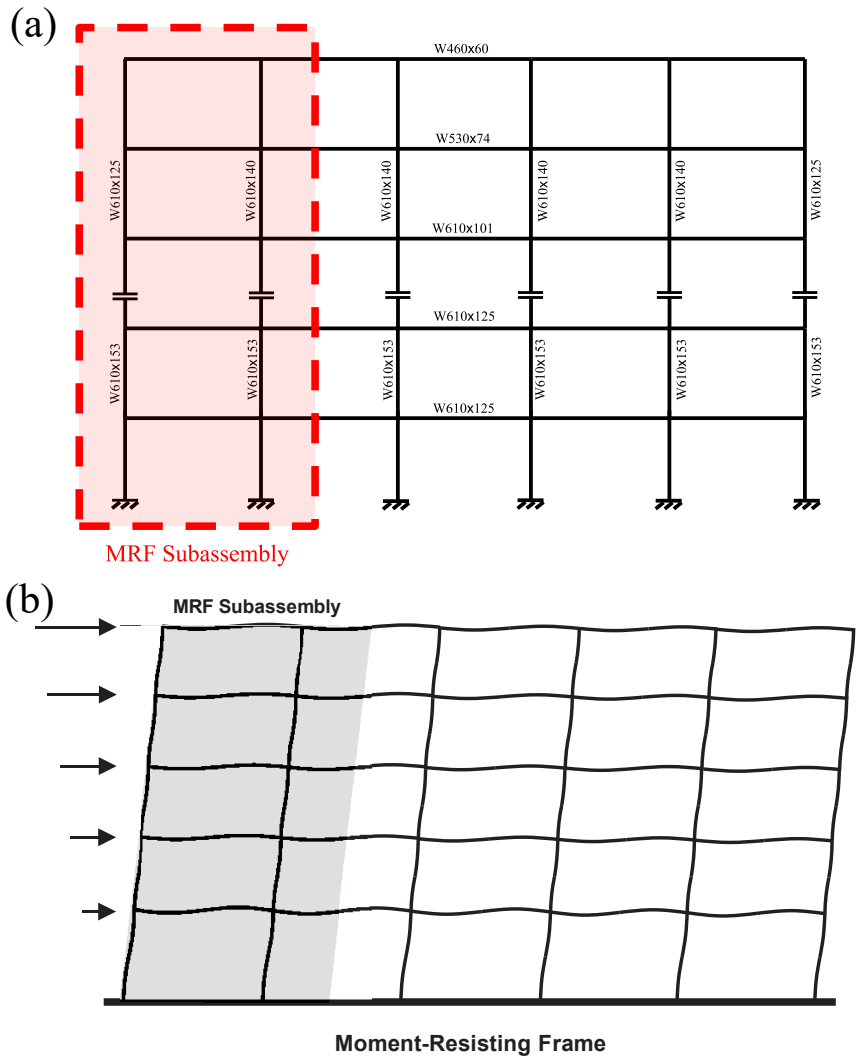

Figure 4-3. Selected MRF subassembly: (a) Undeformed MRF and member sizes; b) Deformed MRF under lateral loads.

The isometric view of the MRF subassembly is shown in Fig. 4-4a. The beams and columns were simulated using four-node doubly curved, reduced integration, hourglass controlled Shell elements (S4R) with a uniform structured mesh. The mesh size was varied across the model to optimize computation time without sacrificing accuracy. A 25 × 25 mm mesh was used for the first-storey columns, at every beam-to-column web panel zone joint and the RBS locations (see Fig. 4-4b) as yielding is expected. A coarse mesh was employed in locations where yielding or instability is not expected. An element size of 25 × 75 mm was used between the column panel zones in upper-storey columns and outside RBS locations. The RBS connection was constructed explicitly by trimming flanges and adjusting the mesh structure to accommodate the circular cut. Doubler plates in the column panel zones were simulated by increasing the element thickness on the area encompassing the adjoining beam and column webs. Continuity plates were provided in the column web at the level of the top and bottom flanges of the beams.

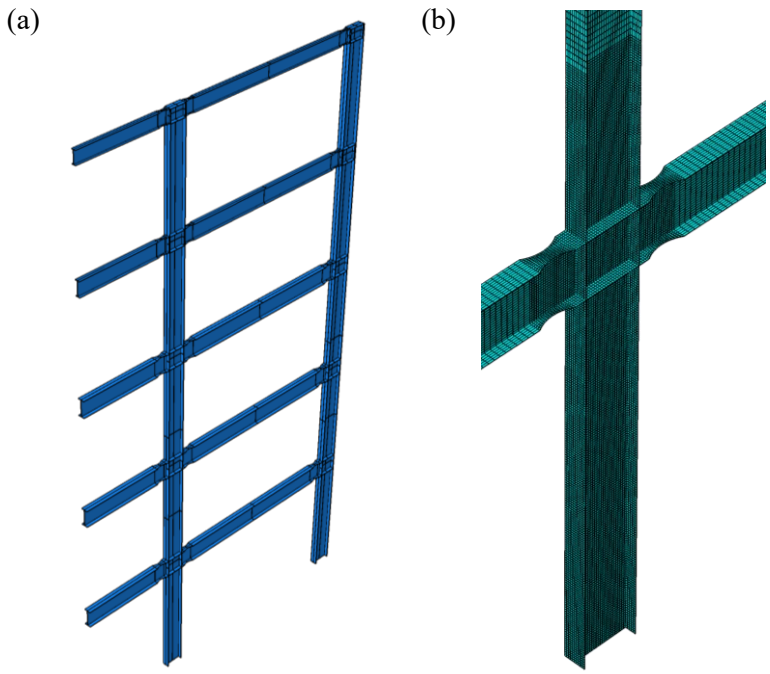

Figure 4-4. (a) MRF subassembly (elements are not shown); (b) CFEM of the beam-to-column connection.

Material nonlinearity was incorporated in the model through the Maxwell-Huber-Hencky-von Mises yield criterion with associated flow rule. The nonlinear cyclic behaviour of the steel material was reproduced using the Voce and Chaboche plasticity model with combined kinematic/cyclic hardening parameters as described in Section 3.4.1. This model features combined isotropic/kinematic hardening (de Castro e Sousa et al. 2020; Hartloper et al. 2021) with Young's modulus, E = 200 GPa, Poisson's ratio υ = 0.3, and the expected yield stress R_yF_y = 385 MPa. The steel stress-strain behaviour is represented by kinematic hardening parameters consisting of C = 3378 MPa and γ = 20, while cyclic hardening parameters are equal to $Q_\infty = 90$ MPa and b = 12 (Elkady and Lignos 2018b). The residual stress distributions for both wide-flange sections were specified based on the pattern proposed by Galambos and Ketter (1958), which is defined using a linear distribution in the flange with a maximum compressive stress of $0.3F_y$ at the tip of the flange and maximum tensile stress of $0.3A_f/(A_f + A_w)F_y$ at the middle of the flange, where, A_f and A_w are the flange and web cross-sectional areas, respectively. A uniform tensile stress distribution with an amplitude of $0.3A_f/(A_f+A_w)F_y$ is considered on the web. The Rayleigh damping method was used to reproduce classical damping in the model. The corresponding mass and stiffness proportional damping coefficients were assigned based on the structure's first and second modes of vibration obtained from a frequency analysis performed on the subassembly model, which resulted in periods of 1.84 and 0.64s, respectively. These periods agree well with those obtained from the modal analysis of the MRF using the SAP2000 model (1.79 and 0.62s).

Initial geometric out-of-straightness was used in the model to trigger local and global instability. Local initial geometric out-of-straightness were assigned to web and flanges at both ends of the columns at each storey based on the maximum anticipated manufacturing errors (ASTM 2003) with maximum amplitudes of $b_f/150$ and $d/150$ in the flange and web, respectively. For both beams and

columns, global out-of-plane out-of-straightness, which is affine to each member's global buckling mode, was created with a maximum amplitude of 1/1000 times the member's length (AISC 2016). Additional details regarding the residual stress distributions and the initial geometric imperfections are provided in Section 3.4.1. The modelling assumptions were verified by comparing the cyclic behaviour predicted using the numerical model developed here against the experimental test data reported by Elkady and Lignos (2018a) for 4000mm-long W610×217 column specimens. The calibration results are shown in Figs. 3-7.

Figure 4-5b shows the boundary conditions considered to simulate the subassembly as part of the MRF. All translational and rotational DOFs were restrained at the base of the column, except the translational DOF along the Z-axis (in the plane of the frame) to allow for horizontal movement resulting from base excitation created by the ground motion acceleration (see Fig. 4-5b). At the top end of the column at each storey at the level of the beam top flange, the translations and rotations of the column section nodes were coupled to a reference point (RP) located at the middle of the column web (Fig. 4-5b). The out-of-plane translational DOF in X-axis was restrained at this RP to represent the lateral support provided by the perpendicular beams framing into columns at the storey level. The translational DOF of the top end of both the interior and exterior columns at each storey (at RPs) were coupled in the Z-axis to simulate a rigid floor diaphragm. However, the concrete slab was not explicitly modelled here. Thus, the beneficial effects of the concrete slab in carrying flexural bending moment (Elkady and Lignos 2014b) were ignored.

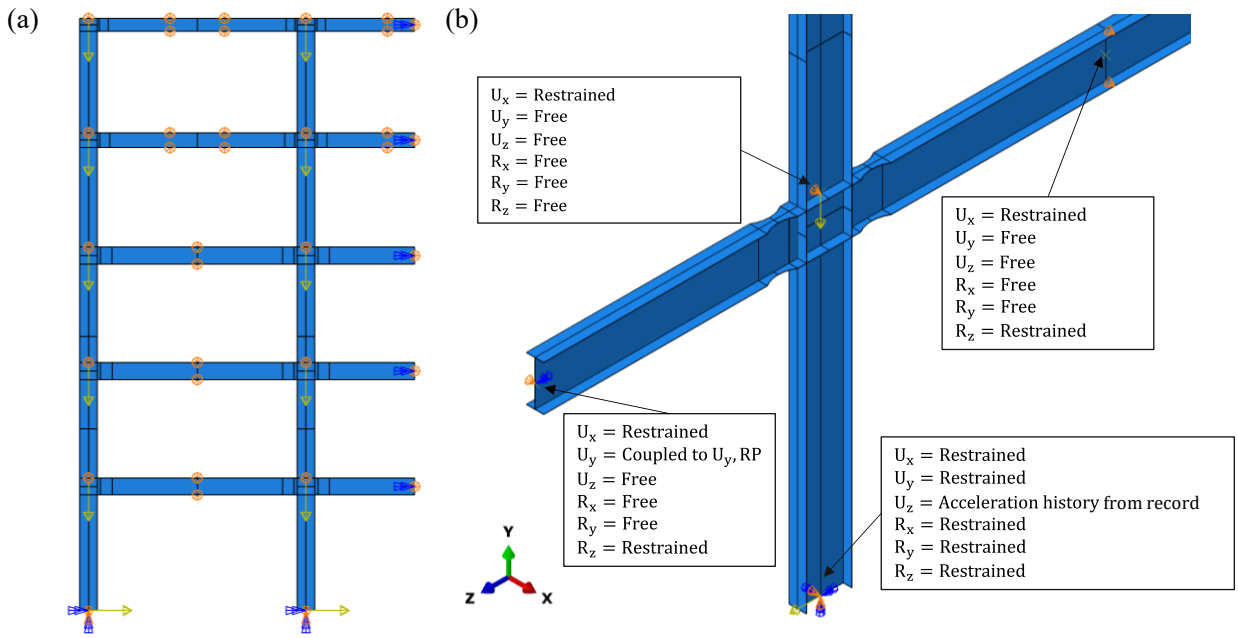

Figure 4-5. Subassembly model boundary conditions: (a) Elevation view; (b) first-storey interior column.

Supplemental out-of-plane bracing for the beams was provided at beam mid-span at both top and bottom flanges (Fig. 4-5a) following the CSA S16 lateral bracing requirement assuming $\kappa = 0$ (see Eq. 2-3). This was simulated by restraining translation in X-axis at the exterior beam mid-span and the free end of the beam of the interior bay. Bracing at the RBS locations was not provided, referring to the AISC 358 (AISC 2016) requirement stating that supplemental bracing is not required at the beam reduced section if a concrete slab is connected with shear studs spaced at or less than 300 mm. This assumption was made to create more critical out-of-plane demands on the first-storey column. The results obtained from this model may therefore be deemed to be conservative.

The axial gravity load tributary to each column at each storey was applied at the respective column RP. A leaning column, consisting of rigid beam-column wire elements, was added to account for P-Delta effects. The rotational DOFs of the leaning column were released at the two ends within each storey, thereby providing no rotational stiffness at member ends. Moreover, the translational

DOF of the leaning column was coupled to that of the MRF subassembly at each storey using a kinematic coupling constraint. The subassembly model was analyzed under the three selected ground motion records (I05, I06, and I09) applied to the base in the Z-axis. The implicit dynamic analysis method was used to perform the NLRHA in the ABAQUS program. The analyses were completed using a remote cluster provided by Compute Canada (www.computecanada.ca) to achieve a better computation time.

4.5.2 Dynamic Analysis Results

The results of the dynamic analysis of the subassembly model under all three records confirmed the plastic collapse mechanism anticipated in a steel MRF, which involves flexural yielding at the base of the column, RBS locations, and partial shear yielding at beam-to-column web panel zone. The peak storey drift ratio profile was shown in Fig. 4-6 for the records analyzed. Storey drift ratios were computed by subtracting the lateral displacement recorded at the beam-to-column centreline at the bottom of each storey from that recorded at the beam-to-column centreline at the top of the storey.

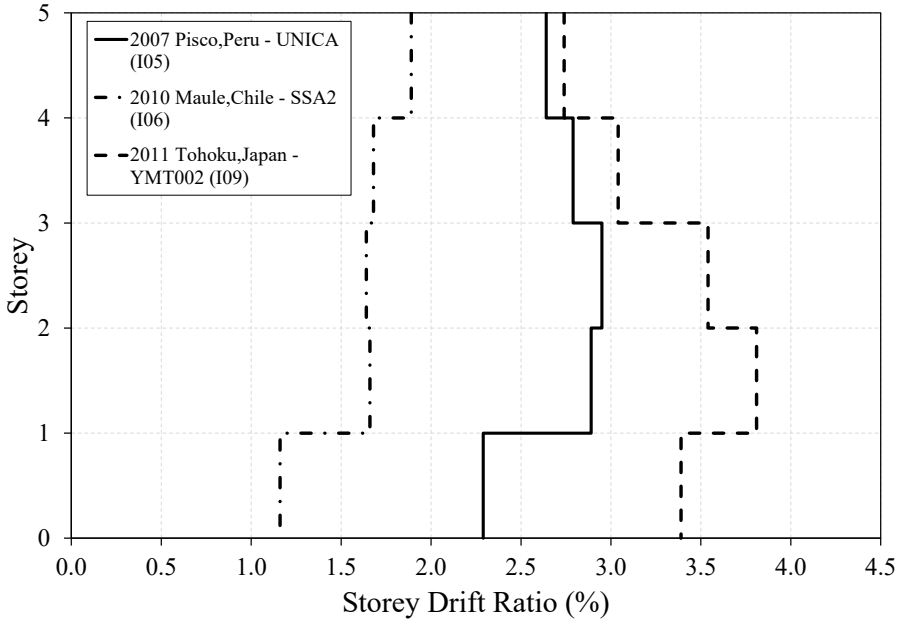

Figure 4-6. Profile of storey drifts ratios from the subassembly model.

Referring to Fig. 4-6, the subassembly model experienced the largest storey drifts under the 2011 Tohoku, Japan – YMT002 (I09) earthquake, followed by the 2007 Pisco, Peru – UNICA (I05) earthquake. The drift response under the 2010 Maule, Chile – SSA2 earthquake (I06) was the smallest among the three records considered here. The key analysis results, including nonlinear mechanism, yielding propagation, local instabilities, beam behaviour with the focus on the RBS response, and column demands were presented in the subsequent subsections under the 2011 Tohoku, Japan – YMT002 (I09) earthquake, which yielded the most critical drift response on the selected W610×153 columns.

4.5.2.1 Subassembly Overall Response

The MRF subassembly deformed-shape and von-Mises stress distribution at maximum storey drift ratio recorded in Storey 1 and 2, 3.4% and 3.8%, respectively, at t = 156s under the 2011 Tohoku, Japan – YMT002 (I09) earthquake is shown in Fig. 4-7. At this point of the NLRHA, the exterior column is in tension. A magnified view of Stories 1 and 2 shown in Fig. 4-7 confirms plastic hinging at the base of both columns along with significant yielding in RBS regions of the beams and shear yielding in the column panel zones. Flexural plastic hinges first formed at the RBS reduced zones of the first two stories and base of the first story columns at 36s and then propagated to the upper story beams. After beam plastic hinging, as drift increased, large out-of-plane displacements occurred at the RBS reduced zone, particularly at the bottom two stories leading to twisting at the first-storey columns (Chi and Uang 2002).

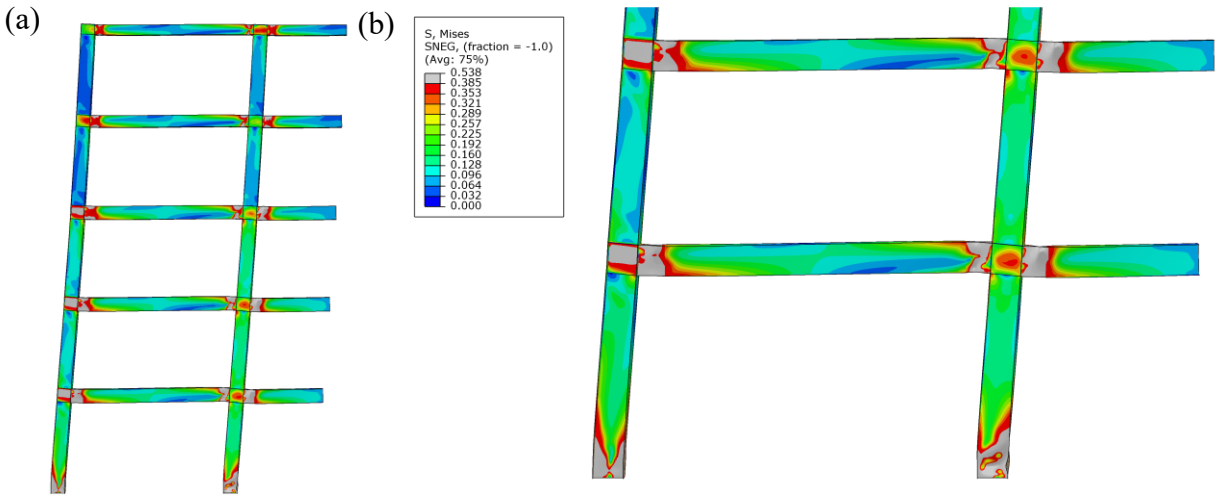

Figure 4-7. Deformed-shape and von-Mises stress distribution at t = 156s under the 2011 Tohoku, Japan - YMT002 earthquake: (a) elevation view; (b) Storey 1 and 2 (gray area represents yielding).

4.5.2.2 Beam Response

Strong-axis bending response and out-of-plane displacement at the RBS location of the W610×125 beams adjoining the interior column are shown in Figs. 4-8a and 4-8b. The out-of-plane displacement at each RBS was computed by taking an average of the amplitudes recorded at the top and bottom of the web. The left RBS (on the negative Z-axis side of the column) and right RBS (on the positive Z-axis side of the column) in Fig. 4-8a and their displacement signage (along X-axis) in Fig. 4-8b are denoted based on the coordinate system shown in the figure.

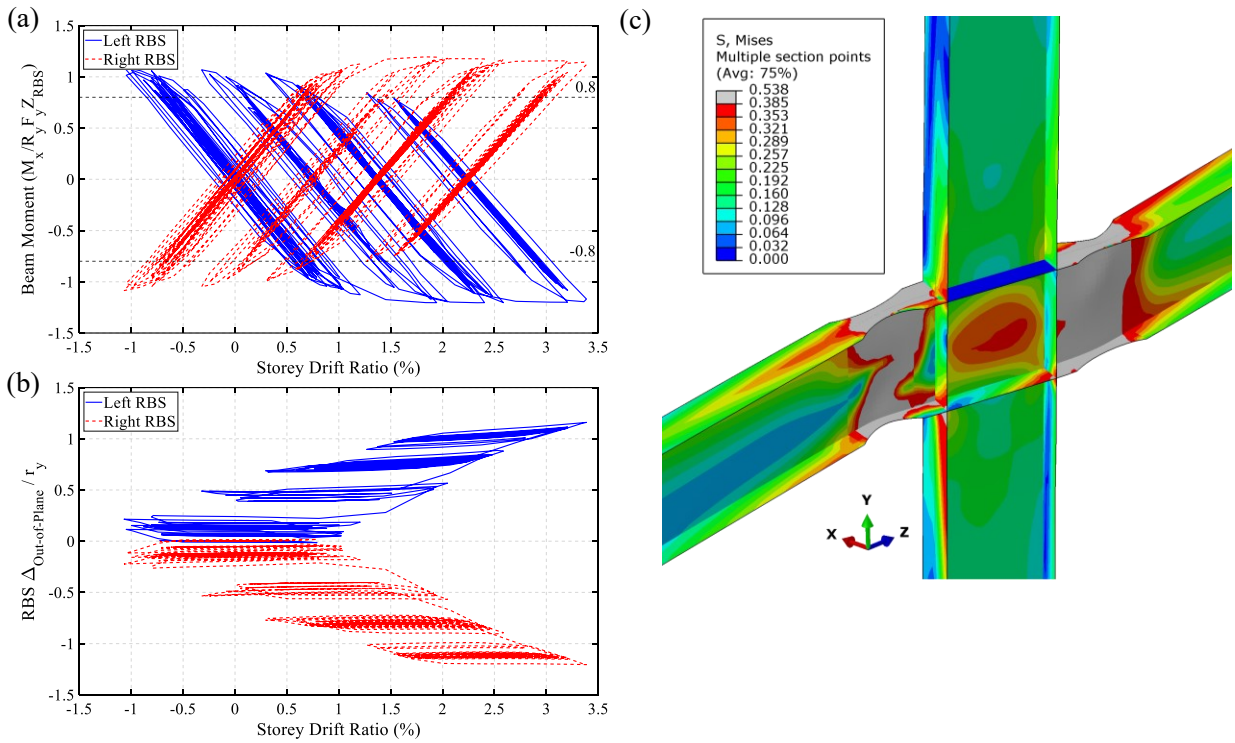

Figure 4-8. Response of W610×125 beams adjoining the interior first-storey column under the 2011 Tohoku, Japan – YMT002 earthquake: (a) Moment – storey drift ratio; (b) Out-of-plane displacement at RBS; (c) Connection deformed-shape at t = 156s, storey drift ratio 3.4% (gray area represents yielding).

As shown in Fig. 4-8a, beam moment reached a maximum value of $1.20R_yF_yZ_{RBS}$ at 1.5% drift ratio and then reduced to $1.09R_yF_yZ_{RBS}$ at 3.4% drift ratio at the right beam due to limited local buckling and out-of-plane movement in the RBS. A similar moment response was recorded in other stories with the moment capacity at the RBS always above $0.80R_yF_yZ_{RBS}$, indicating a stable beam-to-column moment connection response. In Fig. 4-8b, an increasing trend was observed for the out-of-plane displacement at RBS locations, while the rate of this increase tended to reduce at large drift ratios. The maximum out-of-plane displacement recorded was $1.3r_y$ for both beams connected to the column on each side but moving in opposite directions (left RBS moving along positive X-axis and right RBS moving along negative X-axis) as shown in Fig. 4-8c. This response caused twisting at the first-storey column and will be discussed below. Furthermore, RBS displacements were slightly different (approximately $0.20r_y$) between the top and bottom of their respective cross-sections, generating twists in the beam due to non-uniform yielding of the top and

bottom flanges in the presence of initial out-of-plane imperfections. The out-of-plane RBS response confirms the tendency of steel beams to buckle in the inelastic range with pronounced deformations in plastic hinge regions (Chi and Uang 2002). It should be noted that the cross-section twist and RBS out-of-plane displacement observed for the interior column was mainly produced because of the lack of supplemental bracing at the RBS locations and could have significantly been reduced if lateral support had been provided.

The beam moment and out-of-plane displacement at the RBS for the exterior column were also recorded and are shown in Fig. 4-9. The beam moment reaches $1.23R_yF_yZ_{RBS}$ with no sign of strength deterioration. The RBS out-of-plane displacement reaches a maximum of $0.8r_y$ at 3.4% drift, which is much less pronounced in magnitude than the interior column.

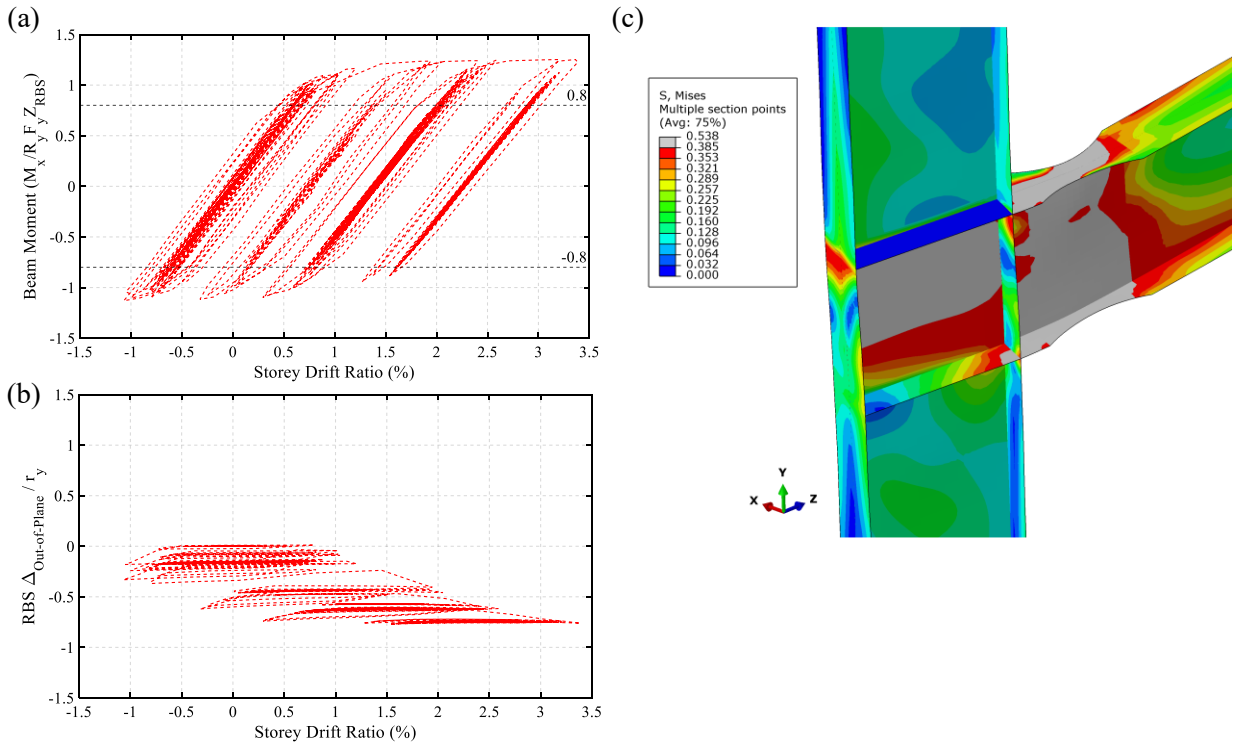

Figure 4-9. Response of W610×125 beams adjoining the exterior first-storey column under the 2011 Tohoku, Japan – YMT002 earthquake: (a) Moment – storey drift ratio; (b) Out-of-plane displacement at RBS; (c) Connection deformed-shape at t = 156s, storey drift ratio 3.4% (gray area represents yielding).

4.5.2.3 Interior Column Response

The moment-chord rotation response of the base and top end of the interior first-storey W610×153 column of the MRF subassembly is shown in Figs. 4-10a and 4-10b. This column has web and flange slenderness ratios of 40.9 and 4.6, respectively, and a member slenderness ratio equal to L_b/r_y = 85. As shown in Fig. 4-10a, the column experienced moderate strength degradation at its base, with the moment capacity reaching $1.05R_yM_{px}$ at 3.4% chord rotation from a maximum value of $1.13R_yM_{px}$ measured at 1.5% chord rotation. The loss of strength occurred mainly due to web and flange local buckling initiated at around 1.5% chord rotation and was exacerbated at higher drifts. Local buckling was accompanied by moderate axial shortening in the member under a constant axial load equal to $0.15AF_y$, which reached a maximum of $0.27\%L$ as shown in Fig. 4-10c. It is significant to note that local buckling in W610×153 was initiated at a lower chord rotation than that observed in W610×195 and W610×217 columns, which had a similar axial load, in Section 3.4.2 under the same ground motion record, which can be attributed to more slender web width-to-thickness ratio of W610×153 section compared to others (40.9 vs. 34.6 and 37.2) (Ozkula et al. 2021). The top moment is shown in Fig. 4-10b, which was recorded right below the column panel zone and never exceeded 0.52RyMpx, indicating no yielding at the column top end and an inflection point above the column mid-height. In Fig. 4-10c, the minimal stress recorded at the top continuity plate is attributed to the kinematic coupling constraint assigned to the column reference point to uniformly distribute the gravity loads throughout the column cross-section at the floor level. This assumption is not expected to affect the response of the columns and beams in the subassembly model.

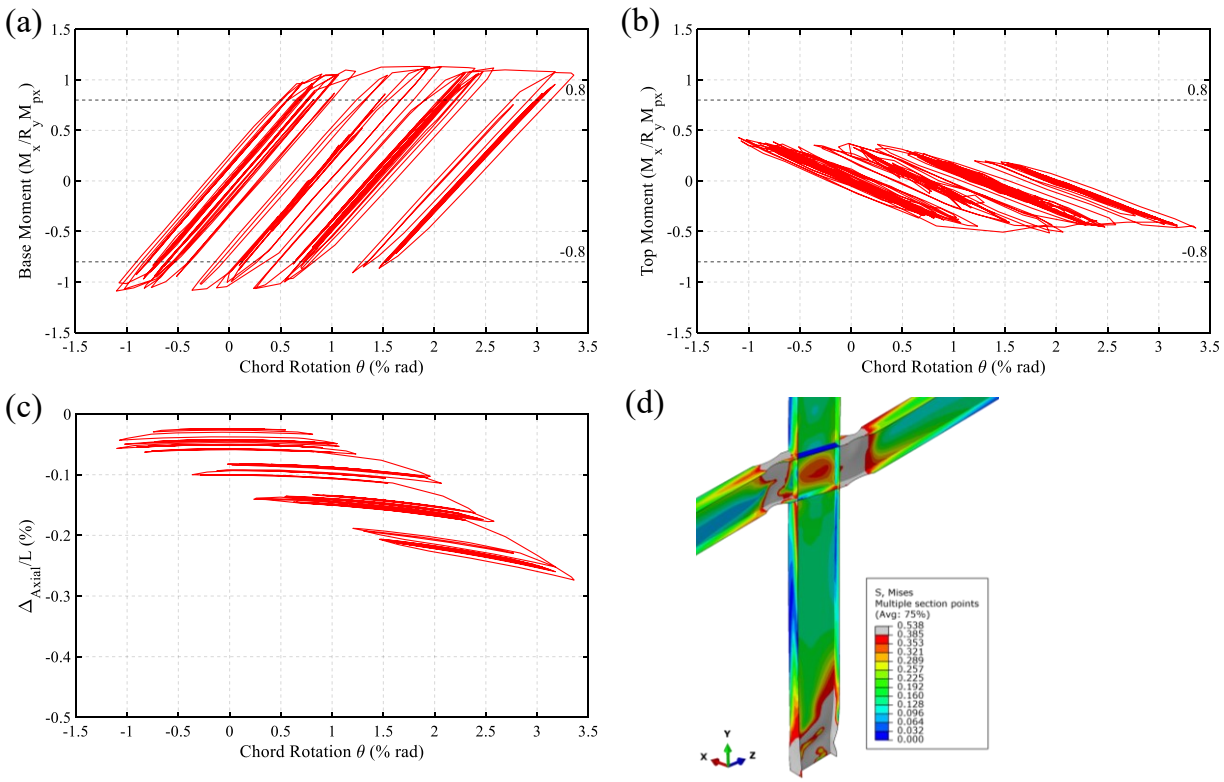

Figure 4-10. In-plane response of the interior first-storey W610×153 column under the 2011 Tohoku, Japan – YMT002 earthquake: (a) Moment – chord rotation response at the base; (b) Moment – chord rotation response at the top end; (c) Axial shortening – chord rotation response; (d) Deformed-shape and von-Mises stress distribution at t = 156 s, chord rotation 3.4% (gray area represents yielding).

Similar to the first-storey column top end, no significant yielding was observed in the upper storey columns. The moment at the bottom and top ends of these columns remained well below $1.0R_yM_{px}$. Figure 4-11 shows the out-of-plane response of the first-storey interior column, including out-of-plane moment demand, normalized out-of-plane displacement $\Delta_{Out\text{-}of\text{-}Plane}/L$ and normalized cross-section twist $\gamma_{Cross\text{-}Section}/L$. The out-of-plane deformation of the RBS plus the deformation of the base plastic hinge due to local buckling near the base (Elkady and Lignos 2018b) caused the out-of-plane moment at the top end. The moment demand reached a maximum of $0.40R_yM_{py}$. The out-of-plane displacement and cross-section twist at quarter points, $0.25L$, $0.50L$, $0.75L$, with respect to the column clear length measured from the fixed base, is shown in Figs. 4-11b and 4-11c. To eliminate

the effects of cross-section twist, the out-of-plane displacements were calculated by taking the average of the out-of-plane displacements at two extremes of the column web.

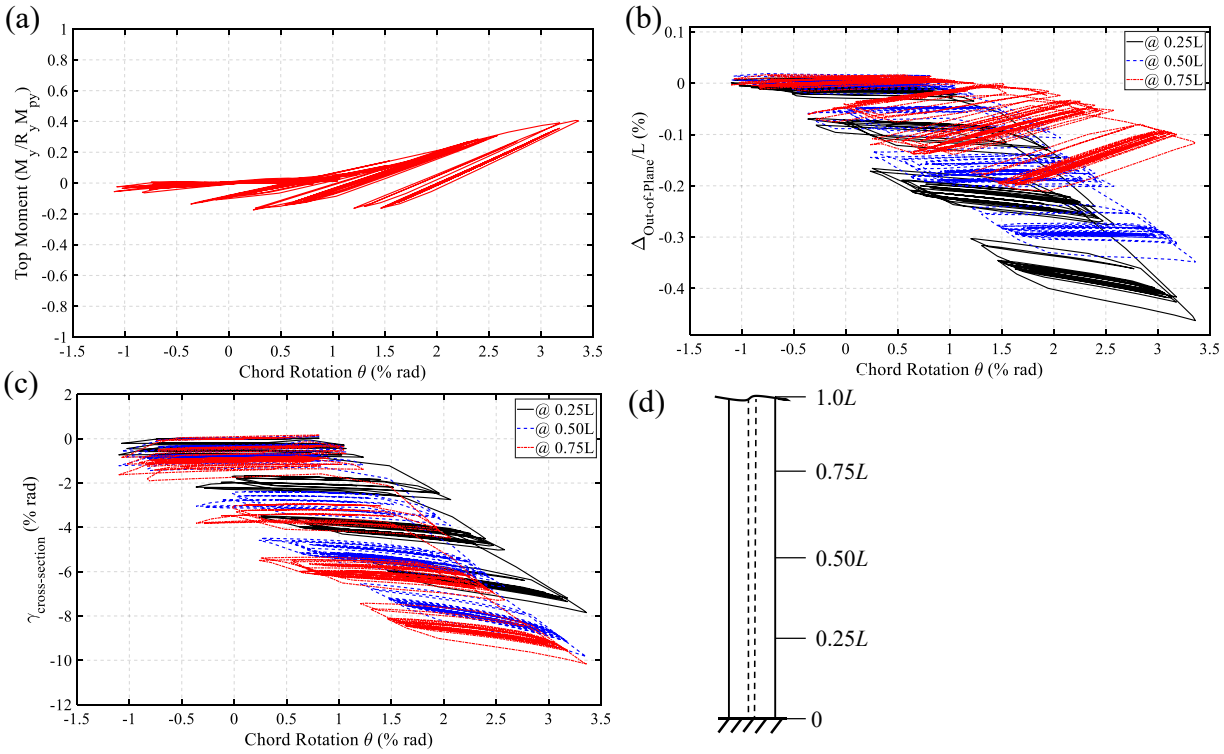

Figure 4-11. Out-of-plane response of the interior first-storey W610×153 column under the 2011 Tohoku, Japan – YMT002 earthquake: (a) Moment – chord rotation response at the top; (b) Out-of-plane displacement; (c) cross-section twist; (d) stations along column length.

The out-of-plane displacement as shown in Fig. 4-11b was more pronounced near the base of the column, i.e., 0.25*L*, where local instability took place, reaching a maximum value of 0.46%*L* at 0.25*L*, while lower amplitudes of 0.35%*L* and 0.21%*L* were recorded at 0.50*L* and 0.75*L*, respectively. A reversed trend was observed for the cross-section twist increasing towards the member's top-end, where the twist is unrestrained. The cross-section twist at 0.75*L* was recorded as 0.102 rad. (6.0 degrees) at 3.4% chord rotation. However, a lower twist was observed at 0.25*L* and 0.50*L*, 0.078 and 0.098 rad., respectively, because of the higher fixity provided by the column base compared to the flexible top. The large twist angle (> 0.10 rad.) observed here suggests that slender sections such as W610×153 may not perform well due to their susceptibility to out-of-plane

instability. This response was observed in past experimental studies of fully restrained beam-to-column connections with deep columns (Chi and Uang 2002).

4.5.2.4 Exterior Column Response

The exterior first-storey W610×153 column under the lateral displacement generated by the base excitation experienced large axial compression and tension loads due to uplift. The moment–chord rotation responses at the base and top end of this column are given in Fig. 4-12a and 4-12b. Overall the exterior column exhibited almost no strength and stiffness degradation and very limited base local buckling (Fig. 4-12d), attributed to the delay in web and flange local buckling in the exterior column.

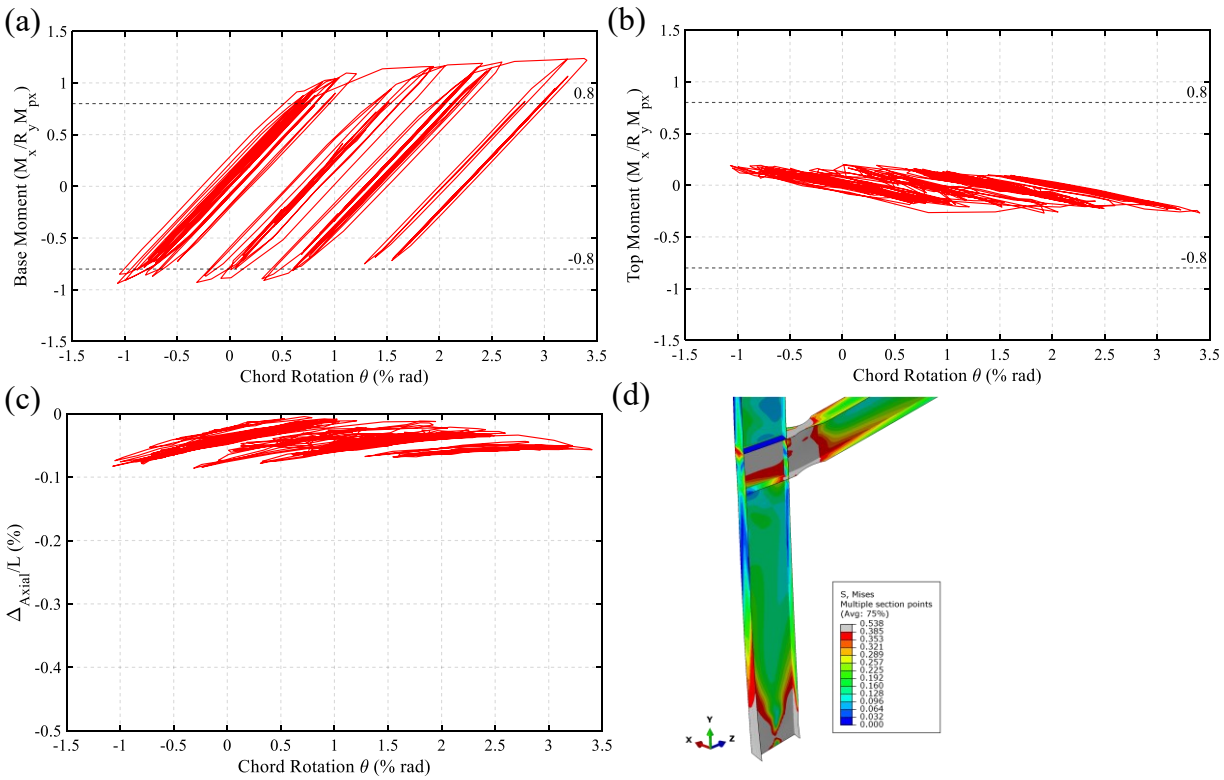

Figure 4-12. In-plane response of the exterior first-storey W610×153 column under the 2011 Tohoku, Japan – YMT002 earthquake: (a) Moment– chord rotation response at the base; (b) Moment – chord rotation response at the top end; (c) Axial shortening – chord rotation response; (d) Deformed-shape and von-Mises stress distribution at t = 156s, chord rotation 3.4% (gray area represents yielding).

The maximum moment observed at the base and top end of the column were $1.21R_yM_{px}$ and $0.30R_yM_{px}$, respectively. As shown in Fig. 4-12c, very limited axial shortening with a maximum amplitude of $0.09\%L$ was observed as the column was subjected to axial loads fluctuating between $0.06AF_y$ in tension and $0.32AF_y$ in compression. The results obtained from the NLRHA of the MRF subassembly suggest that the $0.30AF_y$ limit in CSA S16 may be conservative for such exterior columns because of strength deterioration, local buckling, and axial shortening amplitudes are much lower than those observed for the interior column under the most severe ground motion acceleration.

The out-of-plane moment demand measured at the top end of the column is plotted in Fig. 4-13a with respect to the chord rotation. As shown, a lower weak-axis moment with the peak value of $0.16R_yM_{py}$ at 3.4% chord rotation was induced in the column compared to that observed in the interior column counterpart, which may stem from having only one beam connected to the exterior column.

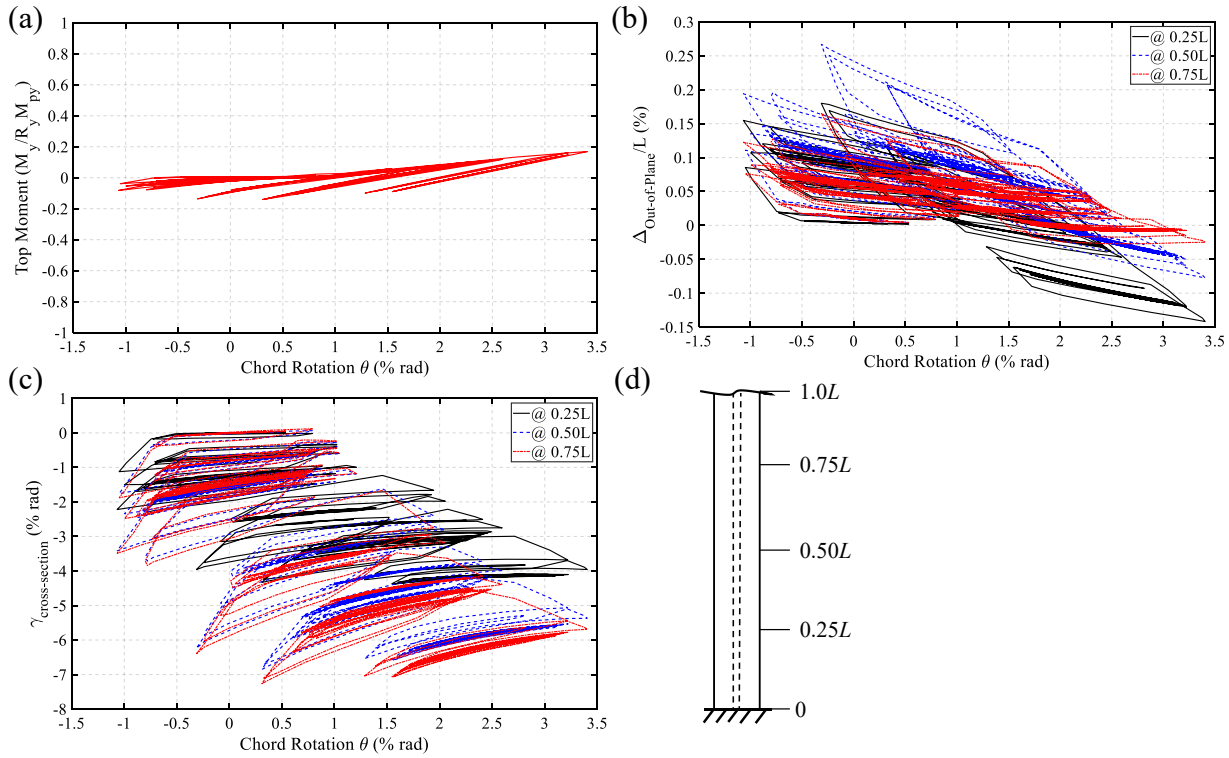

Figure 4-13. Out-of-plane response of the exterior first-storey W610×153 column under the 2011 Tohoku, Japan – YMT002 earthquake: (a) Moment – chord rotation response at the top; (b) Out-of-plane displacement; (d) stations along column length.

The exterior first-story column's out-of-plane displacement and cross-section twist are given at quarter points, 0.25*L*, 0.50*L*, 0.75*L* of the column with respect to the column clear length measured from the fixed base in Figs. 4-13b and 4.13c. The out-of-plane displacement of the column at 0.25*L*, 0.50*L*, and 0.75*L* from the base reached 0.18%*L*, 0.27%*L*, and 0.16%*L*, respectively, near the beginning of the ground motion at low drifts. As drift demand increased, the out-of-plane displacements were highest near the base plastic hinge at 0.25*L* from the base with a value of 0.14%*L* at 3.4% chord rotation, similar to the interior column but much lower in displacement magnitude. The peak cross-section twist recorded for the exterior column under the ground motion was 0.073 rad. at 0.75*L*, which also agrees with the response observed for the interior column.

The seismic demands induced in the exterior W610×153 column, including deformation and force demands, were always less critical than those measured for the interior column of the MRF

subassembly. This was attributed to the fact that the exterior column only had one moment connection inducing in-plane and out-of-plane demands on the member, plus the exterior column enjoyed the benefit of dynamic overturning effects leading to highly fluctuating axial load that reduces compression throughout the ground motion. Similar conclusions can be made based on the results obtained from the other two ground motions records (I05 and I06).

The results of the NLRHA performed on the MRF subassembly were also used to track the weak-axis moment distribution for both interior and exterior first-storey columns and compute a moment distribution factor κ for out-of-plane bending. κ is defined as the ratio of the smaller to the larger factored column moment demand at opposite ends of the member's unbraced length, which is positive when the member is in contraflexure (positive for double curvature and negative for single curvature). The average $\bar{\kappa}$ of -0.25 and -0.11 were calculated for the interior and exterior columns, respectively, based on the three ground motions using Eq. 3-2 from Section 3.3.4. Furthermore, it was determined that, on average, the column could be in single curvature over 50% the duration of the ground motion.

4.5.3 Effect of Supplemental Out-of-Plane Bracing at RBS Locations

The effect of adding supplemental out-of-plane bracing at the beam RBS locations on the seismic performance of the MRF and the interior first-storey column was examined using the NLRHA under the 2011 Tohoku, Japan – YMT002 earthquake. Supplemental out-of-plane bracing was placed at the top and bottom flanges of the beams outside the protected zone with a distance equal to half a beam depth from the end of the flange cut. As shown in Table 4-2, the extent of normalized local buckling deformations in the flange and web at the base plastic hinge was increased

(approximately 50%) when lateral support was provided in the RBS locations, mainly because of additional restraint created at the top end of the first-storey column.

Table 4-2. Normalized local buckling deformations at the base plastic hinge.

Model	Interior Column	
	Δ_{web}/h	$\Delta_{flange}/(0.5b_f)$
No Supplemental Out-of-plane at RBS	0.04	0.16
Supplemental Out-of-plane Bracing at RBS	0.07	0.26

The evaluation of the presence of the lateral support at the RBS location showed that boundary conditions play an important role in the seismic response of the MRF column (Elkady and Lignos 2018a). Less severe local buckling associated with a more flexible top boundary condition may be attributed to local buckling straightening (Cravero et al. 2020) occurring in the presence of higher cross-section twists and out-of-plane displacements along the length of the member and above the base plastic hinge. However, it is expected that due to the presence of the concrete slab, the boundary condition at the top end of MRF columns would be in between the two scenarios examined here. This aspect should further be investigated in future related studies.

4.6 Evaluation of Column Stability Parameters

The seismic stability response of steel wide-flange columns was studied using the CFEM under the in-plane demands and out-of-plane moments obtained from the MRF subassembly. An ensemble of 26 Class 1 wide-flange columns representing interior MRF columns was selected by varying the global slenderness ratio $42.2 \leq L_b/r_y \leq 127.3$ section aspect ratio $0.96 \leq d/b_f \leq 2.72$, flange width-to-thickness ratio $6.56 \leq b_f/2t_f \leq 7.68$, and web width-to-thickness ratio $17.0 \leq h/t_w \leq 48.1$. The columns were subjected to constant axial load, in-plane and out-of-plane demands representing gravity and seismic loads in a steel MRF. The selected parametric study matrix and the loading protocol were intended to create the most critical loading conditions on typical MRF first-storey columns in order to create a column stability database that is independent of MRF

design, geometry and loading. The results were used to evaluate the stability response of wide-flange steel columns.

4.6.1 Component-based Finite Element Model

A computationally efficient CFEM of an isolated column was developed using the modelling technique described in Section 3.4.1. Fig. 4-14 shows the finite element model and the boundary conditions assigned to the member. The CFEM consisted of a wide-flange column made of shell elements (S4R) and a wire element wide-flange beam extending between the column and beam mid-span attached to the column top end at the beam centreline. The beam was intended to simulate the in-plane flexibility of the column at the beam-to-column joint while representing flexural strength provided by storey beams to the columns at each joint. Only one beam was connected to the interior column to account for the fact that the moment produced by two adjoining beams at the beam-to-column joint will be distributed between the first and second storey columns. Note that the application of two beams in Section 3.4.1 is deemed conservative considering the moment produced at the column top end. The rotational DOF about Z-axis (out-of-plane) was released at the top end of the column to allow for the application of out-of-plane bending moment based on the loading protocol described later. The beam lateral out-of-plane displacement was restrained in the X-axis (Fig. 4-14b) because the out-of-plane bending moment was directly imposed on the column. Twist (rotational DOF about Y-axis) was retrained at the top end of the column to represent torsional and warping stiffness offered by upper-story columns not simulated here. The probable yield strength of steel $R_y F_y$ of 385MPa was used to define the material models for the column and beam.

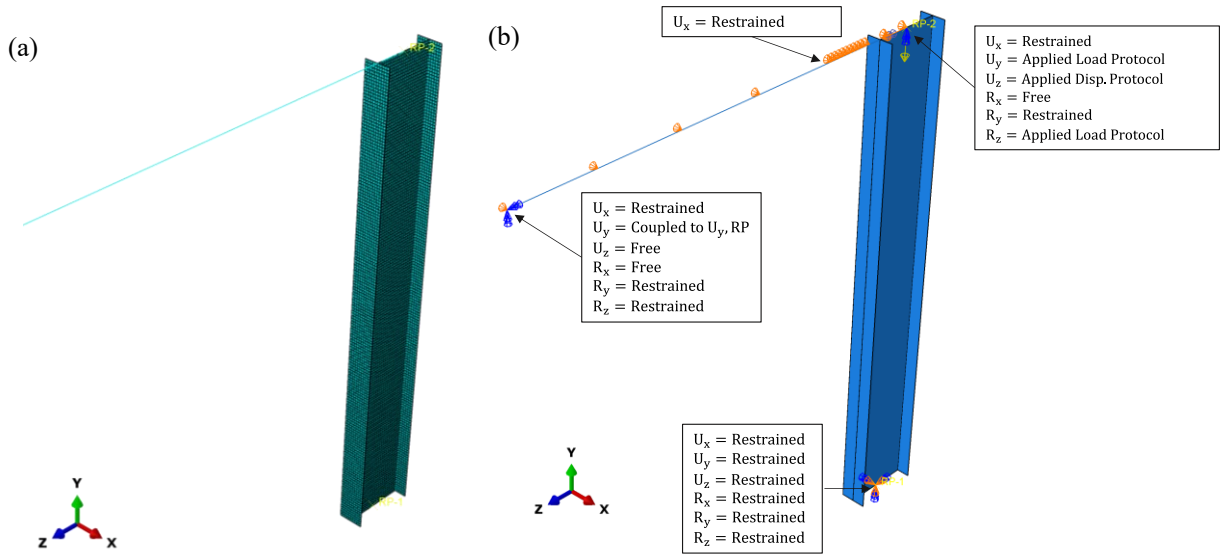

Figure 4-14. Isolated interior first-storey column: (a) Finite element model; (b) boundary conditions.

The modelling technique employed to construct the component-based CFEM of the isolated column was verified by comparing its moment and axial shortening response against those obtained from the MRF subassembly model under the 2011 Tohoku, Japan – YMT002 earthquake. The lateral displacement, axial load, and out-of-plane bending history as obtained from the dynamic analysis of the MRF subassembly were applied at the top end of the isolated column model using a static analysis method (static general). Figs. 4-15a and 4-15b compare the moment responses at the base and top end of the column, respectively, predicted by the component-based CFEM and those obtained from the NLRHA of the MRF subassembly model. The top moment in the subassembly column was calculated by projecting the moment measured below the beam-to-column panel zone to the beam-to-column joint centreline.

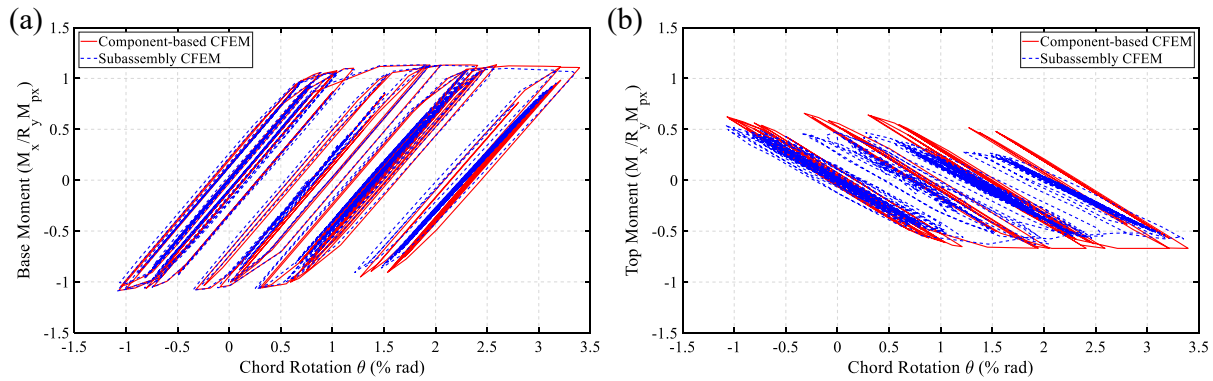

Figure 4-15. Response of W610×153 column, component-based model versus subassembly model under the 2011 Tohoku, Japan – YMT002 earthquake: (a) base in-plane moment; (b) top in-plane moment.

Referring to Figs. 4-15a and 4-15b, the moments from both component-based and subassembly models agreed well. The pronounced reduction of the top moment predicted by the subassembly model may be attributed to the twisting of the column top end, which was not allowed in the component-based model. The column deformed shapes at t = 156s, corresponding to a chord rotation of 3.4%, from the component-based and subassembly models are shown in Fig. 4-16a and 4-16b, respectively. As shown, a good match was obtained between two models when predicting yielding regions, local bucking locations and severity, and distribution of stress. The comparison of column axial shortening between two models shown in Fig. 4-16c further confirmed the capability of the computationally efficient component-based model to predict the cyclic response of MRF columns with base plastic hinging.

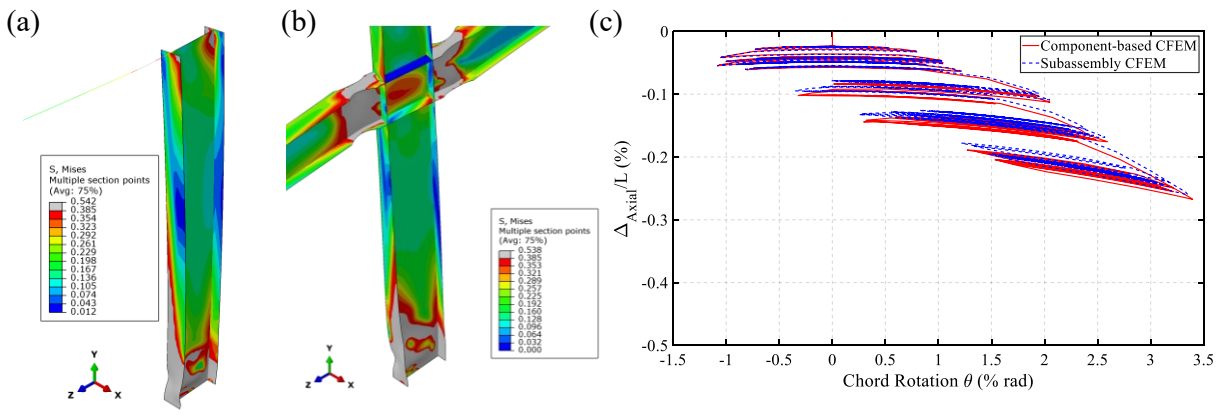

Figure 4-16. Response of W610×153 column, component-based model versus subassembly model under the 2011 Tohoku, Japan – YMT002 earthquake: (a) Column deformed-shape and von-Mises stress distribution from the component-based model at t = 156s, Chord rotation = 3.4% rad. (gray area represents yielding region); (b) Column deformed-shape and von-Mises stress distribution from the subassembly model at t = 156s, Chord rotation = 3.4% rad. (gray area represents yielding region); (c) Axial shortening.

4.6.2 Loading Protocols

The cyclic loading sequence proposed by Section K of the AISC 341-16 (Fig. 4-17a) was used here to simulate the in-plane cyclic displacement anticipated under seismic loads. This protocol was preferred over the displacement history obtained from a ground motion record as it is expected that it leads to more conservative in-plane demands on the column, thus providing an envelope of anticipated seismic demands in the west coast of Canada where deep and long duration subduction earthquakes are expected (Table 4-1) (Suzuki and Lignos 2021). The maximum storey drift angle applied to the column was 4%, which can conservatively represent a seismic hazard level with a 2% probability of exceedance in 50 years, i.e., design-level hazard according to 2015 NBCC. It is important to note that the selected symmetric loading protocol generates in-plane lateral displacements consecutively reaching maximum values in opposite directions, whereas an actual ground motion tends to create an asymmetric and sometimes ratcheting behaviour, which was observed in the MRFs investigated dynamically here. As part of the in-plane demand, the column was subjected to a constant gravity-induced axial compression equal to $0.15AF_y$, representing an

axial load level seen in typical Type D MRFs such as those in this study. This compression load corresponds to 14% of the probable axial capacity (AR_yF_y) assumed in the model.

To reproduce the weak-axis bending demand observed at the top end of the first storey MRF column (Fig. 4-11a) under seismic ground motions, the envelope of the out-of-plane moment from the three NLRHA records using the MRF subassembly model was computed. The three histories showed almost linearly increasing demand within the storey drift angles the subassembly experienced, with a maximum value of $0.40R_yM_{py}$ at 3.4% storey drift ratio. The out-of-plane moment demand for the storey drift angles outside of the range recorded in the NLRHA was extrapolated to develop the weak-axis moment protocol. The final weak-axis bending protocol is shown in Fig. 4-17b.

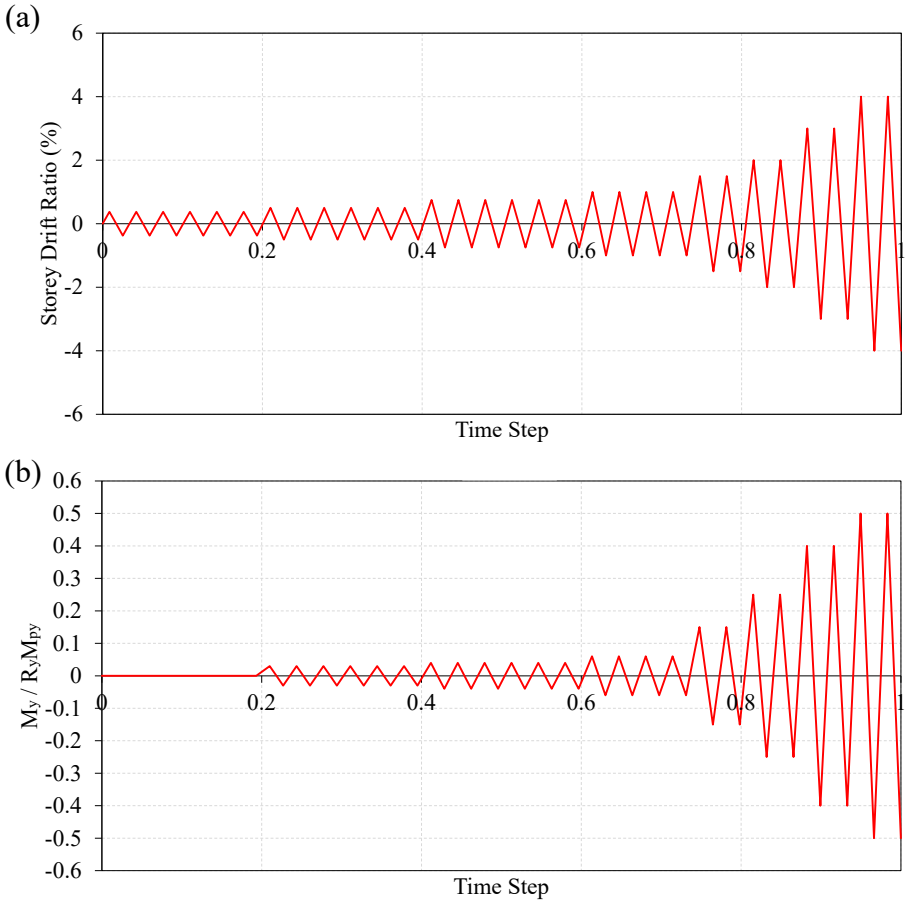

Figure 4-17. Component-based CFEM loading protocol: (a) In-plane displacement history; (b) Weak-axis bending moment history.

4.6.3 Virtual Test Matrix

A total of 26 Class 1 wide-flange columns representing first storey members of steel MRFs were selected for the parameter study to evaluate column stability response. The selected sections, plus their geometric properties and cross-sectional capacities, are given in Table 4-3. In this table and the entire parameter analysis, the unbraced length (L_b) is the same as the column length (L) and represents the distance from the fixed base to the beam-to-column centreline. The virtual test matrix was selected such that while creating a wide range of column stability influential parameters, including $42.2 \leq L_b/r_y \leq 127.3$, $17.0 \leq h/t_w \leq 48.1$, $6.56 \leq b_f/2t_f \leq 7.68$ and $0.96 \leq d/b_f \leq 2.72$, they represent practical and available members used in the North American steel construction practice, with the emphasis on deep ($d/b_f \geq 1.74$) sections, which favor a more economical MRF design. The deep sections include W530×150, W530×182, W610×125, W610×153, W610×174, and W610×217 profiles (labelled as CD in Table 4-3). In addition to deep sections, a square ($d/b_f \approx 1.0$) W360×237 profile (labelled as CS in Table 4-3) was chosen as a baseline column design and is expected to sustain large in-plane bending (Newell and Uang 2008) and potentially weak-axis bending demands without significant stability issues. Four unbraced heights L_b including 3300, 4300, 5300, and 6300 mm were considered for deep members, while the stocky W360×237 column had two heights, 4300 and 6300 mm. The selected heights cover the potential first-storey column in mid-rise steel MRF buildings for typical office, hotel, or residential occupation scenarios. The storey beam connected to the top end of the column would allow the column to reach a maximum strong-axis moment of approximately $0.65R_yM_{px}$ at its top end once plastic hinging occurs at the beam RBS. This top moment would feature a moment diagram with an inflection point at $0.6L$ to $0.7L$ measured from the column base in the elastic range, evidenced by previous works (Elkady and Lignos 2018b).

Table 4-3. Geometrical properties and cross-section capacities of the virtual test matrix.

ID	Section	L_b (mm)	L_b/r_y	d/b_f	$b_f/2t_f$	h/t_w*	GJ/L (kN-m)	AR_yF_y (kN)	R_yM_{px} (kN-m)	R_yM_{py} (kN-m)
CS1-4.3	W360×237	4300	42.2	0.96	6.56	17.0	146.7	11589	1810	920
CS1-6.3	W360×237	6300	61.8	0.96	6.56	17.0	100.1	11589	1810	920
CD1-3.3	W530×150	3300	45.0	1.74	7.68	39.6	50.6	7392	1598	389
CD1-4.3	W530×150	4300	58.6	1.74	7.68	39.6	38.8	7392	1598	389
CD1-5.3	W530×150	5300	72.2	1.74	7.68	39.6	31.5	7392	1598	389
CD1-6.3	W530×150	6300	85.8	1.74	7.68	39.6	26.5	7392	1598	389
CD2-3.3	W530×182	3300	44.5	1.75	6.45	33.0	87.2	8932	1937	477
CD2-4.3	W530×182	4300	58.0	1.75	6.45	33.0	66.9	8932	1937	477
CD2-5.3	W530×182	5300	71.4	1.75	6.45	33.0	54.3	8932	1937	477
CD2-6.3	W530×182	6300	84.9	1.75	6.45	33.0	45.7	8932	1937	477
CD3-3.3	W610×125	3300	66.7	2.67	5.84	48.1	35.9	6122	1413	206
CD3-4.3	W610×125	4300	86.9	2.67	5.84	48.1	27.5	6122	1413	206
CD3-5.3	W610×125	5300	107.1	2.67	5.84	48.1	22.4	6122	1413	206
CD3-6.3	W610×125	6300	127.3	2.67	5.84	48.1	18.8	6122	1413	206
CD4-3.3	W610×153	3300	65.3	2.72	4.60	40.9	68.5	7508	1767	262
CD4-4.3	W610×153	4300	85.1	2.72	4.60	40.9	52.6	7508	1767	262
CD4-5.3	W610×153	5300	105.0	2.72	4.60	40.9	42.7	7508	1767	262
CD4-6.3	W610×153	6300	124.8	2.72	4.60	40.9	35.9	7508	1767	262
CD5-3.3	W610×174	3300	44.2	1.90	7.52	41.0	65.3	8547	2064	450
CD5-4.3	W610×174	4300	57.6	1.90	7.52	41.0	50.1	8547	2064	450
CD5-5.3	W610×174	5300	71.0	1.90	7.52	41.0	40.6	8547	2064	450
CD5-6.3	W610×174	6300	84.3	1.90	7.52	41.0	34.2	8547	2064	450
CD6-3.3	W610×217	3300	43.1	1.91	5.92	34.6	130.1	10665	2637	589
CD6-4.3	W610×217	4300	56.2	1.91	5.92	34.6	99.8	10665	2637	589
CD6-5.3	W610×217	5300	69.3	1.91	5.92	34.6	81.0	10665	2637	589
CD6-6.3	W610×217	6300	82.4	1.91	5.92	34.6	68.1	10665	2637	589

*Clear web depth (h) computed by subtracting two times flange thickness from overall section depth (d-2t_f).

4.6.4 Cyclic Analysis Results

The results obtained from the column stability parameter study were used to compute four response parameters that can be used to quantitatively represent the stability response of the columns and establish a set of criteria to identify column failure modes. These parameters included flexural strength at the base, axial shortening, cross-section twist, and out-of-plane displacements. Twist angles and out-of-plane displacements were recorded at quarter points along the length of the

member measured from the column base, i.e., at 0.25L, 0.50L and 0.75L (see Fig. 4-11d). Table 4-4 summarizes these parameters for the 26 columns analyzed under the axial load of 0.15AF_y. The peak response parameters were recorded at 4% story drift ratios, except those that failed before the last cycle of the target drift was attained.

Table 4-4. Measured response parameters for columns of virtual test matrix under an axial load of 0.15AF_y.

ID	Section	L_b (mm)	Max Achieved Drift (%)	M_{rx}/R_yM_{px}	Δ_{Axial}/L (%)	$\Delta_{out\text{-}of\text{-}plane}/L$ (%)	$\gamma_{cross\text{-}section}$ (% rad)	Failure Type
CS1-4.3	W360×237	4300	4.0	1.07	0.6	0.2	2.9	None
CS1-6.3	W360×237	6300	4.0	1.13	0.3	0.3	5.3	None
CD1-3.3	W530×150	3300	4.0	0.55	2.3	1.0	3.7	None
CD1-4.3	W530×150	4300	4.0	0.64	1.6	0.5	2.6	None
CD1-5.3	W530×150	5300	4.0	0.61	1.3	0.5	9.8	None
CD1-6.3	W530×150	6300	4.0	0.50	1.2	0.9	10.5	None
CD2-3.3	W530×182	3300	4.0	0.78	1.8	0.6	3.2	None
CD2-4.3	W530×182	4300	4.0	0.83	1.3	0.3	2.9	None
CD2-5.3	W530×182	5300	4.0	0.74	1.1	0.6	8.4	None
CD2-6.3	W530×182	6300	4.0	0.67	1.0	0.8	10.4	None
CD3-3.3	W610×125	3300	4.0	0.19	4.0	3.4	4.5	Out-of-plane buckling at base
CD3-4.3	W610×125	4300	4.0	0.22	2.7	2.1	4.8	Out-of-plane buckling at base
CD3-5.3	W610×125	5300	4.0	0.36	1.9	5.6	18.9	Member buckling
CD3-6.3	W610×125	6300	3.0	0.46	0.9	4.2	13.3	Member buckling
CD4-3.3	W610×153	3300	4.0	0.34	3.3	3.4	5.4	Out-of-plane buckling at base
CD4-4.3	W610×153	4300	4.0	0.39	2.2	2.0	5.8	Out-of-plane buckling at base
CD4-5.3	W610×153	5300	4.0	0.41	2.0	6.5	15.9	Member buckling
CD4-6.3	W610×153	6300	3.0	0.46	1.2	5.3	17.2	Member buckling
CD5-3.3	W610×174	3300	4.0	0.45	2.9	1.6	4.0	None
CD5-4.3	W610×174	4300	4.0	0.51	2.1	0.9	3.5	None
CD5-5.3	W610×174	5300	4.0	0.61	1.5	0.5	3.5	None
CD5-6.3	W610×174	6300	4.0	0.46	1.4	1.1	11.7	Member buckling
CD6-3.3	W610×217	3300	4.0	0.68	2.3	1.2	4.1	None
CD6-4.3	W610×217	4300	4.0	0.74	1.7	0.6	3.6	None
CD6-5.3	W610×217	5300	4.0	0.74	1.3	0.5	9.5	None
CD6-6.3	W610×217	6300	4.0	0.62	1.2	1.0	11.1	None

Two failure modes dominated the response of the columns studied here: 1) out-of-plane buckling at the column base due to severe local buckling, and 2) member buckling along the length of the

column. Fig. 4-18 shows an example of out-of-plane buckling at the base observed for the 4.3m-long W610×153 column, and an example of member buckling observed for the 5.3m-long W610×153 column. The failure modes recorded for each of the 26 columns examined under the axial load of $0.15AF_y$ are given in Table 4-4. All W610×125 and W610×153 columns failed by 4% drift. The 3.3m- and 4.3m-long W610×125 and W610×153 failed by out-of-plane buckling at the base due to axial shortening and out-of-plane displacements exceeding $2\%L$. However, the 5.3m- and 6.3-m long columns failed due to member buckling accompanied by twist angles well above 0.08 rad; the 6.3-m long column failed to reach 4% drift. The 6.3m-long W610×174 column failed by member buckling with excessive cross-section twist, e.g., angle exceeding 0.11 rad. No buckling was observed for the rest of the columns studied here.

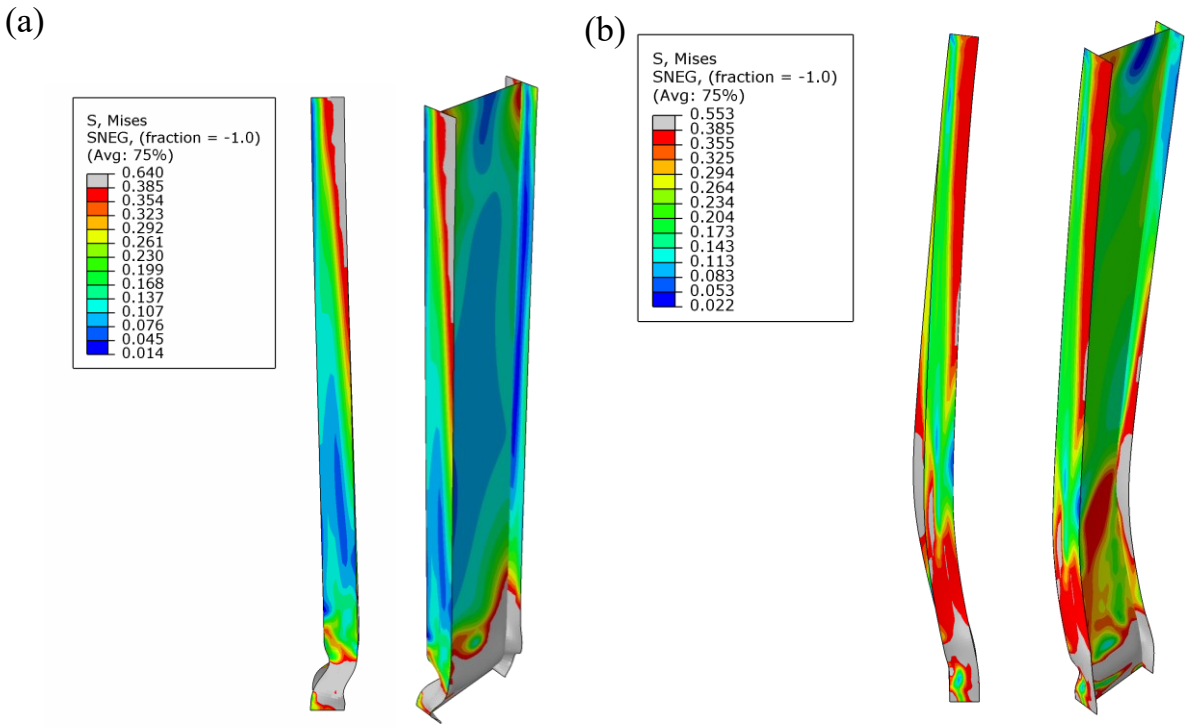

Figure 4-18. In-plane and out-of-plane deformed-shape and von-Mises stress distribution for: (a) W610×153 column with L_b = 4300 mm, d/b_f = 2.72, h/t_w = 40.9 under $0.15AF_y$ failing by out-of-plane buckling at the base; (b) W610×153 column with L_b = 5300 mm, d/b_f = 2.72, h/t_w = 40.9 under $0.15AF_y$ failing by member buckling.

Column strength and deformation response parameters (reported in Table 4-4) are plotted against two geometric parameters, global slenderness ratio and cross-section aspect ratio, in Figure 4-19. As shown, two CS columns exhibited no noticeable strength degradation owing to their stable cyclic response with minor web and flange local buckling at the base (Newell and Uang 2008), even in the presence of fairly considerable weak-axis bending. The results of the deep CD columns showed that they experienced severe strength degradation compared to $R_y M_{px}$. Referring to Figs. 4-19a and 4-19b, a descending trend was observed for the flexural strength of the column as both L_b/r_y and d/b_f increase. All three deformation measures considered here, axial shortening, out-of-plane displacement, and cross-section twist, are plotted against L_b/r_y and d/b_f as shown in Figs. 4-19c to 4-19h. All three deformation parameters increase as either d/b_f or L_b/r_y increases, except axial shortening against L_b/r_y, for which no clear trend was observed. In general, shorter columns, L_b = 3.3 and 4.3 m, experienced failure exhibiting large axial shortening (> 2%L) and out-of-plane displacement near the base plastic hinge (> 2%L) accompanied by large strength deterioration, promoting column out-of-plane buckling at the base due to severe local buckling near the plastic hinge location, i.e., Failure Mode 1. Whereas longer, 5.3 m and 6.3 m columns underwent a larger cross-section twist angle (> 0.08 rad.) near the base plastic hinge plus larger out-of-plane deformations distributed along the member length; this was accompanied by large strength deterioration, showing a tendency for member buckling, i.e., Failure Mode 2.

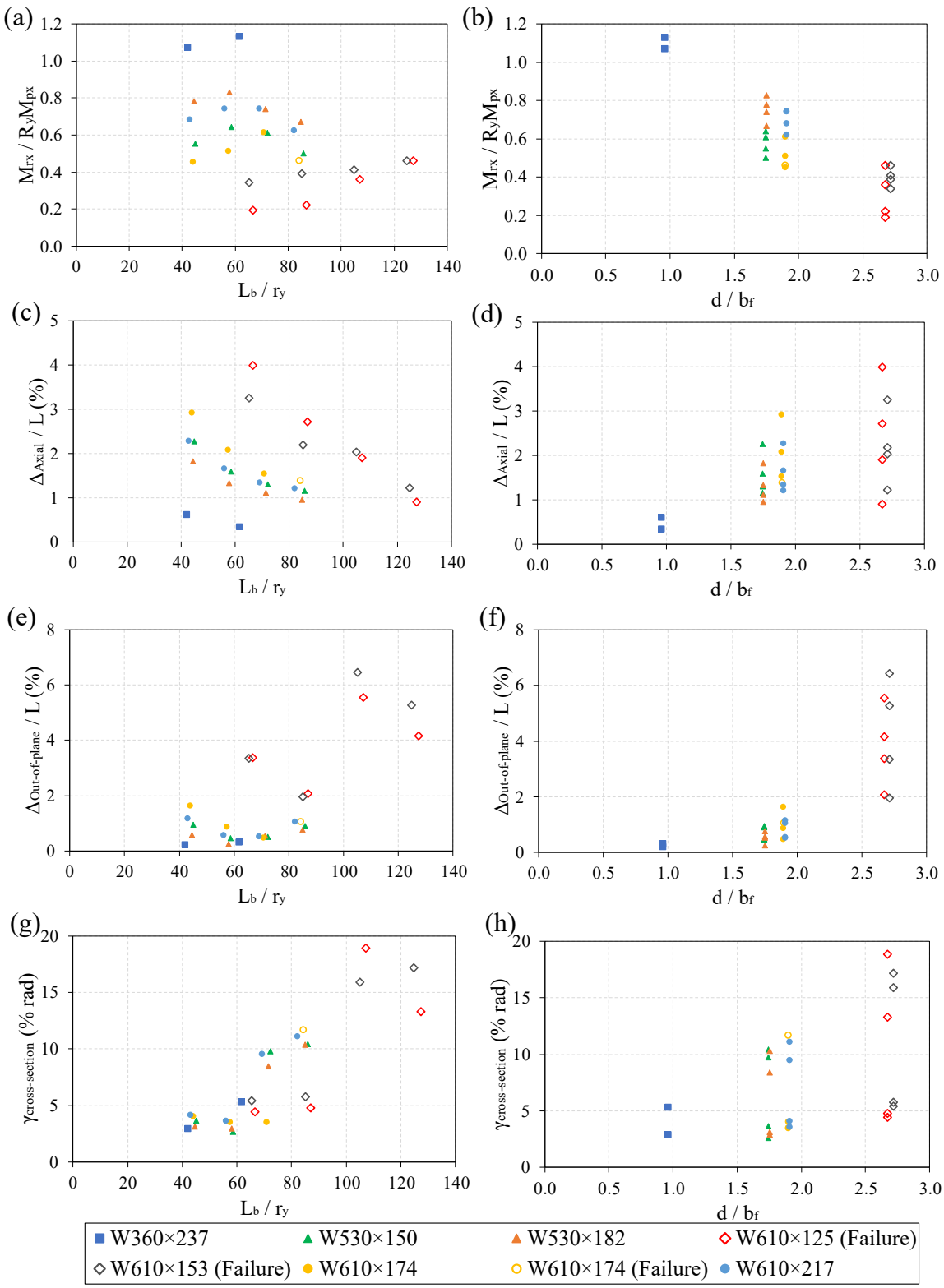

Figure 4-19. Column strength and deformation response parameters: (a-b) Flexural strength at the base vs. L_b/r_y and d/b_f; (c-d) Axial shortening vs. L_b/r_y and d/b_f; (e-f) Out-of-plane displacement at the base vs. L_b/r_y and d/b_f; (g-h) Cross-section twist angle vs. L_b/r_y and d/b_f (data points with a hollow marker indicate failure).

Based on the parameter study results and the trends observed in Fig. 4-19, a combination of strength and deformation criteria was established to identify whether a column has failed. These criteria are 1) flexural strength falling below 50% times the member's probable plastic moment capacity R_yM_{px} accompanied by axial shortening and out-of-plane displacement measured near the base plastic hinge exceeding 2%L by the end of the analysis, which represents out-of-plane buckling at the base; 2) flexural strength lower than $0.50R_yM_{px}$ accompanied by a cross-section twist angle greater than 0.08 rad. by the end of the analysis, which represents member buckling or lateral-torsional buckling (LTB). Both failure modes were intended to characterize a condition in which the column experiences the complete loss of gravity load-carrying capacity, i.e., dynamic instability. The failure cases identified using this definition are listed using a hollow marker in Fig. 4-19. As shown, the cases identified as failed almost always lie on the boundary of L_b/r_y and d/b_f axes, i.e., $L_b/r_y > 65$ and $d/b_f > 2.6$, suggesting the correlation between the column stability condition and the global slenderness and the cross-section aspect ratios. It is also inferred from the data points in Fig. 4-19 that the column with a higher d/b_f remains stable only when L_b/r_y is low and those with high L_b/r_y require more square sections, i.e., $d/b_f \approx 1.0$, to avoid instability.

The cyclic analyses on the selected columns of Table 4-3 were repeated under a higher axial load of $0.25AF_y$, corresponding to 23% of the probable axial capacity (AR_yF_y) assumed in the model. Table 4-5 summarizes the column strength and deformation response parameters used to evaluate the stability of the MRF columns here. The square CS columns still exhibited a stable behaviour with limited strength degradation at a 4% drift cycle. The deep CD columns, however, exhibited significant strength degradation (more than $0.60R_yM_{px}$), high axial shortening (on average 3%L), and out-of-plane displacement (on average 2.6%L). Referring to the identified failure modes in

Table 4-5, shorter 3.3m- and 4.3m-long columns exhibited out-of-plane buckling at the base due to severe out-of-plane displacements near the base plastic hinge (close to or exceeding 2.0%L) accompanied by large axial shortening (> 2%L). Columns measuring 5.3 m and 6.3 m in length failed by member buckling experiencing large twists (on average 0.14 rad.). The majority of the columns exhibiting member buckling also experienced appreciable axial shortening (on average 1.9%L) and out-of-plane displacement at the bottom half of the member (on average 2.4%L) due to the increased axial load, i.e., 1.67 times higher axial load. Fig. 4-20a and 4-20b show the out-plane buckling at the base for the W530×182 column with a 3.3 m length and member buckling for the 5.3m-long W530×182 column, both under the constant axial force of 0.25AF_y.

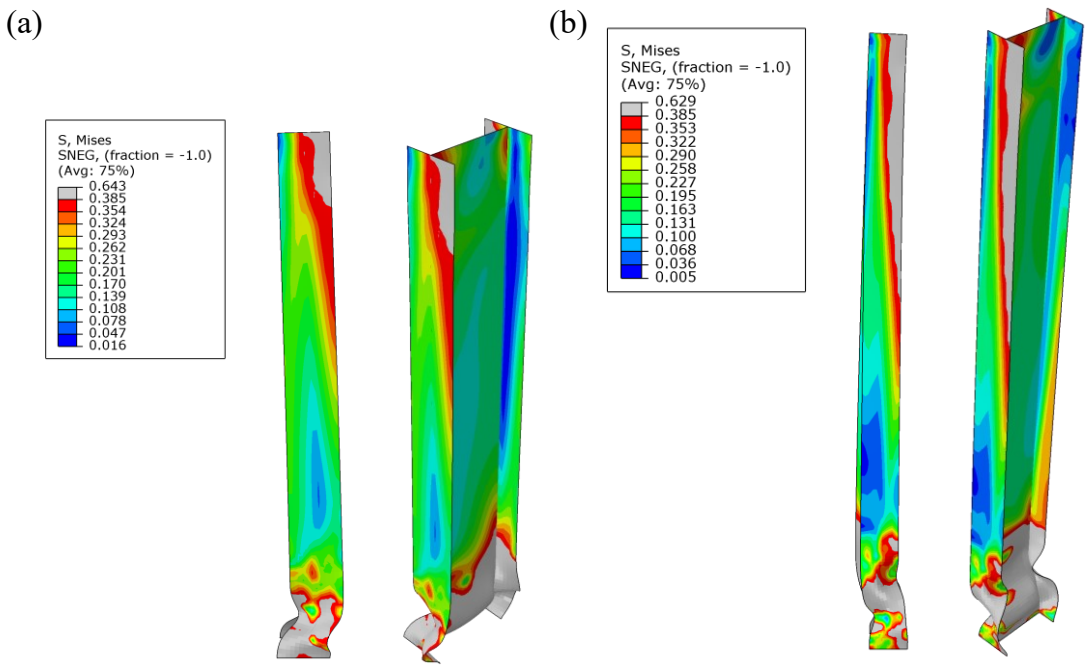

Figure 4-20. In-plane and out-of-plane deformed-shape and von-Mises stress distribution for: (a) W530×182 column with L_b = 3300 mm, d/b_f = 1.75, h/t_w = 33.0 under 0.25AF_y failing by out-of-plane buckling at the base; (b) W530×182 column with L_b = 5300 mm, d/b_f = 1.75, h/t_w = 33.0 under 0.25AF_y failing by member buckling.

The correlations between the column strength and deformation response parameters considered here and the column failure modes observed under an axial load equal to 0.25AF_y agree with those

described for the failure cases under an axial load of $0.15AF_y$. Moreover, the results of the analyses under the heavier axial load confirmed the detrimental impact of the axial load level on the column cyclic response (Elkady and Lignos 2018b, Ozkula et al. 2017a, 2019, 2021), which must be considered when checking column stability under seismic loads. Supplementary data detailing strength and deformation response parameters obtained from the parametric study analyses are provided in Appendix A.

Table 4-5. Measured response parameters for columns of virtual test matrix under an axial load of $0.25AF_y$.

ID	Section	L_b (mm)	Max Achieved Drift (%)	M_{rx}/R_yM_{px}	Δ_{Axial}/L (%)	$\Delta_{out\text{-}of\text{-}plane}/L$ (%)	$\gamma_{cross\text{-}section}$ (% rad)	Failure Type
CS1-4.3	W360×237	4300	4.0	0.90	1.1	0.2	3.5	None
CS1-6.3	W360×237	6300	4.0	0.95	0.6	0.4	8.5	None
CD1-3.3	W530×150	3300	4.0	0.05	5.3	3.0	3.9	Out-of-plane buckling at base
CD1-4.3	W530×150	4300	4.0	0.12	3.5	1.8	4.1	Out-of-plane buckling at base
CD1-5.3	W530×150	5300	4.0	0.20	2.6	2.4	9.5	Member buckling
CD1-6.3	W530×150	6300	4.0	0.17	2.3	2.8	9.0	Member buckling
CD2-3.3	W530×182	3300	4.0	0.29	3.9	2.2	4.1	Out-of-plane buckling at base
CD2-4.3	W530×182	4300	4.0	0.40	2.7	1.1	5.1	Out-of-plane buckling at base
CD2-5.3	W530×182	5300	4.0	0.32	2.3	1.9	10.4	Member buckling
CD2-6.3	W530×182	6300	4.0	0.32	1.9	1.9	11.4	Member buckling
CD3-3.3	W610×125	3300	3.0	0.08	4.0	3.7	3.5	Out-of-plane buckling at base
CD3-4.3	W610×125	4300	3.0	0.09	3.2	2.9	4.6	Out-of-plane buckling at base
CD3-5.3	W610×125	5300	2.0	0.45	0.9	3.2	15.3	Member buckling
CD3-6.3	W610×125	6300	2.0	0.57	0.5	3.1	10.7	Member buckling
CD4-3.3	W610×153	3300	4.0	0.07	5.4	5.3	4.6	Out-of-plane buckling at base
CD4-4.3	W610×153	4300	3.0	0.18	2.8	2.9	4.7	Out-of-plane buckling at base
CD4-5.3	W610×153	5300	2.0	0.42	1.0	3.9	12.8	Member buckling
CD4-6.3	W610×153	6300	2.0	0.58	0.5	3.1	8.5	Member buckling
CD5-3.3	W610×174	3300	4.0	0.11	5.4	3.3	3.4	Out-of-plane buckling at base
CD5-4.3	W610×174	4300	4.0	0.03	4.3	2.6	3.6	Out-of-plane buckling at base
CD5-5.3	W610×174	5300	4.0	0.16	3.4	0.8	31.4	Member buckling
CD5-6.3	W610×174	6300	4.0	0.20	2.2	2.5	8.2	Member buckling
CD6-3.3	W610×217	3300	4.0	0.20	5.0	3.3	4.3	Out-of-plane buckling at base
CD6-4.3	W610×217	4300	4.0	0.23	3.6	2.1	4.5	Out-of-plane buckling at base
CD6-5.3	W610×217	5300	4.0	0.26	2.7	1.0	29.2	Member buckling
CD6-6.3	W610×217	6300	4.0	0.26	2.3	2.6	10.7	Member buckling

4.6.5 Stability Design Recommendations for First Storey Wide-Flange Columns

Based on the column stability parameter study presented herein, in particular, the correlation between the column strength and deformation response parameters and the geometrical properties, including the member global slenderness ratio L_b/r_y and cross-section aspect ratio d/b_f, and the axial load ratio, a simple empirical equation for evaluating the out-of-plane stability of wide-flange steel columns with base plastic hinging was developed as:

$$\left(\frac{C_f/AF_y}{0.15}\right)^{1.4}\left[\left(\frac{L_b/r_y}{108}\right)^2+\left(\frac{d/b_f}{3.0}\right)^2\right]\leq 1.0 \quad (4\text{-}1)$$

The proposed equation couples the global slenderness ratio, cross-section aspect ratio, and axial load ratio to predict the stability response of wide-flange columns with base plastic hinging. The proposed stability design equation is given in Fig. 4-21 against the column cases that failed or passed the criteria set as described earlier under both $0.15AF_y$ and $0.25AF_y$ axial load levels. This equation can well predict the adequacy of columns with square cross-sections ($d/b_f \approx 1.0$) as proven by the past experimental studies (Newell and Uang 2008) while eliminating deep slender columns with $d/b_f > 2.6$ such as the W610×125 or W610×153 sections under the $0.15AF_y$ axial load level (Fig. 4-21a) and all deep slender columns, i.e., $d/b_f > 1.75$, under the $0.25AF_y$ axial load level (Fig. 4-21b), which are prone to instability under seismic load effects. Furthermore, the range of acceptable section aspect rations, i.e., $d/b_f = 0.0$ to 3.0, encompasses the majority of Class 1 wide-flange members that would be used in practice as first-storey MRF columns. The proposed interaction equation should be used within the range of geometrical and constitutional properties considered in this study. This equation can be used in lieu of the CSA S16 constant global slenderness ratio limit L_b/r_y (Eq. 2-3), which is equal to 50 assuming $\kappa = 0$ and $F_y = 350$ MPa, as this limit was found to be conservative and may eliminate a large number of sections that can be

used in practice in Ductile steel MRFs. Note that the uncoupled L_b/r_y limit proposed in Section 3.3.4 was 70, assuming $\kappa = 0.45$.

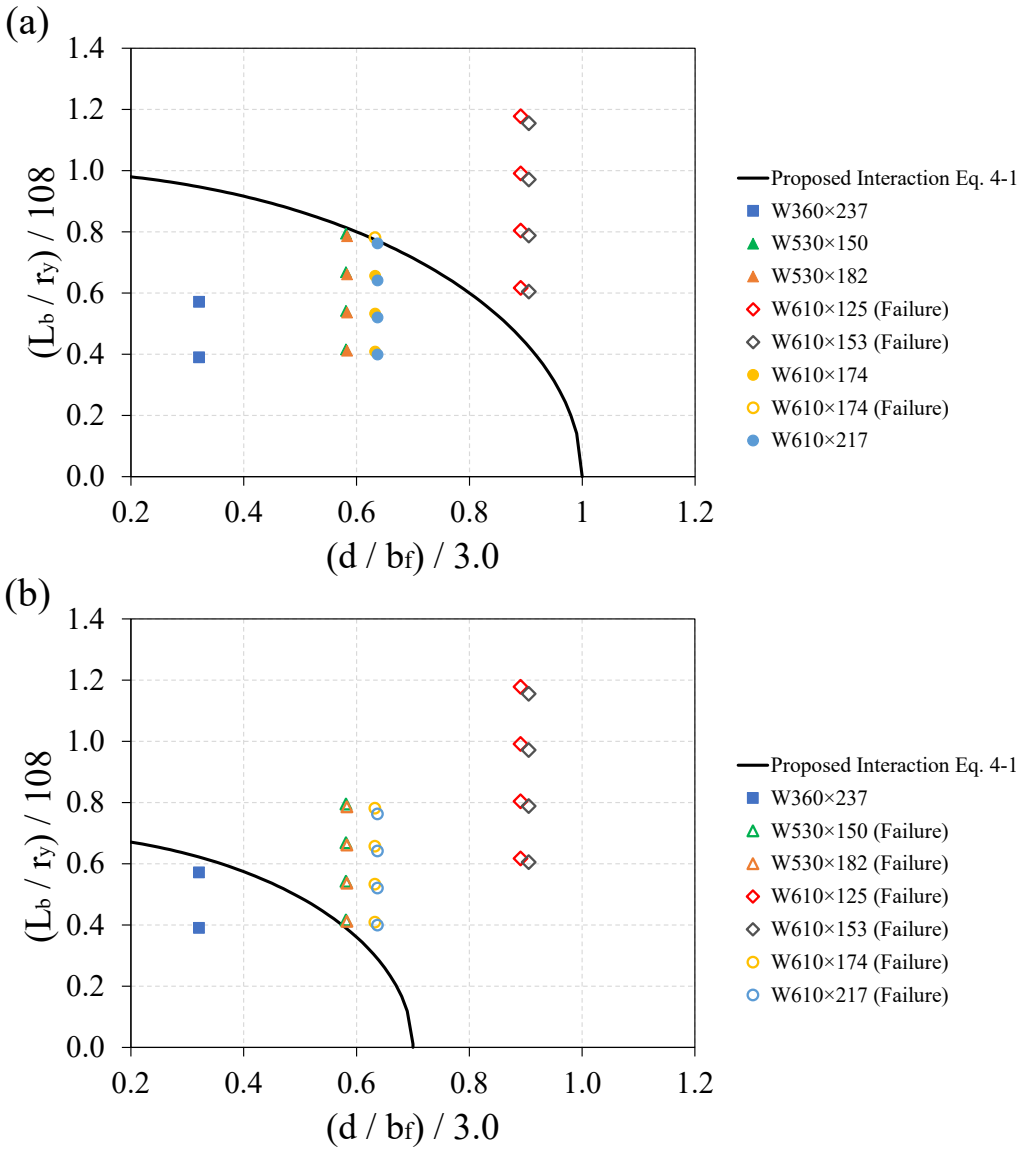

Figure 4-21. Proposed global slenderness and aspect ratio interaction: (a) $0.15AF_y$ axial load level; (b) $0.25AF_y$ axial load level (data points with an empty marker indicate failure).

4.6.6 Evaluation of the Web Slenderness Ratio Limit

The web slenderness ratio was also investigated using 52 columns analyzed under cyclic loading. Fig. 4-22 provides L_b/r_y versus h/t_w at the two different axial load levels. The CSA S16 web slenderness limit (Eq. 2-4) and the limits proposed by Ozkula et al. (2019 and 2021) given in Eq.

2-6 are also provided. Under the 0.15AF_y axial load level, the current CSA S16 limit of 37.0 can well predict the columns that failed, but as the axial load increases to 0.25AF_y, this limit is deemed to poorly predict instability cases. The limit provided by Ozkula et al. (2021) barely eliminates the W610×153 and W610×174 columns that failed under 0.15AF_y. Under the higher 0.25AF_y axial load, however, this limit can well predict columns that failed, suggesting that this limit can better represent the seismic stability response of wide-flange columns with base plastic hinging by explicitly considering the influence of the axial force.

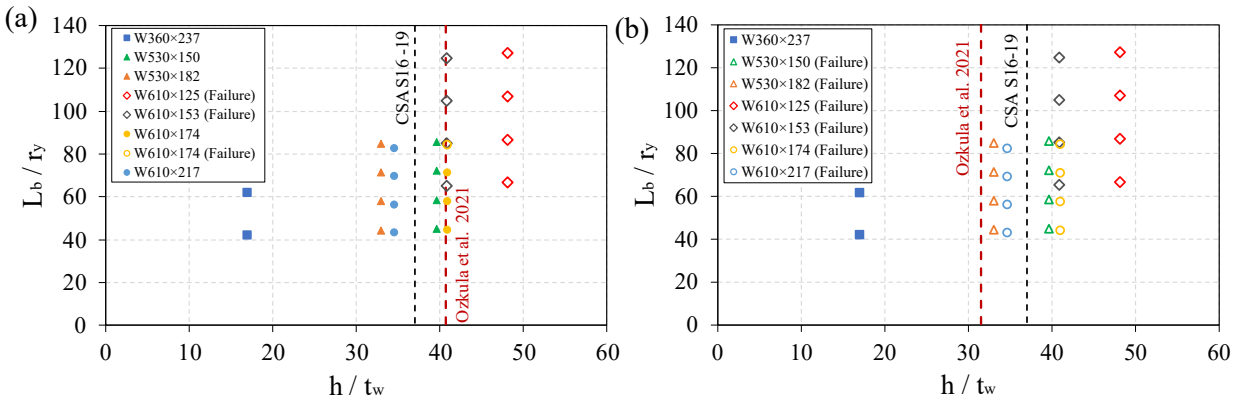

Figure 4-22. Global slenderness versus web slenderness ratio: (a) 0.15AF_y axial load level; (b) 0.25AF_y axial load level (data points with an empty marker indicate failure).

4.6.7 Summary

A prototype Type D MRF consisting of relatively deep and slender columns was designed per the Canadian steel design standard. The frame was then analyzed using the NLRHA, and the three most critical ground motion records that created the largest lateral displacement demands were identified. The three-dimensional continuum-based finite element model (CFEM) of the MRF subassembly consisting of the exterior bay plus half of the adjacent interior bay was developed. The MRF subassembly was analyzed under the selected ground motion records to evaluate the three-dimensional response of the MRF, and in particular, the force and deformation demands induced in the interior first-storey column. The NLRHA of the MRF subassembly was also used

to develop a weak-axis bending history that was used alongside a constant axial compression force and in-plane cyclic displacement demand to examine the stability response of a set of 52 wide-flange columns with varying L_b/r_y, d/b_f, $b_f/2t_f$, h/t_w and axial load ratio C_f/AF_y. The results of the parameter study confirmed two stability-related failure modes, out-of-plane buckling at the base with a large lateral displacement near the base, often observed for shorter columns, and member buckling with a large twist angle often observed for longer members. Both modes were accompanied by significant strength degradation at the base plastic hinge. Moreover, a correlation was found between the column strength and deformation response parameters, including flexural strength at the base, axial shortening, out-of-plane displacement, cross-section twist, and the geometrical properties associated with the member L_b/r_y and cross-section aspect ratio d/b_f, plus the column axial load ratio. An equation that couples the global slenderness ratio, cross-section aspect ratio, and axial load ratio was finally developed based on the parameter study results to predict the stability response of wide-flange columns with base plastic hinging.

Chapter 5. Conclusions and Recommendations

5.1 Summary

The objective of this M.Sc. research was to evaluate the seismic behaviour and quantify seismic force and deformation demands of wide-flange columns with base plastic hinging in Ductile (Type D) steel MRFs and improve the stability design requirements prescribed by the 2019 Canadian steel design standard CSA S16.

A prototype five-storey Ductile MRF was selected and designed following the CSA S16 seismic design provisions. Three column design scenarios were considered: 1) square columns with $d/b_f \approx 1.0$ designed in accordance with the current CSA S16 provisions, 2) deep columns with $d/b_f \approx 1.9$ designed in accordance with the current CSA S16 provisions, and 3) deep columns with $d/b_f \approx 1.9$ designed excluding the special stability design provisions specified for MRF columns. The concentrated plasticity-based numerical model of the MRF was then developed in the OpenSees program. The model was used to perform nonlinear response history analyses under 33 ground motion records representing three predominant seismic actions in western Canada. The global and local responses of the alternative designs, including storey drift ratios, seismic-induced forces, and rotations of the columns, were evaluated using NLRHA results. A continuum-based finite element model of the interior and exterior columns isolated from the prototype MRF designs was developed and subjected to the displacements and axial load histories obtained from the NLRHA of the three most critical ground motion records. The results of the NLRHA of the frame and those from the CFEM of the isolated columns were used to evaluate the CSA S16 stability design requirements for the first-storey columns of Type D MRFs and propose improvements to those provisions.

The five-storey prototype MRF was redesigned using more slender (L_b/r_y > 80) wide-flange columns, exceeding the limit proposed in the first phase of the study and replicating the W610×153 experimental test specimens as the first-storey column. A three-dimensional continuum-based finite element model (CFEM) of the MRF subassembly consisting of the exterior bay plus half of the adjacent interior bay was created. Beams, columns, and beam-to-column connections were explicitly simulated in this model. The MRF subassembly was intended to study the three-dimensional response of steel MRFs, including the out-of-plane deformation and torsional response of RBS connections and the weak-axis bending demands induced in the first-storey column as a result of RBS deformation and local buckling near the base plastic hinge. The subassembly model was then subjected to earthquake ground motions (the three most critical subduction records selected). A weak-axis bending moment loading protocol was created using the results of the NLRHA of the MRF subassembly, which in combination with the in-plane cyclic displacement history and a constant gravity-induced axial compression load, were used to perform a parameter study on column stability response using the refined CFEM of the isolated column. A total of 52 columns were analyzed by varying the section size (W360×237, W530×150, W530×182, W610×125, W610×153, W610×174, and W610×217), unbraced length (L = 3300, 4300, 5300, and 6300 mm), and axial load ratios (C_f/C_y = 0.15AF_y and 0.25AF_y). The axial load ratios correspond to 14 and 23% of the column's probable axial capacity. The results of the parameter study were used to identify column strength and deformation response parameters, including base moment, axial shortening, out-of-plane displacement near the base plastic hinge, and cross-section twist angle, which were then used to determine column instability modes, including out-of-plane buckling at the base and member buckling. Finally, a simple empirical equation as a function of the global slenderness ratio, cross-section aspect ratio, and axial load

ratio was proposed in the framework of the Canadian steel design standard, which was found to well represent the stability condition of MRF columns with base plastic hinging.

5.2 Scientific Contributions

This M.Sc. project made the following original scientific contributions:

- Seismic design provisions implicit in Canadian steel design standard that produce over-restrictive stability checks for the columns of Ductile steel MRFs were identified.
- Influential paraeters affecting the seismic stability of columns with base plastic hinging in Ductile steel MRFs were quantified.
- New seismic design recommendations were developed in the framework of the Canadian steel design standard to improve the stability of wide-flange columns in the first storey of Ductile steel MRFs.
- A new interaction equation was introduced using the global slenderness ratio (L_b/r_y), cross-section aspect ratio (d/b_f), and constant axial load ratio (C_f/AF_y) for selecting wide-flange columns with base plastic hinges with adequate stability under cyclic loading.

5.3 Conclusions and Recommendations for Design

The key findings of this M.Sc. research project can be summarized as follows:

- The results obtained from NLRHA suggest that the strong column-weak beam check at the beam-to-column joint may not be sufficient to prevent member instability and ensure elastic response of the columns above the first storey. It is necessary to verify in-plane and out-of-plane stability of these columns under gravity loads and bending arising from beams reaching their probable flexural resistance.
- The current CSA S16 axial load limit of $0.30AF_y$ for exterior first-storey columns is conservative and can control the design of such columns. The limit for exterior first-storey

columns can be increased to $0.35AF_y$ as the exterior columns subjected to the proposed axial load limit in this study exhibited stable seismic response with limited strength degradation ($M_{rx} > 0.80R_yM_{px}$) and axial shortening (<1%L). This is due to dynamic overturning effects causing highly fluctuating axial loads between compression and tension for exterior columns.

- The evaluation of the equivalent moment factor κ using the NLRHA showed that, on average, $\kappa = 0.45$ could be used for first-storey columns, which results in a lateral bracing limit of $L_b/r_y = 70$.
- The results from the CFEM of the MRF subassembly analyzed under earthquake ground motion accelerations showed out-of-plane displacement and twist in the first storey W610×153 column, which combined with large in-plane displacement resulted in more severe local buckling near the base plastic hinge. The out-of-plane displacements and twist are caused by RBS out-of-plane movements, which tend to occur in opposite directions for the two RBS connections on both sides of the column. The local buckling amplifies the out-of-plane displacement near the base of the column.
- Using the subassembly model, the peak out-of-plane displacement measured at the RBS locations reached $1.3r_y$ for both beams connected to the column on each side but moving in opposite directions.
- The peak cross-section twist angle in the interior first-storey column was observed near the top end of the member due to the torsional demands imposed by the RBS and reached over 0.10 rad at 3.4% chord rotation.
- Weak-axis bending moments measured at the top end of the first-storey columns of the MRF subassembly tend to increase linearly by increasing drift demands, with the peak

value of $0.40R_yM_{py}$ at 3.4% chord rotation. The history of out-of-plane bending was extracted from the NLRHA results of the MRF subassembly and used to develop an out-of-plane moment history, which, in turn, was used to examine the three-dimensional response of the isolated first-storey columns, including the weak-axis moment.

- Observations from the parameter study of 26 wide-flange columns under cyclic loading and two constant axial load levels ($0.15AF_y$ and $0.25AF_y$) showed that two failure modes dominate the column response: 1) out-of-plane buckling at the column base due to severe local buckling, and 2) member buckling along the length of the column. The out-of-plane buckling at the base is identified when the flexural strength falls below 50% times the member's probable plastic moment capacity R_yM_{px} accompanied by axial shortening and out-of-plane displacement measured near the base plastic hinge exceeding $2\%L$ at large storey drifts. The member buckling is identified when the flexural strength falls below $0.50R_yM_{px}$ accompanied by a cross-section twist angle greater than 0.08 rad. plus greater out-of-plane deformations distributed along the member length at large storey drifts.
- At shorter lengths ($L \leq 4300$ mm), columns tend to display out-of-plane buckling at the base plastic hinge, while columns display member buckling at longer lengths ($L \geq 5300$ mm).
- The column stability parameter study results showed a descending trend for the flexural strength of the column as both L_b/r_y and d/b_f increase. All three deformation parameters increase as either d/b_f or L_b/r_y increases, except axial shortening against L_b/r_y for which no clear trend was observed.
- The heavier axial load $0.25AF_y$ imposed on the columns of the parameter study resulted in more severe local bucking near the base and accelerated flexural strength degradation.

- A correlation was found between the column strength and deformation response parameters, including flexural strength at the base, axial shortening, out-of-plane displacement, cross-section twist, and the geometrical properties associated with the member L_b/r_y, cross-section aspect ratio $d/b_{f,}$ and axial load.
- An equation that couples the global slenderness ratio, cross-section aspect ratio, and axial load ratio was developed based on the parameter study results to predict the stability response of wide-flange columns with base plastic hinging. This equation can supersede the overly conservative uncoupled L_b/r_y limit of 50 (assuming $\kappa = 0$ and $F_y = 345$ MPa) currently prescribed in CSA S16, provided that the column meets all the other code strength and stability requirements.
- The current S16 web slenderness ratio limit of 37.0 for first-storey columns subjected to axial loads greater than or equal to $0.15AF_y$ was evaluated using the 52 wide-flange sections in the parameter study. The results showed that the current limit may not appropriately predict the stability response of members under larger axial loads such as $0.25AF_y$. A variable web slenderness ratio limit that decreases with increasing axial load level is needed.

5.4 Limitations

The findings of this study should be used within the range of parameters and assumptions made here:

- MRFs designed as part of this study were limited to a five-storey building located on site Class C in Vancouver, British Colombia, Canada. The number of stories and storey heights may affect the seismic demand of MRF members.

- This study only considers the seismic hazard sources likely in Western Canada. Other seismicity sources for different locations across Canada may result in a different response for the MRFs studied herein.
- The ground motions in this study were scaled to the design level pseudo-spectral acceleration under NBCC 2015, which corresponds to a hazard level with a 2% probably of exceedance in 50 years, representing a major seismic event. Collapse analysis and the response of the MRFs and their columns under records scaled above the design level is not within this project's scope.
- Column splices were not explicitly modelled in this study. Explicit modeling of splices may affect the lateral stiffness of steel MRFs.
- Column bases were assumed to be fully fixed in the numerical models developed here. The column bases however will have some inherent flexibility in practice due to the flexibility of the base plate, anchor rods and grout, which may impact the hysteretic behaviour and stability of members with base plastic hinges.
- The influence of perpendicular seismic force-resisting system on the MRF studied in this study was ignored. The perpendicular seismic force-resisting system such as steel MRFs or steel buckling-restrained braced frames can influence the seismic-induced demands on the MRF members and stability of its columns.
- The stability response of steel MRF columns under cyclic displacement histories (e.g., Elkady and Lignos 2018a, 2018b; Ozkula et al. 2017b, 2017c) such as the symmetric cyclic loading protocol recommended by AISC Seismic Provisions (2016) or collapse-consistent loading protocols (Suzuki and Lignos 2020) may result in conservative demands in regions where near field earthquakes are expected, but such displacement histories can provide an

envelope of anticipated seismic demands in regions with deep and long duration earthquakes such as subduction interface earthquakes expected in the west coast of Canada (Suzuki and Lignos 2021). Such standard loading protocols ignore the influence of the rest of the structure on column demands and may not necessarily account for the ground motion characteristics specific to the building location.

- The component-based finite element model of the isolated first-storey column with base plastic hinging developed here neglects the beam-to-column web panel zone joint and upper storey columns, which may slightly influence the column seismic-induced demands and stability response.

5.5 Recommendations for Future Work

The following research directions are recommended in future studies based on the findings of this thesis:

- Large-scale laboratory tests should be performed on steel wide-flange columns with base plastic hinging to further validate the numerical modelling assumptions used here and verify the design recommendations proposed.
- The MRF subassembly study should be expanded by varying the column sizes, heights, and ground motion records to further investigate the response of first-storey columns considering the influence of upper-storey columns, beams, and connections. However, the efficiency of computation should be given priority.
- Hybrid simulations where the first-storey column is physically tested in the laboratory and the rest of the MRF (or MRF subassembly) is numerically modelled can be used as an efficient tool to examine the influence of column boundary conditions while testing only a structural component.

- The column parameter study database should be expanded by including other wide-flange cross-sections with various width-to-thickness ratios to further validate and refine the proposed stability design equation.
- The influence of the torsional demand on the column cyclic response should be studied by including the influence of torsional slenderness offered by upper stories and adjacent beams while imposing the torsional demand that appropriately represents twist observed in the columns with base plastic hinging.
- The effect of the flexibility of the column base condition on the stability response of the first storey MRF columns should be evaluated using an enhanced finite element model accounting for the column base flexibility and full-scale experimental testing.

References

AISC. (2016a). *Code of standard practice for steel buildings and bridges*, ANSI/AISC 303-16. American Institute of Steel Construction.

AISC. (2016b). *Seismic provisions for structural steel buildings,* ANSI/AISC 341-16. American Institute of Steel Construction.

AISC. (2016c). *Prequalified for special and intermediate steel moment frames for seismic applications,* ANSI/AISC 358-16. In. Chicago, IL, USA: American Institute of Steel Construction.

AISC. (2016d). *Specifications for structural steel buildings,* ANSI/AISC 360-16. American Institute of Steel Construction.

Ashrafi, A., & Imanpour, A. (2021). Seismic response of steel multi-tiered eccentrically braced frames. *Journal of Constructional Steel Research*, 181, 106600.

ASTM. (2003). *Standard specification for general requirements for rolled structural steel bars, plates, shapes, and sheet piling,* ASTM A6/A6M-04b. American Society for Testing and Materials.

Bansal, J. P. (1971). *The lateral instability of continuous steel beams.* PhD Thesis. University of Austin, Texas, USA.

Bech, D., Tremayne, B., & Houston, J. (2015). Proposed changes to steel column evaluation criteria for existing buildings. *Second ATC & SEI Conf. on Improving the Seismic Performance of Existing Buildings and Other Structures*, American Society of Civil Engineers, San Francisco, CA.

Bruneau, M., Uang, C.-M., & Sabelli, R. (2011). *Ductile design of steel structures*, 2nd Edition. McGraw-Hill Professional.

CEN. (2003). *Eurocode 8 – Design provisions for earthquake resistant structures*, EN-1998-1:2003. E, Comite Europeen de Normalization, Brussels, Belgium.

CSA (2019). *Design of steel structures*. Canadian Standards Association Group. Mississauga, ON, Canada.

Chi, B., & Uang, C.-M. (2002). Cyclic response and design recommendations of reduced beam section moment connections with deep columns. *Journal of Structural Engineering*, 128(4), 464-473.

CISC. (2014). *Moment Connections for Seismic Applications,* 2nd Edition. Canadian Institute of Steel Construction. Markham, ON, Canada.

Computers & Structures Inc. (2019). SAP2000. In. Walnut Creek, CA, US.

Dassault Systemes Simulia Corporation (2020). ABAQUS-FEA/CAE. In. Johnston, Rhode Island, USA.

Cravero, J., Ahmed, E., & Lignos, D. (2020). Experimental evaluation and numerical modeling of wide-flange steel columns subjected to constant and variable axial load coupled with lateral Drift Demands. *Journal of Structural Engineering*, 146(3), 04019222.

Elkady, A. (2016). *Collapse risk assessment of steel moment resisting frames designed with deep wide-flange columns in seismic regions.* PhD Thesis. McGill University, Canada.

Elkady, A., & Lignos, D. (2014a). Analytical investigation of the cyclic behavior and plastic hinge formation in deep wide-flange steel beam-columns. *Bulletin of Earthquake Engineering*, 13(4), 1097–1118.

Elkady, A., & Lignos, D. (2014b). Modeling of the composite action in fully restrained beam-to-column connections: implications in the seismic design and collapse capacity of steel special moment frames. *Earthquake Engineering & Structural Dynamics*, 43(13), 1935-1954.

Elkady, A., & Lignos, D. (2017a). Full-scale cyclic testing of deep slender wide-flange steel beam-columns under unidirectional and bidirectional lateral drift demands. *16th World Conference on Earthquake Engineering,* Santiago, Chile.

Elkady, A., & Lignos, D. (2017b). Stability requirements of deep steel wide-flange columns under cyclic loading. *Proceedings of the Annual Stability Conference Structural Stability Research Council*, San Antonio, Texas, USA.

Elkady, A., & Lignos, D. G. (2018a). Full-scale testing of deep wide-flange steel columns under multi axis cyclic loading: Loading sequence, boundary effects, and lateral stability bracing force demands. *Journal of Structural Engineering*, 144(2), 04017189.

Elkady, A., & Lignos, D. G. (2018b). Improved seismic design and nonlinear modeling recommendations for wide-flange steel columns. *Journal of Structural Engineering*, 144(9), 04018162.

FEMA. (2000a). *Recommended seismic design criteria for new steel moment-frame buildings,* FEMA-350*.* Federal Emergency Management Agency.

FEMA. (2000b). *State of the art report on connection performance,* FEMA-355D. Federal Emergency Management Agency.

Filiatrault, A., Tremblay, R., Christopoulos, C., Folz, B., & Pettinga, D. (2013). *Elements of Earthquake Engineering and Structural Dynamics*, 3rd edition. Presses Internationale Polytechnique.

Galambos, T.V. and Ketter, R.L. (1958). *Columns under combined bending and thrust*. Fritz Engineering Laboratory Report 205A.21, Bethlehem, Pennsylvania.

Gupta, A., & Krawinkler, H. (1999). *Seismic demands for the performance evaluation of steel moment resisting frame structures,* Report No. 132. The John A. Blume Earthquake Engineering Center, Stanford University, CA, USA.

Hamburger, R. O., Krawinkler, H., Malley, J. O., & Adan, S. M. (2009). *NEHRP seismic design technical brief no. 2, seismic design of steel special moment frames: A guide for practicing engineers*. National Institute of Standards and Technology.

Ibarra, F. L. & Krawinkler, H. (2005). *Global collapse of frame structures under seismic excitations,* Report No. 152. The John A. Blume Earthquake Engineering Center, Stanford University, CA, USA.

Imanpour, A. (2015). *Seismic response and design of steel multi-tiered concentrically braced frames*. PhD Thesis. Polytechnique Montréal, Canada.

Imanpour, A., Lignos, D., Clifton, C., & Tremblay, R. (2016). Comparison of seismic design requirements for steel moment resisting frames with emphasis on stability of columns in North America, New Zealand, and Europe. *11th Pacific Structural Steel Conference*, Shanghai, China.

Lamarche, C.-P., & Tremblay, R. (2011). Seismically induced cyclic buckling of steel columns including residual-stress and strain-rate effects. *Journal of Constructional Steel Research*, 67(9), 1401-1410.

Lignos, D., Hartloper, A. R., Elkady, A., Deierlein, G. G., & Hamburger, R. (2019). Proposed updates to the ACSE 41 nonlinear modeling parameters for wide-flange steel columns in support of performance-based seismic engineering. *Journal of Structural Engineering*, 145(9), 04019083.

Lignos, D., & Helmut, K. (2011). Deterioration modeling of steel components in support of collapse prediction of steel moment frames under earthquake loading. *Journal of Structural Engineering*, 137(11), 1291-1302.

Lignos, D., & Krawinkler, H. (2012). *Sidesway collapse of deteriorating structural systems under seismic excitations*, Report No. 177. The John A. Blume Earthquake Engineering Center, Stanford University, CA, USA.

MacRae, G. A., A. J. Carr, and W. R. Walpole. (1990). *The seismic response of steel frames*, Report 90-6. University of Canterbury Research, University of Canterbury, Christchurch, New Zealand.

McKenna, F., Fenves, G. L., & Scott, M. H. (2000). Open system for earthquake engineering simulation (OpenSees). University of California, Berkeley, USA.

Nakashima, M., Takanashi, K., & Kato, H. (1990). Test of steel beam-columns subject to sidesway. *Journal of Structural Engineering*, 116(9), 2516-2531.

Newell, J. D., & Uang, C.-M. (2008). Cyclic behavior of steel wide-flange columns subjected to large drift. *Journal of Structural Engineering*, 134(8), 1334-1342.

NRC. (2015). National Building Code of Canada 2015. National Research Council of Canada, Ottawa, ON, Canada.

NRC. (2015). User's Guide – NBC 2015 Structural Commentaries (Part 4 of Division B). Associate Committee on the National Building Code, Ottawa, ON, Canada.

NZS. (1997). *Steel structures standard*, NZS 3404: Part 1:1997. Standards New Zealand, Wellington, New Zealand.

Ozkula, G., Harris, J., & Uang, C.-M. (2017a). Observations from cyclic tests on deep, wide-flange beam-columns. *Engineering Journal*, *American Institute of Steel Construction*, 54, 45-60.

Ozkula, G., Harris, J., & Uang, C.-M. (2017b). Classifying cyclic buckling modes of steel wide-flange columns under cyclic loading. *ASCE Structures Congress*, pp. 155-167.

Ozkula, G., Harris, J., & Uang, C.-M. (2017c). Cyclic backbone curves for steel wide-flange columns: A numerical study. *Ce/Papers*, 1(2-3), 3365-3374.

Ozkula, G., Uang, C.-M., & Harris, J. (2021). Development of enhanced seismic compactness requirements for webs in wide-flange steel columns. *Journal of Structural Engineering*, 147(7), 04021100.

Popov, E. P., Bertero, V. V., Chandramouli, S., & University of California, B. E. E. R. C. (1975). *Hysteretic behavior of steel columns*. Earthquake Engineering Research Center, University of California, CA, USA.

Popov, E. P., Yang, T.-S., & Chang, S.-P. (1998). Design of steel MRF connections before and after 1994 northridge earthquake. *Engineering Structures*, 20(12), 1030-1038.

Ricles, J. M., Zhang, X., Lu, L.-W., & Fisher, J. (2004). *Development of seismic guidelines for deep-column steel moment connections.* ATLSS Report No. 04-13, Lehigh University, Bethlehem, PA, USA.

Shen, J., Associate, S., Astaneh-Asl, A., & McCallen, D. (2002). *Use of deep columns in special steel moment frames*. Steel Tips, Structural Steel Educational Council.

Sousa, A. d. C. e., Suzuki, Y., & Lignos, D. (2020). Consistency in solving the inverse problem of the voce-chaboche constitutive model for plastic straining. *Journal of Engineering Mechanics*, 146(9), 04020097.

Suzuki, Y., & Lignos, D. G. (2015). Large scale collapse experiments of wide-flange steel beam-columns. *8th International Conference on Behavior of Steel Structures in Seismic Areas*, Tongji University, Shanghai, China.

Suzuki, Y., & Lignos, D. G. (2020). Development of collapse-consistent loading protocols for experimental testing of steel columns. *Earthquake Engineering & Structural Dynamics*, 49(2), 114-131.

Suzuki, Y., & Lignos, D. G. (2021). Experimental evaluation of steel columns under seismic hazard-consistent collapse loading protocols. *Journal of Structural Engineering*, 147(4), 04021020.

Tremblay, R., Atkinson, G. M., Bouaanani, N., Daneshvar, P., Leger, P., & Koboevic, S. (2015). Selection and scaling of ground motion time histories for seismic analysis using NBCC 2015. *The 11th Canadian Conference on Earthquake Engineering*, Victoria, BC, CA.

Uang, C.-M., Ozkula, G., & Chansuk, P. (2019). Research on seismic design of deep wide-flange steel columns in the U.S. *12th Pacific Structural Steel Conference*, Tokyo, Japan, Tokyo, Japan.

Yu, Q. S., Gilton, C., Uang, C. M., & Sac, J. V. (2002). *Cyclic response of RBS moment connections: Loading sequence and lateral bracing effects*, Rep. No. SSRP-99/13. Dept. of Structural Engineering, Univ. of California, San Diego, CA.

Zareian, F., & Krawinkler, H. (2009). *Simplified performance based earthquake engineering*, Report No. 169. The John A. Blume Earthquake Engineering Center, Stanford University, CA, USA.

Zareian, F., & Medina, R. (2010). A practical method for proper modeling of structural damping in inelastic plane structural systems. *Computers & Structures*, 88, 45-53.

Zhang, X., & Ricles, J. M. (2006). Experimental evaluation of reduced beam section connections to deep columns. *Journal of Structural Engineering*, 132(3), 346-357.

Appendix A: Supplementary Parameter Study Data

Table A-1. Max drift, corresponding cycle, and out-of-plane displacement, and twist at quarter points at $0.15AF_y$.

Specimen ID	Section	L (mm)	Max Drift		$\Delta_{out\text{-}of\text{-}plane}/L$ (%)			$\gamma_{cross\text{-}section}$ (% rad)		
			Ratio Achieved (%)	Max Cycle Achieved Out of 4	@ 0.25L	@ 0.50L	@ 0.75L	@ 0.25L	@ 0.50L	@ 0.75L
CS1-4.3	W360×237	4300	4.0	4	0.1	0.2	0.2	2.9	2.2	1.1
CS1-6.3	W360×237	6300	4.0	4	0.2	0.3	0.3	5.3	4.1	1.9
CD1-3.3	W530×150	3300	4.0	4	1.0	0.7	0.5	3.7	2.1	0.7
CD1-4.3	W530×150	4300	4.0	4	0.5	0.4	0.3	2.6	1.6	0.9
CD1-5.3	W530×150	5300	4.0	4	0.5	0.5	0.4	9.8	6.8	2.5
CD1-6.3	W530×150	6300	4.0	4	0.9	0.9	0.6	10.5	7.7	3.0
CD2-3.3	W530×182	3300	4.0	4	0.6	0.5	0.3	3.2	1.9	0.7
CD2-4.3	W530×182	4300	4.0	4	0.2	0.3	0.2	2.9	2.2	1.1
CD2-5.3	W530×182	5300	4.0	4	0.5	0.6	0.4	8.4	6.4	2.6
CD2-6.3	W530×182	6300	4.0	4	0.5	0.7	0.8	10.4	8.2	3.3
CD3-3.3	W610×125	3300	4.0	4	3.4	2.4	1.4	4.5	2.7	0.9
CD3-4.3	W610×125	4300	4.0	4	2.1	1.8	1.1	4.8	2.9	1.3
CD3-5.3	W610×125	5300	4.0	1	5.2	5.6	3.3	18.9	15.5	6.1
CD3-6.3	W610×125	6300	3.0	1	3.7	4.2	2.7	12.4	13.3	5.2
CD4-3.3	W610×153	3300	4.0	4	3.4	2.3	1.3	5.4	3.6	4.1
CD4-4.3	W610×153	4300	4.0	4	2.0	1.6	1.0	5.8	3.9	1.5
CD4-5.3	W610×153	5300	4.0	1	6.0	6.5	3.8	15.9	14.9	5.8
CD4-6.3	W610×153	6300	3.0	4	4.8	5.3	3.3	17.2	15.9	6.1
CD5-3.3	W610×174	3300	4.0	4	1.6	1.1	0.7	4.0	2.3	0.8
CD5-4.3	W610×174	4300	4.0	4	0.9	0.7	0.5	3.5	1.9	0.6
CD5-5.3	W610×174	5300	4.0	4	0.4	0.5	0.4	3.5	2.7	1.3
CD5-6.3	W610×174	6300	4.0	4	1.1	0.9	0.6	11.7	8.1	2.9
CD6-3.3	W610×217	3300	4.0	4	1.2	0.8	0.5	4.1	2.4	0.9
CD6-4.3	W610×217	4300	4.0	4	0.6	0.5	0.3	3.6	2.1	2.2
CD6-5.3	W610×217	5300	4.0	4	0.5	0.5	0.4	9.5	6.8	2.7
CD6-6.3	W610×217	6300	4.0	4	1.0	0.9	0.6	11.1	8.1	2.9

Table A-2. Max drift, corresponding cycle, and out-of-plane displacement, and twist at quarter points at $0.25AF_y$.

Specimen ID	Section	L (mm)	Max Drift		$\Delta_{out\text{-}of\text{-}plane}/L$ (%)			$\gamma_{cross\text{-}section}$ (% rad)		
			Ratio Achieved (%)	Max Cycle Achieved Out of 4	@ 0.25L	@ 0.50L	@ 0.75L	@ 0.25L	@ 0.50L	@ 0.75L
CS1-4.3	W360×237	4300	4.0	4	0.2	0.2	0.2	3.5	2.9	1.4
CS1-6.3	W360×237	6300	4.0	4	0.3	0.4	0.3	8.5	6.6	3.1
CD1-3.3	W530×150	3300	4.0	4	3.0	2.0	1.2	3.9	2.3	0.8
CD1-4.3	W530×150	4300	4.0	4	1.8	1.4	0.9	4.1	2.4	0.7
CD1-5.3	W530×150	5300	4.0	4	2.4	2.0	1.3	9.5	6.5	2.6
CD1-6.3	W530×150	6300	4.0	3	2.6	2.8	2.1	9.0	7.0	5.4
CD2-3.3	W530×182	3300	4.0	4	2.2	1.4	0.9	4.1	2.5	1.0
CD2-4.3	W530×182	4300	4.0	4	1.1	0.8	0.5	5.1	3.2	1.3
CD2-5.3	W530×182	5300	4.0	4	1.9	1.6	1.0	10.4	7.7	3.0
CD2-6.3	W530×182	6300	4.0	4	1.9	1.8	1.2	11.4	8.8	3.5
CD3-3.3	W610×125	3300	3.0	3	3.7	2.8	1.6	3.5	2.0	0.7
CD3-4.3	W610×125	4300	3.0	3	2.9	2.8	1.8	4.6	3.2	2.5
CD3-5.3	W610×125	5300	2.0	2	2.6	3.2	2.1	15.3	13.2	4.4
CD3-6.3	W610×125	6300	2.0	1	2.3	3.1	2.1	9.7	10.7	3.9
CD4-3.3	W610×153	3300	4.0	2	5.3	4.3	2.6	4.6	3.0	1.2
CD4-4.3	W610×153	4300	3.0	4	2.9	2.8	2.0	4.7	3.3	2.9
CD4-5.3	W610×153	5300	2.0	3	3.3	3.9	2.5	12.8	12.3	4.6
CD4-6.3	W610×153	6300	2.0	1	2.3	3.1	2.0	8.5	8.4	3.3
CD5-3.3	W610×174	3300	4.0	2	3.3	2.4	1.3	3.4	1.8	0.8
CD5-4.3	W610×174	4300	4.0	3	2.6	2.1	1.3	3.6	1.9	1.2
CD5-5.3	W610×174	5300	4.0	4	0.8	0.7	0.5	31.4	19.0	4.1
CD5-6.3	W610×174	6300	4.0	2	2.5	2.5	2.0	8.2	6.9	4.2
CD6-3.3	W610×217	3300	4.0	4	3.3	2.2	1.2	4.3	2.6	0.9
CD6-4.3	W610×217	4300	4.0	4	2.1	1.5	0.9	4.5	2.7	1.0
CD6-5.3	W610×217	5300	4.0	4	1.0	0.8	0.6	29.2	17.5	6.6
CD6-6.3	W610×217	6300	4.0	4	2.6	2.4	1.7	10.7	7.9	3.3

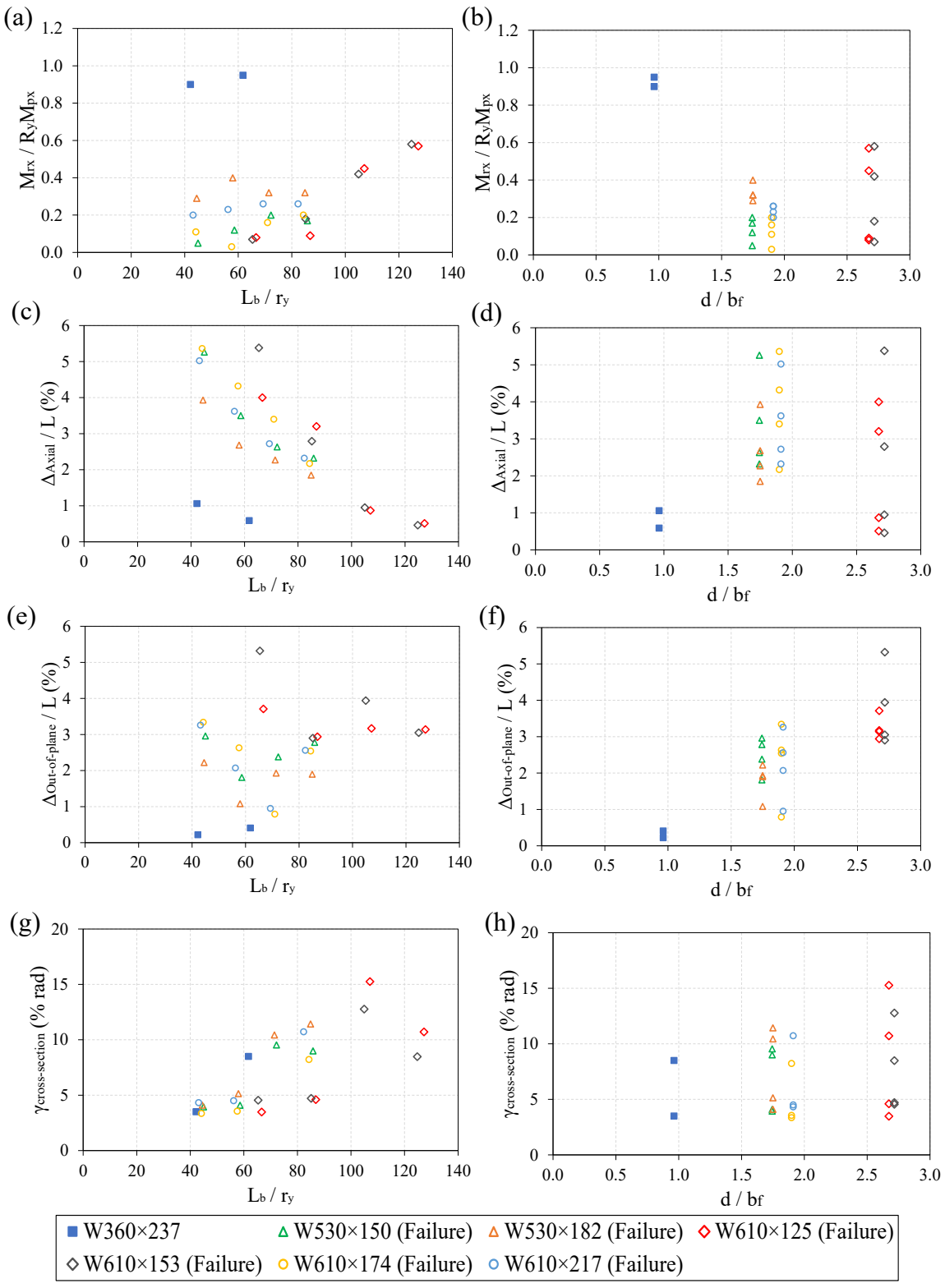

Figure A-1. Column strength and deformation response parameters under an axial load of $0.25AF_y$: (a-b) Flexural strength at the base vs. L_b/r_y and d/b_f; (c-d) Axial shortening vs. L_b/r_y and d/b_f; (e-f) Out-of-plane displacement at the base vs. L_b/r_y and d/b_f; (g-h) Cross-section twist angle vs. L_b/r_y and d/b_f (data points with a hollow marker indicate failure).